LSU Doctoral Dissertations   Graduate School

2009

Fabrication of nanostructured surfaces with well-defined chemistry using particle lithography

Jie-Ren Li
Louisiana State University and Agricultural and Mechanical College, jli11@tigers.lsu.edu

FABRICATION OF NANOSTRUCTURED SURFACES WITH WELL-DEFINED
CHEMISTRY USING PARTICLE LITHOGRAPHY

A Dissertation

Submitted to the Graduate Faculty of the
Louisiana State University and
Agricultural and Mechanical College
in partial fulfillment of the
requirements for the degree of
Doctor of Philosophy

in

The Department of Chemistry

by
Jie-Ren Li
B.S., National Chung Cheng University, 1998
M.S., National Chiao Tung University, 2000

May 2009

ACKNOWLEDGEMENTS

This research results from years of study and reflection as a Ph.D. student. During this period, the thoughts and ideas have matured gradually and have taken shape to become my research topic. For these investigations, I have had assistance from many people whose recommendations and guidance helped to deepen my understanding about the subjects of this dissertation. I owe my gratitude to these individuals for many of the best ideas and inspiration behind this work and express my whole-hearted gratitude to each of them for their valuable contributions.

First of all, I want to express appreciation to my advisor, Dr. Jayne C. Garno, who inspired my interest in the subjects of surface science and scanning probe microscopy. Constant support and guidance contributed to every accomplishment presented here. Great mentorship helped to mold me into the scientist I am today. I am grateful to my committee members, Dr. Evgueni E. Nesterov, Dr. Kermit K. Murray, Dr. Julia Y. Chan, Dr. Bin Chen and Dr. James M. Matthews, who reviewed my dissertation and provided valuable feedback. I also acknowledge Pfizer and Center for BioModular Multi-Scale Systems for fellowship.

I am indebted to my family and to my friends for their moral support and the gentle nudges that they provided in every way possible. My parents and sister gave me confidence and encouragement while I completed this research. My close friend, Szu-Fang Chuang, has been there for me every step of the way, patiently listening to me and providing important suggestions.

I would like to thank my colleagues in the Garno research group, especially for Brian Lewandowski, Belle LeJeune and Kathie Lusker. I sincerely cherish all the moments we shared together as colleagues and friends.

TABLE OF CONTENTS

LIST OF FIGURES

ABSTRACT

Natural self-assembly processes provide nanofabrication capabilities for designing surfaces with nanoscale control of surface chemistry and relative orientation of the nanomaterials on the surfaces. Particle lithography was used to produce periodic arrays of protein nanostructures. Monodisperse mesoparticles can be applied to rapidly prepare millions of uniform protein nanostructures on flat surfaces using the conventional benchtop chemistry steps of mixing, centrifuging, evaporation and drying. Nanopatterns of bovine serum albumin and staphylococcal protein A were produced with particle lithography. The immobilized proteins remain attached to the surface and form nanopatterns over micron areas corresponding to the thickness of a single layer of proteins. The morphology and diameter of the protein nanostructures are tunable by selecting the ratios of protein-to-particle and the diameters of spheres.

Organosilane nanopatterns were fabricated using particle lithography combined with vapor deposition to regulate surface chemistry. Colloidal masks produced by particle lithography enable to control and direct the placement of nanoscopic residues of water for hydrosilation. Different geometries of silane nanostructures depend on the length of drying for particle masks. Organosilanes form covalent bonds with the surface through hydrolysis, which provide an excellent platform for further steps of chemical modification. The head groups of organosilane nanopatterns can be designed to generate spatial selectivity for electroless deposition of iron oxide and selective adsorption of gold nanoparticles.

New imaging strategies using atomic force microscopy (AFM) were developed for mapping magnetic domains and elastic compliance at size regimes below 100 nm. The AFM-based imaging mode is referred to as magnetic sample modulation (MSM). The AFM tip serves as a force and motion sensor for mapping the vibrational response of magnetic nanomaterials. The

information acquired from MSM images includes the distribution of individual magnetic domains as well as spectra of the characteristic resonance frequencies of the vibrating nanomaterials. Indirect magnetic modulation (IMM) based on indirect oscillation of soft nonmagnetic cantilevers was used to investigate elastic response of organosilane nanostructures. With the use of IMM, dynamic parameters of the driving frequencies and amplitude of the tip motion can be optimized to sensitively map the elastic response of samples.

CHAPTER 1. INTRODUCTION

Engineering surface chemistry at the nanoscale poses a fundamental challenge for applications in the emerging fields of nanoscience and nanotechnology.[1-3] Regulating the composition and distribution of functional chemical groups on surfaces is an important strategy for directing the adsorption of nanomaterials with spatial selectivity.[4-7] A number of lithography methods have been advanced towards development of well-defined nanoscale architectures. For developing methods of lithography at the nanoscale, the critical issues to be considered are reproducibility, resolution, reliability, fabrication speed and throughput. Fabrication of nanosized structures on surfaces provides new possibilities for investigating the size-dependent properties of nanomaterials and thin films.[6, 8-10] Various imaging modes of atomic force microscopy (AFM) can be applied for characterizing designed nanoscale test structures, to enable systematic investigations of the changes in properties as a function of geometry and dimensions.[11-14] The investigations described in this dissertation applied a strategy of combining nanoscale lithography with AFM characterizations, to generate well-defined test platforms for molecular-level measurements.

1.1 Background – Development of Methods for Nanoscale Lithography

Various lithographies have been developed to generate well-defined structures of organic thin films, metals, proteins and nanomaterials, for a broad range of dimensions, as summarized in Figure 1.1. Conventional approaches such as micromachining and photolithography are not amenable for fabrication at the sub-100 nm size scale.[15] Soft lithography methods such micro-contact printing have been widely applied as promising high-throughput patterning techniques due to the capabilities for achieving nanometer sizes.[16] However, fabricating ultrasmall molds and masks with regular nanoscale dimensions is difficult and requires expensive laser or e-beam

1

instruments. Scanning probe lithography (SPL) enables production of regular nanostructures of organic thin films; however the slow serial fabrication processes are time-consuming. It is unlikely that SPL will achieve the high throughput needed to prepare millions of nanostructures for device manufacture.[17-21]
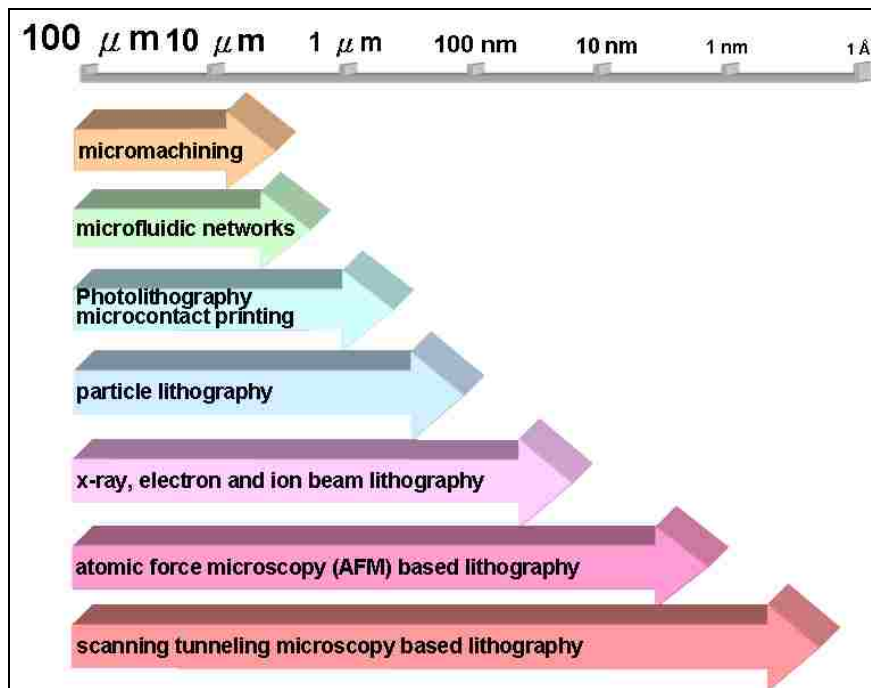
Figure 1.1 Dimensions achievable by micro- and nanofabrication approaches.

1.2 Particle Lithography

Particle lithography provides a number of advantages compared to other established lithographies, such as uniform geometry, high throughput, and reproducibility. Particle lithography uses the close-packed arrangement of spherical particles to produce ordered arrays of regular nanostructures.[22, 23] Monodisperse spheres self-assemble on flat surfaces into periodic structures with designed dimensions and interparticle spacing which can then be used as structural templates or evaporative masks to guide the deposition of various materials.[24-30]

To regulate the position of nanomaterials on surfaces, particle lithography provides a way to fabricate nanostructures with well-defined functionality and geometry. Chapter two describes the

capabilities of particle lithography for generating regular protein nanostructures.[31, 32] The arrangements and surface coverage of proteins on surfaces is determined by the close-packed structural templates of monodisperse latex mesospheres. Conventional steps of bench chemistry for mixing, centrifuging, drying and rinsing during particle lithography provide exquisite control for the surface coverage and periodicity of protein nanopatterns. The periodicity of the protein nanostructures is tunable by selecting the sizes of mesospheres. The morphologies of nanopatterns can be tailored by changing the protein-to-particle ratios, providing arrays of exquisitely uniform and regular protein nanostructures.

1.3 Nanopatterns of Organosilane Self-Assembled Monolayers

A requirement for defining surface chemistry at the nanoscale is the ability to create geometrically well-defined architectures with the desired chemical functionalities. Self-assembled monolayers (SAMs) of organosilanes provide a means to design surface chemistries to resist or adsorb nanomaterials in further reaction steps.[33-35] Particle lithography was combined with vapor deposition to generate organosilane nanopatterns on various substrates.[36-38] For organosilanes to bind to surfaces, nanoscopic amounts of water are needed to initiate silane hydrolysis. Evaporative masks of latex or colloidal silica mesoparticles prepared by particle lithography were used to direct the placement of nanoscopic residues of water. Drying intervals of the masks were used to regulate the nanoscopic amounts of water present on surfaces. Chapter three reports the differences in the morphologies of organosilane nanopatterns observed for different drying conditions.[36] The surface coverage and pattern geometry, as well as surface functionalities were evaluated using AFM characterizations.

Typical substrates used for preparing SAMs of organosilanes are silicon, quartz, glass, metal oxides and mica. Most typically, free hydroxyl groups on surfaces are required to form

3

SAMs of organosilanes. Chapter four demonstrates that organosilane nanostructures can be generated on gold, which is a substrate devoid of hydroxyl groups.[37] Pre-treatment of gold films with UV-irradiation renders the surface to be sufficiently hydrophilic for particle lithography. Close-packed films of monodisperse latex mesoparticles provide an evaporative mask to spatially direct the placement of nanoscopic amounts of water on surfaces. Vapor phase organosilanes deposit selectively at areas of the surface containing water residues, forming nanopatterns with regular thickness, geometry and periodicity.

1.4 Further Reaction Steps with Organosilane Nanostructures

Surfaces with well-defined nanopatterns provide a platform to spatially define locations for further chemical steps, such as reactions with proteins, metals, nanoparticles and organic molecules. The chemistry presented at the surface of nanopatterns can be designed by choosing from a broad and diverse range of organosilane functionalities. Organosilane nanopatterns prepared by particle lithography provide a foundation to direct and confine the adsorption of new molecules and nanomaterials with designed geometry and periodicity.[38] Engineered nanopatterns of adhesive and resistive silane SAMs offer exquisite surface selectivity which can be further used as a platform for site-selective adsorption of metals.[39, 40] Arrays of iron oxide nanostructures fabricated using electroless deposition onto nanopatterned surfaces will be described in chapter five.[39] The head groups of organosilanes enable exquisite selectivity for the deposition of iron oxide. The well-defined geometries of organosilane nanopatterns define sites for electroless deposition of iron oxide. The periodicity of the iron oxide nanostructures is determined by the diameter of mesospheres used for particle lithography. Arrays of iron oxide nanostructures conform precisely to the selected areas of patterned organosilanes with reproducible and near-

perfect nanoscale geometries, which can then be used as a test platform for investigating nanomagnetism.[40]

1.5 Characterization of Metal Nanostructures Using Magnetic Sample Modulation AFM

Studies of the size-scaling effects of nanomaterial properties are an important direction for surface investigations. However, the difficulties for characterizing properties at very small dimensions must be overcome.[5, 8, 41, 42] A key strategy for investigating properties of nanomaterials is to produce arrays of regular nanostructures as test platforms with tailorable sizes and spacing.[9, 43, 44] The combination of nanofabrication and AFM enables investigations of structure/property relationships and measurements of size-dependent properties. Chapters six and seven demonstrate that periodic arrays of nanostructures can be used to evaluate new strategies for nanoscale measurements and imaging with AFM. A new imaging mode of magnetic sample modulation (MSM) was developed to map magnetic nanomaterials with dimensions less than 100 nm.[40] Arrays of iron oxide nanostructures produced using particle lithography and electroless deposition were used to develop and evaluate the capabilities of MSM. When an oscillating electromagnetic field is applied to arrays of iron oxide nanostructures, the magnetic nanostructures are selectively driven to vibrate. A non-magnetic AFM tip serves as a force and motion sensor for mapping the vibrational response of iron oxide nanostructures. Changes in the phase and amplitude images with and without an applied magnetic field are used to selectively detect magnetic domains of iron oxide. The information acquired from MSM images includes the distribution of individual magnetic domains as well as spectra of the characteristic resonance frequencies of the vibrating nanomaterials. Chapter six describes the operating principle of the MSM imaging mode and the capabilities of MSM for characterizing magnetic nanomaterials.

1.6 Characterizations of Nanostructures Using Indirect Magnetic Modulation AFM

Nanoscale investigations of the mechanical properties of thin films and surface structures, e.g. viscoadhesion and elasticity, are important for development of new engineered materials. New capabilities for evaluating the elastic compliance and viscoelastic behavior of organic thin films can be accomplished using various dynamic AFM imaging modes. We have developed a new set-up for force modulation AFM imaging mode based on an instrument configuration with indirect magnetic modulation (IMM).[45] Chapter seven demonstrates successful characterizations of the elastic response of organosilane nanostructures using IMM. For IMM, an AFM tip is driven to vibrate indirectly by the motion of a tip holder assembly which contains ferromagnetic materials. The entire tip assembly is induced to vibrate by the flux of an external AC electromagnetic field. With IMM, dynamic parameters of the driving frequencies and amplitude of the tip motion can be optimized to sensitively map the elastic response of organosilane nanostructures.

1.7 Dissertation Synopsis

New approaches for particle lithography have been advanced to generate well-defined surfaces with desired functionalities and geometries. The position and spatial distribution of nanomaterials can be controlled at the nanoscale with mesoparticle masks/templates prepared by particle lithography. The spatial selectivity provided by particle lithography was used for further chemical reactions to deposit proteins, metals and nanoparticles. New AFM imaging modes were developed, which provide insight into size-dependent properties and provide new tools for nanoscale investigations of surface properties.

CHAPTER 2. FABRICATION OF NANOPATTERNED FILMS OF BOVINE SERUM ALBUMIN AND STAPHYLOCOCCAL PROTEIN A USING LATEX PARTICLE LITHOGRAPHY

2.1 Introduction

Particle lithography is an approach for patterning surfaces which exploits the natural assembly of spherical particles into organized 2-D or 3-D crystals. Monodisperse latex particles self-assemble into periodic structures on flat surfaces, which can then be used as structural templates or photomasks.[46, 47] Particle lithography is a versatile approach for producing nanoscale features spanning large areas, and has been used to pattern metals,[41, 48-54] catalysts,[55] self-assembled monolayers (SAMs),[56, 57] polymers[27, 58-60] and inorganic materials.[24-26, 61-63] The latex particles typically are removed by calcination or solvent dissolution. Potential applications include biosensing,[64, 65] photonic crystals[23, 66-69] and optical gratings.[70] Researchers have applied lithography with latex beads as photomasks, to construct functional surfaces for selective protein adsorption on well-defined regions.[71, 72] Particle lithography also can be applied for organizing proteins on surfaces to generate periodic arrays of protein nanostructures, with superb control of the distribution of proteins within a single layer over micron-sized areas.[30]

Tools for nano- and microfabrication will provide important contributions in developing biochip and biosensing technologies, as well as supply basic research in protein–protein interactions. Nanoscale studies can be applied to refine critical parameters used to link and organize proteins on surfaces of biochips and biosensors. Miniaturization provides rewards of reduced quantities of analytes and reagents, increased density of sensor and chip elements, and more rapid reaction response.[73-76] Protein microarrays based on AFM detection may soon reach

capabilities for routinely achieving single molecule detection. Ultra small protein patterns can be used in biosensing, control of cell adhesion and growth, and in biochip fabrication.[77-79] Technologies for protein arrays including protein-based biochip and biosensing devices are predicted to bring advancements to biotechnology, clinical diagnostics, tissue engineering, and targeted drug delivery.[80-82] With the rapid progress in development of large sets of characterized antibodies, protein and antibody arrays will provide tremendous advantages for diagnostics and medical science. Methods of high-throughput protein analysis offer immense potential for fast, direct and quantitative detection, including the possibility of screening thousands of proteins within a single sample to test for protein, ligand, and drug interactions.[81, 82] Biomolecules immobilized on a surface serve as the receptor and in some cases as the signal transducer in biosensors. Therefore, the placement of biological ligands in precisely defined locations can increase the density of sensor elements and lead to improved detection limits with molecular level control of the surface reactivity.[74, 83] As a proof-of-concept, Wolinsky, Mirkin and coworkers have reported a nanometer-scale antibody array prepared by DPN to test for the presence of the human immunodeficiency virus type 1 (HIV-1) in blood samples.[84] Antibodies for HIV-1 were immobilized on carboxylate-terminated nanopatterns for hybridizing (HIV-1 p24) antigen and bound proteins. With a nanoarray of 100 nm features written by DPN, the three-component sandwich assay exceeded the limit of detection of conventional enzyme-linked immunosorbent assay (ELISA) immunoassays by 1000-fold. Improved binding to surfaces onto which capture proteins are arrayed and improved sensitivity of detection are technical challenges for further advancing protein microarray technology.

At the core of biosensing is detection of biomolecular binding events with high selectivity and sensitivity. Typically, bioassays for surface-bound proteins are not as sensitive as approaches

which use solution chemistry, due in part to the accessibility of molecules for binding. Pressing the limits of protein patterning to the nanometer scale will furnish direct views of the differences in immobilization chemistries, which will aid development of more sensitive assays. Conventionally, biosensors and biochips are produced using microspotting or solution deposition to place proteins on various surfaces, without control of the placement and arrangement of target proteins within protein deposits. There is a requirement for efficient yet mild immobilization chemistries which preserve tertiary structure and maximize the activity of fragile biomolecules. Thus, to generate nanopatterns of proteins it is desirable to use mild aqueous conditions, with simple steps to rapidly generate viable surfaces. Simple physical adsorption is the most widely used method to generate protein spots for biochip surfaces. Particle lithography is a highly reproducible approach for patterning proteins using mild conditions and offers advantages of high throughput and reproducibility to generate a single layer of protein nanostructures over wide areas. The size, shape and spacing of features can be systematically varied by changing the diameter of the latex particles. Using latex particles to control the arrangement of proteins on surfaces is a practical technology which is amenable to microspotting or immersion methods used for protein microarrays and biochips. Latex bead immobilization has been applied in spotting solutions to create microarrays for detection of antibodies.[85] Particle lithography offers the advantages of nanometer precision and high throughput, since a small vial of solution can produce hundreds of replicate samples. In this investigation, latex particle lithography is applied for nanopatterning proteins and mixtures of BSA and protein A. Atomic force microscopy (AFM) images display the morphology of patterned proteins. Nanostructured protein layers formed using particle lithography may be suitable for application in surface-bound immunoassays with advantages for quantitative evaluation with well-defined surface arrangements of proteins.

9

2.2 Experimental Approach

2.2.1 Materials and Reagents

Staphylococcal protein A (SpA) from Staphylococcus aureus and bovine serum albumin (BSA), were purchased from Sigma Biochemicals (St. Louis, MO, USA). Solutions of 2.0 mg mL^{-1} BSA and 0.1 mg mL^{-1} SpA were prepared with deionized water (Milli-Q, 18 megaohm). Pieces of freshly cleaved Ruby muscovite mica were used as substrates (S&J Trading Co., NY). Mica can be easily cleaved to produce clean, atomically flat surfaces for protein deposition.

Monodisperse polystyrene latex solutions were purchased from Duke Scientific (Palo Alto, CA). To remove contaminants such as charge stabilizers or surfactants the latex nanospheres were washed once with deionized water by using centrifugation. A pellet is formed after centrifuging latex suspensions for 10–20 min at 12000 rpm. The pellets can then be resuspended in aqueous solutions by vortex mixing. The ratios of protein and latex were controlled by adding the appropriate volumes of protein solutions to washed latex pellets.

2.2.2 Atomic Force Microscopy

AFM images were acquired in contact mode with a deflection type scanner (PicoSPM) from Molecular Imaging (Tempe, AZ). The electronic controllers and software were purchased from RHK Technology (Troy, MI). Standard soft silicon nitride cantilevers with force constants ranging from 0.06 to 0.16 N m^{-1} were used for imaging.

2.2.3 Particle Lithography

An overview of the steps for particle lithography with proteins is displayed in Figure 2.1. First, the protein and latex are mixed together in an aqueous solution. Monodisperse latex particles are mixed with aqueous solutions of the desired protein (BSA, IgG or SpA) at a certain ratio. For best results, the solution containing protein and latex should remain at room

temperature for time intervals no longer than 4 h. (To maintain protein activity the solutions should be freshly prepared, and to minimize contaminants, the latex particles should be washed to ensure that the particles are free of surfactants.) In the second step, a small volume (10 mL cm^{-2}) of the latex and protein solution is deposited at the center of the substrate, using a pipette. The liquid spreads out into a thin layer across the surface as it dries. Next, the deposit is dried at room temperature. As the water evaporates during drying, a film of protein and latex is formed in which the latex nanoparticles assemble together into close-packed crystalline assemblies. After the deposits have dried, the latex is rinsed away with deionized water to leave a layer of protein nanostructures on the surface. A monolayer of protein remains securely attached to the surface with an imprinted pattern of nanostructures.
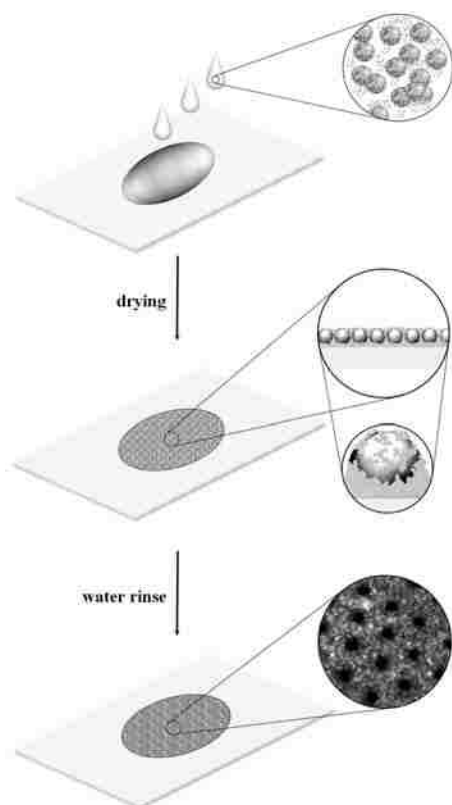
Figure 2.1 Particle lithography procedures. A drop of solution containing latex and proteins is deposited on the surface and allowed to dry. During drying the spheres form organized crystalline layers surrounded by protein. Latex particles are removed by rinsing with deionized water to form arrays of protein nanostructures.

2.3 Results and Discussion

The hexagonal, close-packed arrangement formed by the natural self-assembly of monodisperse spheres is a well-studied phenomenon, which has been exploited for many lithographic procedures.[23, 86-88] For protein lithography, the organized crystalline arrangement of latex nanospheres provides a structural template for forming protein nanopatterns. Since the various steps of latex particle lithography can be characterized using AFM or electron microscopy, views of latex layers are presented in Figure 2.2 for 500 nm particles. The particles for the SEM micrograph (Figure 2.2A) were sputtercoated with 5 nm carbon, and thus do not provide sufficient resolution for viewing the protein coatings. The top-view of latex spheres (Figure 2.2B) shown by the AFM topography image indicates a rougher surface morphology for the protein-coated spheres. The images clearly exhibit a 2-D close-packed organization with long-range order, with few defects or missing particles. Depending on the number of latex particles deposited the films were shown to form single or multilayers, with typical arrangements as in Figure 2.
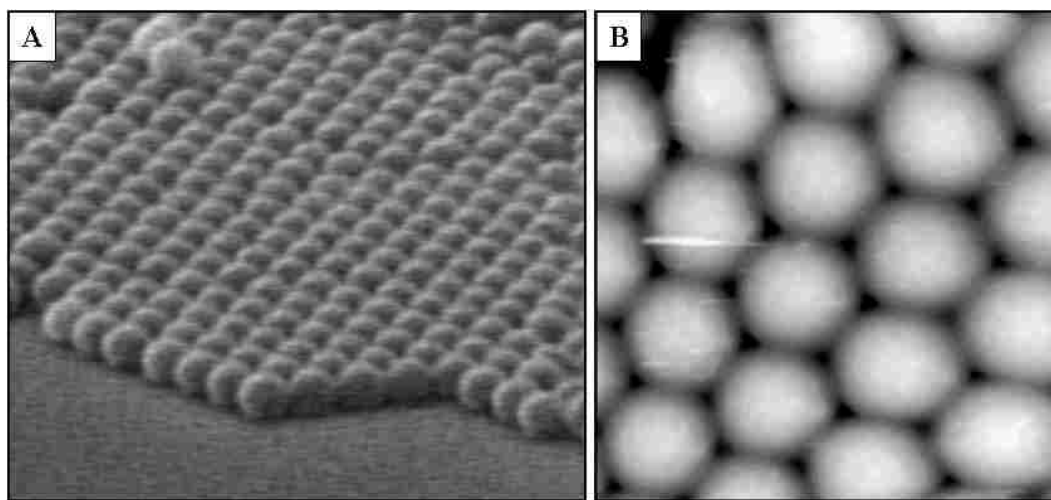
Figure 2.2 Views of the arrangement of 500 nm latex particles using (A) scanning electron microscopy and (B) atomic force microscopy.

As shown in Figure 2.3, particle lithography using monodisperse latex nanoparticles can produce highly organized, periodic arrays of protein nanostructures. The image reveals a film of BSA with circular areas of uncovered substrate where the latex particles were displaced. This morphology spans wide areas on the mica substrate. The image presented is representative of images from several areas of the samples which were examined by translating the sample stage and imaging at different locations. The arrays of protein nanostructures maintain the order and periodicity of the latex films. The exquisite capability for producing periodic nanostructures over broad areas is viewed for an 11×11 μm^2 area in Figure 2.3. The periodicity most likely extends to even larger regions of the surface, spanning microns, as suggested by SEM images of the latex layers in Figure 2.3. The long-range order and periodicity of the structural templates are maintained after removal of the latex by rinsing.

11 x 11 μm²
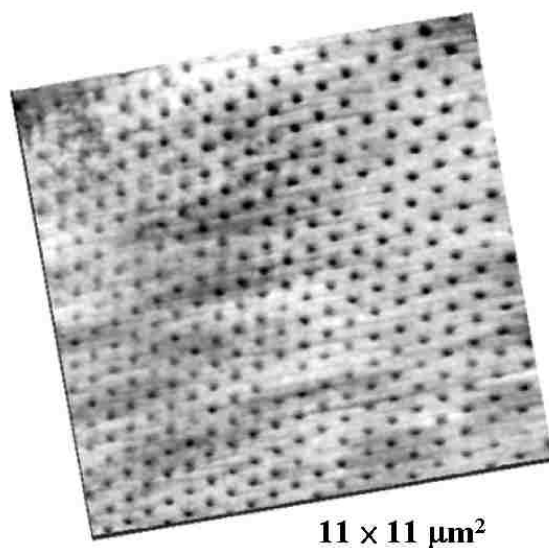
Figure 2.3 Three-dimensional AFM image of nanostructures of BSA on mica(0001).

Example images of arrays of BSA are shown in Figure 2.4 at various protein : latex ratios. The 2-D AFM topographs reveal an organized arrangement of circular dark holes, (uncovered areas of mica) surrounded by clusters of BSA. The periodicity of the resulting nanopatterns

13

depends on the separation of latex spheres, which is observed to be 5–15% smaller than the original latex diameters. This is likely attributable to the shrinking and deformation of latex particles during drying. Using 500 nm particles, the ratio of BSA : latex was 61000 : 1 which corresponds approximately to a single layer of proteins encapsulating a sphere. The appropriate ratios found to be successful for particle lithography have ranged from half of monolayer coverage for surrounding spheres to that of two layers, manifesting different morphologies. As viewed in the topographs of Figure 2.4A and 2.4B, (1.5 × 1.5 μm^2) the periodicity and morphology of surface structures are quite different when changing protein : latex ratios. For Figure 2.4B, the ratio corresponds to an incomplete shell of protein surrounding a latex sphere, approximately half of a shell. A more dense arrangement of proteins surrounding the base of the latex spheres is observed, and the areas show incomplete coverage of protein between the ring-shaped nanostructures. In contrast, at higher ratios, the cursor profile for Figure 2.4A indicates that the thickness of the protein layer is relatively uniform across the surface, completely filling in the areas between the cavities where latex particles were displaced.

The height of the protein layer can be referenced using the uncovered areas of mica as a baseline. The cursor measurements of Figure 2.4 indicate a thickness of 3.7 ± 0.2 nm, which corresponds well with the dimensions of a single layer of protein. The diameter of BSA is 4.0 nm according to X-ray crystallography measurements.[89] The periodicity of BSA nanostructures was affected by drying intervals and protein : latex ratios. To measure the periodicity, the distances between nanopatterns were averaged for at least 200 nanostructures, using several AFM topographs from various areas of the surface. For the 500 nm latex particles of Figure 2.4, the 61000 : 1 ratio resulted in an average periodicity of 422 ± 66 nm, approximately 15 % less than the expected distance between latex particles. When using the 30500 : 1 ratio, the periodicity

measured 460 ± 78 nm, which is approximately 8 % smaller than the expected 500 nm interparticle spacing. A possible explanation of these observed systematic differences may result from facilitating a more ordered, tighter packing through changes in solution conditions.
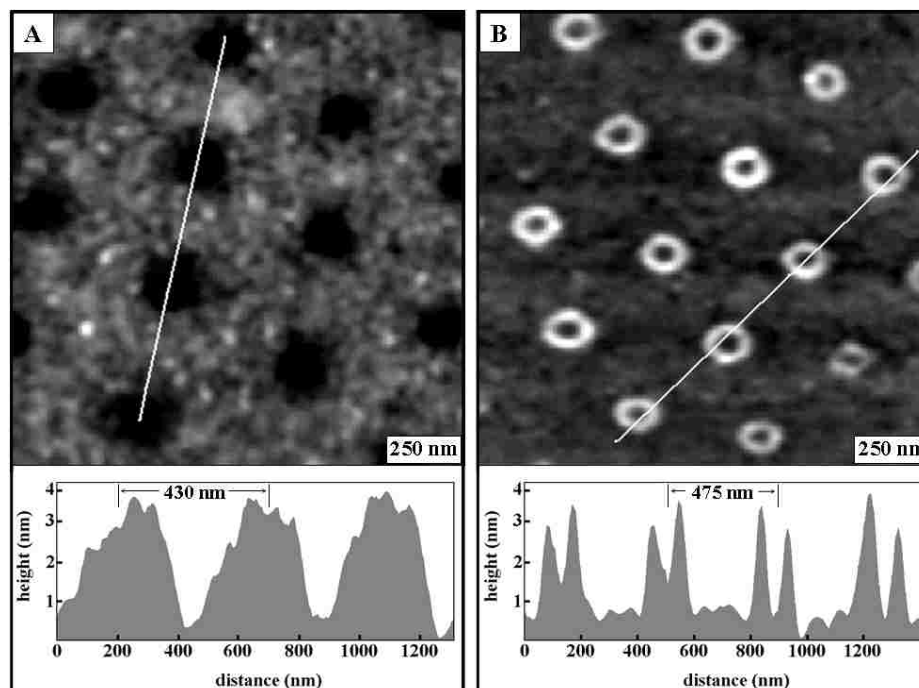
Figure 2.4 Arrays of BSA nanostructures produced with 500 nm latex particles at different ratios. (A) AFM topograph and corresponding cursor profile using a protein : latex ratio of 61000 : 1. (B) A different morphology is observed using a ratio of 30500 : 1.

Particle lithography uses mild conditions (ambient temperatures, aqueous buffers), yet provides nanometer-level control of the spatial distribution of proteins organized within a single surface layer. Even for latex particles as small as 200 nm, particle lithography was applied successfully to prepare arrays of BSA nanostructures (Figure 2.5). The periodicity and size of uncovered areas is tunable by selecting the latex diameter and protein : latex ratios. For 200 nm spheres, a full monolayer would result from a 9000 : 1 ratio of BSA : latex. To generate the nanostructures viewed in Figure 2.5, a ratio of 4000 : 1 was used to form patterns, which corresponds roughly to half of a monolayer shell of proteins encapsulating a 200 nm latex sphere.

15

Note that the image reveals regular triangular and hexagonally shaped arrangements of protein. The compression of deformable latex spheres results in a tightly packed, honeycomb morphology. The thickness of the protein films measured 3.8 ± 0.2 nm and the average periodicity measured 179 ± 44 nm for these conditions.
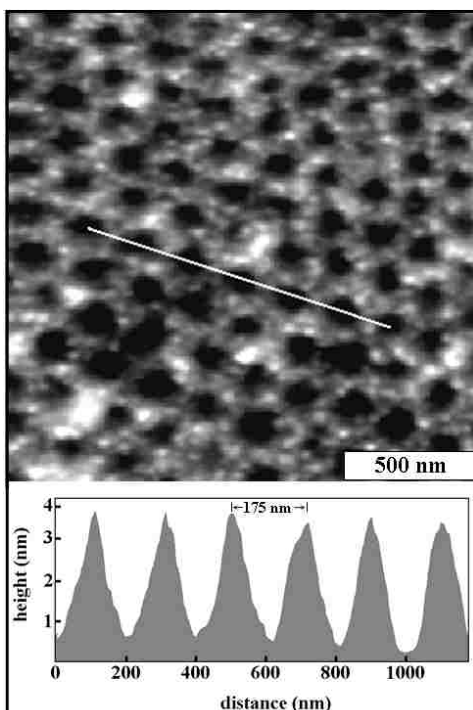
Figure 2.5 Periodic arrays of BSA nanostructures produced by nanoparticle lithography using 200 nm latex particles.

A general observation that can be made is that the surface morphologies were highly consistent and reproducible for a given ratio and particle diameter. Once the experimental conditions have been chosen, dozens of samples prepared with those chosen conditions exhibited similar morphologies. The periodicity was found to vary depending on the rate of drying and when using different latex stock solutions from the manufacturer. Particle lithography was also successfully applied for nanopatterning rabbit IgG.[30] Both IgG and BSA nanopatterns retained the ability to bind corresponding specific antibodies.

Another important observation was that latex particles were completely removed from the surfaces by simple water rinsing. Several factors most likely contribute to the ease of latex removal. First, the hydrodynamic radius of latex particles changes upon wetting. The swelling of latex particles has been previously observed[90, 91] and can cause the diameter of spheres to increase as much as 15 %. This increase in particle size serves to rapidly break latex assemblies apart and enable the spheres to dislodge from the surface when hydrated. The chemical nature of the surface of latex is different when wet, providing weaker adhesion between proteins and the surface of the spheres. Another factor is the contact area between a sphere and a plane is relatively small. Even with deformation during drying, the area of a sphere anchored to the flat surface does not provide enough anchoring bonds to sustain water rinsing. The length of drying was found to affect latex removal; samples which have been dried for many days required lengthy soaking (~30 min) for the latex to be completely removed.

Although the steps of the procedure for particle lithography are simple and direct, the mechanism for creating protein nanostructures is complex and involves many factors. Variables such as the surface charge of the substrates, proteins and latex spheres certainly contribute to the regular periodic spacing and distribution of proteins and spheres formed on surfaces. The nature of the binding interactions (weak or strong between protein and latex, between protein and the substrate, between latex and the substrate) affect the feasibility of particle lithography. For example, the binding between latex and mica is sufficiently weak to enable complete removal of spheres with rinsing, and the binding of BSA or IgG to mica was strong enough to sustain steps of rinsing and immersion in buffers. Surfaces such as aldehyde terminated self-assembled monolayers or glass were found to strongly bind latex spheres and were unsuitable for protein lithography. Surfaces such as methyl, hydroxyl or carboxyl terminated self-assembled

monolayers were unsuitable since both the proteins and latex particles were easily rinsed away. Thus far, particle lithography has been successful using either clean Au(111) or mica(0001) surfaces.

It has also been observed from cursor measurements for the systems studied thus far that only a single layer of protein remains after rinsing. Although it is likely that protein multilayers may be deposited at higher ratios, the protein–protein interactions which form in protein multilayers have not been able to persist after rinsing with water or buffers, as evidenced by AFM images. By far, the most widely used method of protein immobilization for protein arrays uses nonspecific adsorption of proteins dried on solid supports. Forces which nonspecifically influence the binding of proteins to almost any substrate include ion bridging, hydration forces, hydrophobic forces, and short range attractive or repulsive forces.

Surface assays typically include a blocking step, such as with the adsorption of bovine serum albumin (BSA) to prevent nonspecific binding of proteins. BSA is a globular serum protein which is often used in bioassays to backfill uncovered areas of surfaces where proteins did not attach. A logical step towards developing a generic approach for protein arrays is to deposit mixtures of BSA with the proteins for assays. The protein chosen is staphylococcal protein A (SpA) which contains five homologous IgG-binding domains that interact with the Fc portion of immunoglobulins from various mammals at neutral pH.[92, 93] The bound antibodies can be eluted from protein A at acid pH to regenerate immunoaffinity surfaces. Many immunological methods have been developed and refined using SpA as a reagent, including immunoprecipitation techniques and sandwich immunoassays. SpA has a molecular weight of 42000 and exhibits an extended shape with an estimated Stokes radius of 4.0 nm.[94] Figure 2.6 displays an AFM topograph (0.5 × 0.5 μm^2) of nanopatterns of a mixture of BSA and SpA

18

produced with 200 nm latex particles and a protein-to-latex ratio of (3900 BSA + 1400 SpA) : (1 latex). The cursor profile indicates the periodicity of the nanostructures is 167 ± 18 nm, and the height of the protein layer measured 6.6 ± 0.8 nm. This thickness corresponds approximately to the sum of the dimensions of BSA and SpA, suggesting that a mixed multilayer of protein has formed. Future investigations will explore the effect of various BSA : SpA ratios on the nanopattern morphology, and will evaluate changes after binding IgG to SpA.
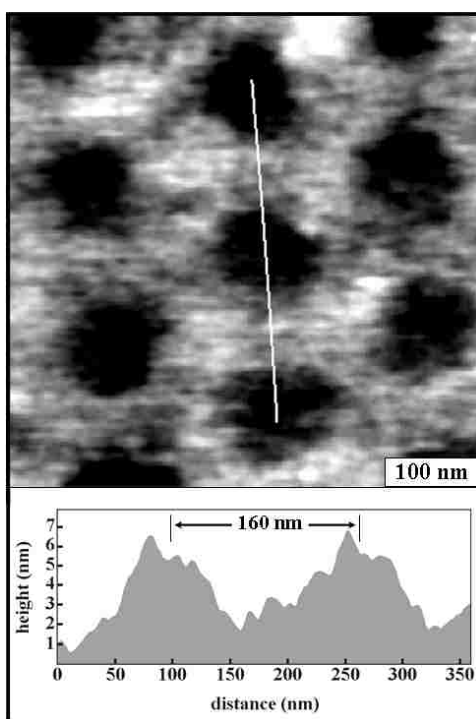
Figure 2.6 Nanostructures of a mixture of BSA and protein A produced by nanoparticle lithography with 200 nm latex particles.

2.4 Conclusion

Particle lithography, which has been widely applied for metal, polymer and inorganic materials, can also be used to generate protein nanopatterns. Latex particle lithography is a highly reproducible and robust method for patterning proteins, and serves as an excellent starting point for continuing to develop more complex bioassays. The periodicity and size of

nanostructures can be controlled by choosing the latex diameter and protein : latex ratios. Particle lithography has been used successfully to create arrays of BSA, IgG and mixed layers of BSA and SpA. Future investigations will address the suitability of particle lithography to other surfaces and proteins, for application in surface-bound immunoassays.

CHAPTER 3. ELUCIDATING THE ROLE OF SURFACE HYDROLYSIS IN PREPARING ORGANOSILANE NANOSTRUCTURES VIA PARTICLE LITHOGRAPHY

3.1 Introduction

The great promise of nanotechnology relies on capabilities to organize nanomaterials on surfaces to create assemblies with designed surface properties.[1-3] Currently, it is a challenge to control surface chemistry at the nanoscale for preparing functional systems for electronic,[4] optoelectronic,[5] biological,[6] or sensing[95] applications. Nanoscale lithography methods will facilitate development of well-defined molecular architectures that can be applied for devices such as protein chips[18, 96] or molecular junctions.[97-100] We have developed a new method for nanopatterning organosilanes using vapor deposition and particle lithography. Using colloidal masks produced by particle lithography, the placement of nanoscopic residues of water can be well-controlled to spatially direct the sites for hydrolysis of organosilanes. Silane nanopatterns produced by particle lithography exhibit highly reproducible geometries and enable nanoscale control of the surface chemistry of nanostructures.

Self-assembled monolayers (SAMs) furnish a model platform for engineering surfaces at the molecular level.[34, 101] Due to the ease of preparation and well-ordered structures, SAMs of *n*-alkanethiols[102] and *n*-alkylsilanes[33] have been used for surface modification, protein adsorption, and molecular device fabrication.[35, 103] Films of organosilanes resist oxidative and thermal degradation. The alkyl chain length and terminal moieties of silane SAMs can be tailored to suit experimental requirements. The covalent nature of siloxane bonds within silane SAMs provides stability and durability for nanostructures. Silane SAMs form siloxane bonds that anchor to the

surface and also cross-link to form interconnections with adjacent molecules. There is a competition for the formation of Si–O bridges to adjacent molecules, connections to the substrate or production of silanols, Si–OH. The amount of cross-linking depends on various conditions of sample preparation such as the nature of the substrate and immersion solvent and temperature.[104] The terminal moieties of silanes present various functional groups on surfaces, such as methyl, amine, glycol, etc., which offers extensive possibilities for generating SAM nanostructures with designed selectivity and reactivity. Substrates that have been used to prepare alkylsilane SAMs include silicon oxide, aluminum oxide, germanium oxide, quartz, glass, and mica.[34] For substrates that contain relatively few hydroxyl groups, such as mica(0001), prehydrolysis of alkylsilanes[105] or water vapor exposure to the surfaces[106] has been used to effect hydrosilation.

Organosilane monolayers can be prepared from solution[107-109] or vapor phase[110-112] to form densely packed monolayers. The molecular density and film quality of silane SAMs depends on parameters such as the amount of water, the temperature, the choice of immersion media, adsorption time, the type of organosilane molecule chosen, and the chemical nature of the surface.[104] In a densely packed silane SAM, the alkyl chains would be oriented nearly perpendicular to the substrate with a tilt angle of 0–5° (Figure 3.1).[34] A broad range of experimental conditions have been used to prepare organosilane layers and consequently the molecular organization, packing, and surface properties reported for the resulting structures have been inconsistent.[104] The self-assembly of octadecyltrichlorosilane (OTS) has been studied extensively using ellipsometry,[107, 109, 112-116] X-ray reflectometry,[109, 117, 118] infrared spectroscopies,[115, 116, 119] grazing incidence X-ray diffraction (GIXD),[118] neutron reflectivity,[120] X-ray photoelectron spectroscopy,[114] and atomic force microscopy (AFM).[109, 113, 114] In these reports, the thickness values ranged from to 2.25 to 2.81 nm for a SAM of OTS. The alkyl chains

22

adopt an all-trans configuration with tilt angle values reported that ranged from 0 to 17°. The range of measured values can be attributed to differences in surface coverage and diverse methods of sample preparation for OTS. In particular, the amount of water present in solvents is a critical parameter which affects formation of an organosilane monolayer.[121-123] The role of water in forming silane SAMs was reported by Sagiv, who observed that water adsorbed on a glass surface is necessary to initiate hydrolysis of OTS.[33] If too much water is present, polymerization of silanes to form polysiloxanes can occur in solution, rather than forming films on surfaces.[113, 121, 122]
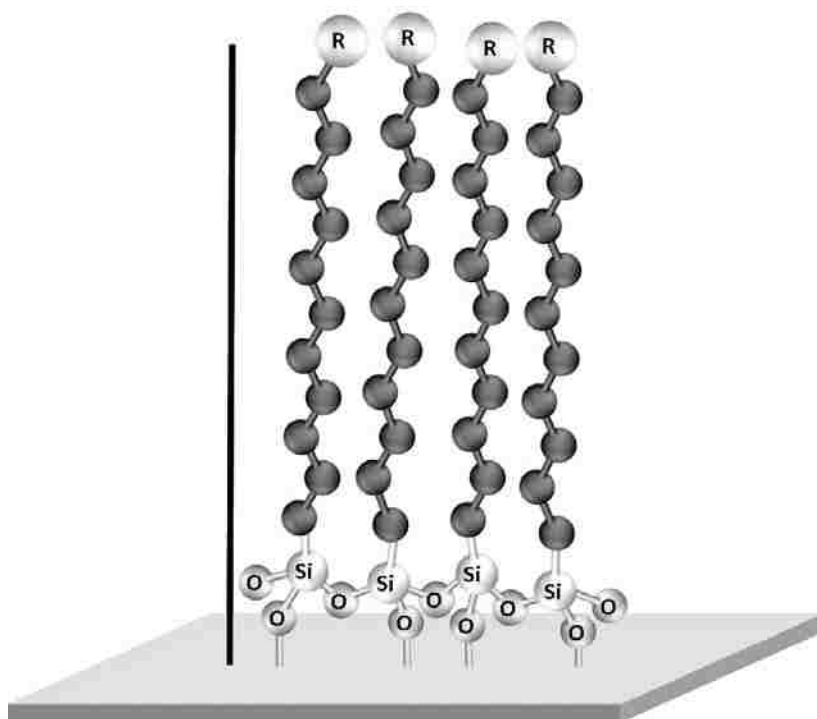
Figure 3.1 General structure of organosilane self-assembled monolayers.

The general steps of the hydrolysis of trichlorosilanes to form SAMs on surfaces are outlined in Figure 3.2.[33] Alkylsilane molecules react with a trace amount of water to bond covalently to surfaces. Silanol molecules produced by hydrolysis adsorb to surface reactive sites and undergo a condensation reaction with free hydroxyl groups. Each hydrolyzed silane

23

molecule can form siloxane bonds to anchor to the surface and also connect to neighboring molecules to form a network of Si–O–Si bridges. The chlorosilane groups can also convert to silanols or form additional linkages to the surface.[112] Trace amounts of water are essential to form densely packed silane monolayers and the quality of SAMs depends on the degree of hydration of the substrate.[121, 124, 125] To form organosilane SAMs, it can be difficult to control trace amounts of water to consistently produce high quality films with continuous well-packed domains of high density. Even ambient humidity can adversely affect the reproducibility of forming alkylsilane SAMs. In the absence of water, organosilane SAMs form incomplete monolayers and are generally of poor quality.
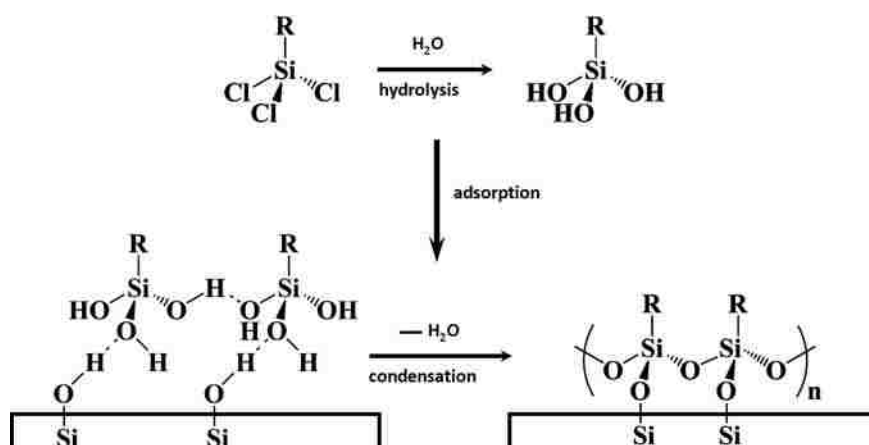
Figure 3.2 Generalized mechanism for the hydrolysis of trichlorosilanes on surfaces.[33]

A range of lithographic approaches have been applied for patterning organosilane monolayers. Photolithography with silane SAMs is accomplished by UV irradiation through photomasks.[15] Silane monolayers in exposed regions can be selectively removed via a photocleavage mechanism; the uncovered areas of the surface can then be used for further modification with different SAMs. Photolithography can also be applied to change the chemistry of surface head groups by UV-activated photochemistry.[126] The resolution of SAM patterns produced by photolithography is limited by diffraction of light sources and by the dimensions of

24

the photomasks. Electron beam lithography can overcome the diffraction limitation of light sources to generate smaller patterns with dimensions less than 100 nm.[110, 127, 128] However, e-beam lithography requires considerable training and expensive instrumentation. Approaches using soft lithography, such as microcontact printing with polydimethylsilane (PDMS) stamps have been applied successfully for patterning silane monolayers.[16, 129] The dimensions of silane patterns are limited to the size of the PDMS templates, typically at the micrometer scale. Also, one must choose solvents which do not dissolve PDMS for ink solutions. Approaches using scanning probe lithography (SPL) including Dip-Pen nanolithography,[17, 130] nanoshaving,[131, 132] bias-induced lithography,[21] and constructive nanolithography[20, 43, 133] have also been applied to write nanopatterns of silane SAMs. These methods provide exquisite nanoscale resolution and enable us to subsequently visualize the surface morphology with great detail. However, the patterns are fabricated one at a time, by slow serial writing processes which are not easily scaled to the high throughput and reproducibility needed for device manufacture.

Particle lithography or nanosphere lithography uses the arrangement of spherical particles to produce ordered arrays of regular nanostructures on surfaces.[22, 23] Monodisperse spheres self-assemble on flat surfaces into periodic structures with designed dimensions and interparticle spacing, which can then be used as structural templates or masks to guide the deposition of metals,[48-50] inorganic materials,[24-26] polymers,[27, 58, 134] catalysts,[55] and proteins.[29-31]

Molecules such as *n*-alkanethiol SAMs have been patterned using particle lithography. Colloidal masks were applied in a method of edge-spreading lithography (ESL) to produce nanosized rings on gold or silver surfaces.[28, 135] For ESL, a PDMS stamp was inked with alkanethiols and placed on a film of silica microspheres that had been dried on gold or silver surfaces. Alkanethiol molecules were delivered from the surface of the PDMS stamp through the

mesoparticle layer to the metal substrate to form circular patterns surrounding the areas masked by silica spheres. A method of contact angle lithography (CAL) was developed to produce pore-shaped structures of silane SAMs using silica particles as masks.[136] For this approach, silicon substrates coated with a mask of silica colloids were immersed in a toluene solution containing silanes. Silane molecules self-assembled in the interstitial areas of the surface between silica spheres. Immersion of colloidal masks can be a problem because of the buoyancy of the mesoparticles in various liquids. Silica and latex spheres rapidly detach from surfaces during immersion steps of particle lithography.

3.2 Experimental Approach

We introduce a new approach for patterning silane SAMs that combines particle lithography with vapor deposition to generate nanopatterns. The procedural steps are outlined in Figure 3.3. First, solutions containing monodisperse latex particles (Duke Scientific, Palo Alto, CA) are deposited on ultraflat surfaces. Ruby muscovite mica (Sand J and Trading Co., NY) and double-sided polished silicon(111) doped with boron (Virginia Semiconductor Inc., Fredericksburg, VA) were used for our investigations. Size-sorted monodisperse latex mesospheres (Duke Scientific, Palo Alto, CA) were initially washed with deionized water by centrifugation. The spheres form a pellet at the bottom of a microcentrifuge tube, which can then be resuspended in deionized water. Next, a drop of the mesoparticle suspension is placed on a substrate and dried at room temperature. As water evaporates during drying, capillary forces pull the mesospheres together to form organized crystalline layers on flat surfaces (Figure 3.3A).[137] The dried film of mesospheres provides a mask for evaporation. The dried masks of colloidal silica spheres are then placed into a sealed vessel containing a few drops of the alkylsilanes to be patterned. The molecules used for preparing nanopatterns, octadecyltrichlorosilane (OTS), 2-

[methoxy(polyethyleneoxy)propyl]trichlorosilane (PEG-silane), and *N*-(6-aminohexyl)aminopropyltrimethoxysilane (AAPTMS) were purchased from Gelest (Morrisville, PA). To generate a vapor, the reaction vessel was placed in an oven at 70 to 80 °C under ambient pressure (Figure 3.3B). During vapor deposition, organosilanes adsorb through self-assembly onto uncovered interstitial areas of the surface between latex spheres. The area of contact between the substrate and the base of the spheres is effectively masked to produce patterns with circular geometries. In the final step, the latex masks are removed completely by sonication and rinsing in ethanol (Pharmco, Aaper, TX). The silanes bond covalently to the substrates and are not displaced from the surface by the rinsing step. Depending on the drying parameters, arrays of rings or pore-shaped silane nanostructures are generated (Figure 3.3C).
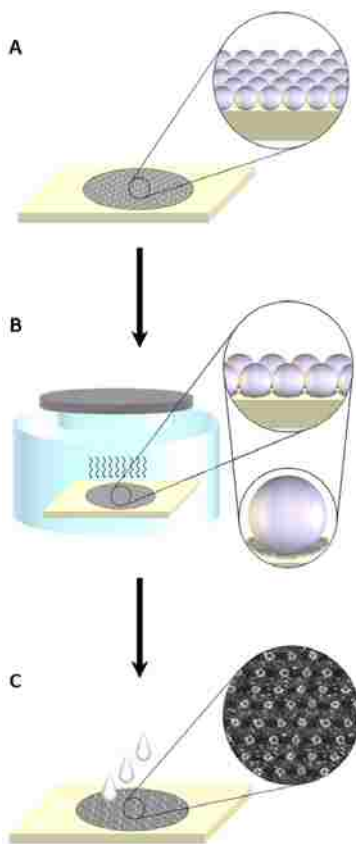
Figure 3.3 Steps of the new procedure for particle lithography. (A) A dried film of monodisperse latex spheres provides a mask for vapor deposition. (B) A vapor of alkylsilanes is generated by heating a sealed vessel. (C) The latex mask is rinsed away to reveal silane nanopatterns.

Silane nanostructures were imaged with a model 5500 atomic force microscope (AFM) (Agilent Technologies, Tempe, AZ) using acoustic AC-mode imaging, which operates the cantilever in the intermittent contact regime. For AC-mode AFM, the oscillation of the AFM tip is driven by applying an AC voltage to a piezoactuator. Rectangular silicon nitride cantilevers with force constants ranging from 21 to 98 N m^{-1} and a resonance frequency of 165 kHz were purchased from Nanosensors (Lady's Island, SC) and used for acoustic AC-mode imaging. Images were processed using Gwyddion (version 2.9) open source software, which is freely available on the Internet and supported by the Czech Metrology Institute.[138]

3.3 Results and Discussion

The surface coverage and geometry of OTS nanostructures on mica exhibit distinct differences when the latex masks were dried under different conditions (Figure 3.4). For latex masks that were dried briefly (20–60 min), arrays of OTS nanopatterns with pore-shaped morphologies were produced as shown in the AFM topography images of Figure 3.4A and B. A film of OTS with circular areas of uncovered substrate is revealed where the latex spheres were displaced. The thickness of the OTS layer is relatively even across the surface, uniformly covering the areas between the cavities where latex particles were displaced. The thickness of the film measures 2.2 ± 0.3 nm, referencing the uncovered areas of the substrate as a baseline (Figure 3.4C). Measurements of the periodicity of the nanopatterns were calculated by averaging the distances between the centers of the pores for at least 200 nanostructures from several representative areas of the surface. The average periodicity of OTS pores for the examples in Figure 3.4A, B measured 309 ± 8 nm and matches well with the expected diameter of the latex mesospheres (299 ± 6 nm). Small islands of OTS formed within the pores of the nanostructured film as shown in Figure 3.4B. If the latex spheres do not make tight conformal contact with the

substrate then water can be trapped underneath the spheres. With the vapor deposition process, OTS molecules bind at the site of water residues. Such islands were not observed for spheres that were smaller than 300 nm or when using polished silicon wafers as substrates.

Ring structures of OTS can be generated by drying the latex masks for 12 h as displayed in Figure 3.4D, E. Aligned rows and columns of ring patterns that form a hexagonal arrangement are generated with precisely replicated geometries. For masks that have been dried for several hours, AFM images reveal that OTS only binds in areas near the base of the latex spheres to form ring structures. The height of the rings measures 2.1 ± 0.4 nm (Figure 3.4F). The periodicity of the OTS rings for the sample of Figure 3.4D,E averages 311 ± 6 nm, which corresponds to the diameter of the latex spheres.

When masks of 300 nm latex were fully dried in an oven (95 °C, 24 h), OTS nanostructures were not generated after exposure to silane vapors as viewed in Figure 3G, H. The cursor profile (Figure 3.4I) provides further evidence that OTS structures did not form. A few loose adsorbates are present on the surface that affects tip adhesion; however there is no evidence of defined periodic structures present in AFM topographs. With oven-dried latex templates, the topographic images of Figure 3.4G, H do not exhibit a surface morphology that is representative of covalently bound OTS on mica(0001).[131, 139]

For organosilanes to bind to substrates, nanoscopic amounts of water are needed to initiate surface hydrolysis. After vapor deposition, AFM images clearly display surface areas with residues of water as viewed for silane nanostructures in Figure 3.4. These results demonstrate that the amount of water on surfaces is a critical parameter for controlling the sites for hydrolysis of OTS. For latex masks that have been dried briefly, water is distributed homogeneously throughout areas of the surface to enable molecular self-assembly of a thin film covering

interstitial areas between mesoparticles. As vapors are introduced, OTS assembles surrounding

the base of the masks and also binds to any uncovered areas of the surface between latex spheres.

Only the areas masked by the latex spheres are protected from silane adsorption. When colloidal

masks are dried under ambient conditions (25 °C, relative humidity ~60%) for longer intervals,

(12-24 h), most of the water evaporates from the surface. Only tiny residues of water persist to

form a circular meniscus in areas surrounding the base of latex spheres. When the partially dried

latex masks are exposed to OTS vapor, hydrolysis occurs only where water is present: at the base

of spheres. For latex masks that were oven-dried (95 °C, 24 h), nanostructures of OTS did not

form in the absence of water.
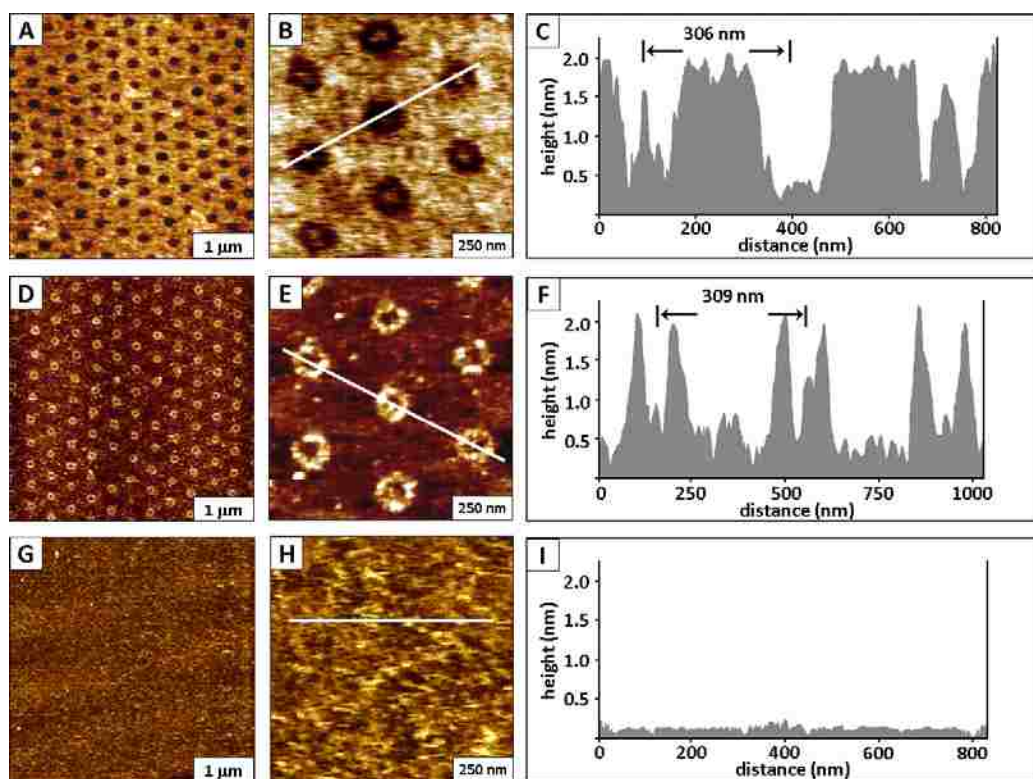
Figure 3.4 Differences in nanopattern morphologies with various drying conditions. (A) Octadecyltrichlorosilane nanopatterns produced on mica(0001) using a 300 nm latex mask that was dried briefly, 20 min; (B) zoom-in view; (C) corresponding cursor profile for panel B. (D) ring-shaped nanopatterns fabricated using 300 nm latex masks dried under ambient conditions for 12 h. (E) close-up view of hexagonal arrangement of rings; (F) cursor profile for panel E. (G, H) patterns did not form on mica surfaces when latex masks were dried in an oven; (I) cursor profile for the line in panel H.

Particle lithography was also applied successfully for organosilanes with different functional headgroups, such as 2-[methoxy(polyethyleneoxy)propyl]trichlorosilane (PEG-silane). Poly-(ethylene glycol) silanes are used as coatings for microfluidic devices, microarrays, and biosensors to reduce nonspecific adsorption of biomolecules or cells onto surfaces while maintaining a hydrophilic, biocompatible surface.[140, 141] A generic approach used for surface-bound protein assays is to pattern PEG silanes to prevent nonspecific binding of proteins.[142] An example of periodic arrays of PEG-silane rings that were fabricated on silicon substrates using 100 nm latex particles is shown in Figure 3.5. The latex masks were dried for 24 h in ambient air, which produced individual ring-shaped nanostructures throughout areas of the surface. The long-range order and organization of PEG-silane rings is apparent in the successive zoom-in views (Figure 3.5A, B, C) with only a few defects produced by missing particles. Other researchers have developed approaches to minimize the density of defects for particle lithography by using fabrication steps with convective assembly[143] or Langmuir-Blodgett troughs.[144] The phase image of Figure 4E displays differences in elastic response between PEG rings and uncovered areas of the substrate. The uniform contrast of the surfaces of the rings indicates that the chemistry is homogeneous. The height of the PEG-silane rings measures 8.3 ± 0.8 nm with an average periodicity of 107 ± 5 nm (Figure 3.5D) which corresponds well with the expected diameter of the latex masks (97 ± 3 nm). The width of the PEG-silane rings measures 67 ± 8 nm with an inner pore diameter of 31 ± 4 nm. The width of gap in between adjacent rings measures 18 ± 5 nm. There are 19 PEG-silane rings within the 0.5×0.5 μm^2 frame of Figure 3.5C, whereas the larger 8×8 μm^2 area of Figure 3.5A has 4870 ring patterns. This yields an estimated ring density of 7.6×10^9 nanostructures per 1×1 cm^2.
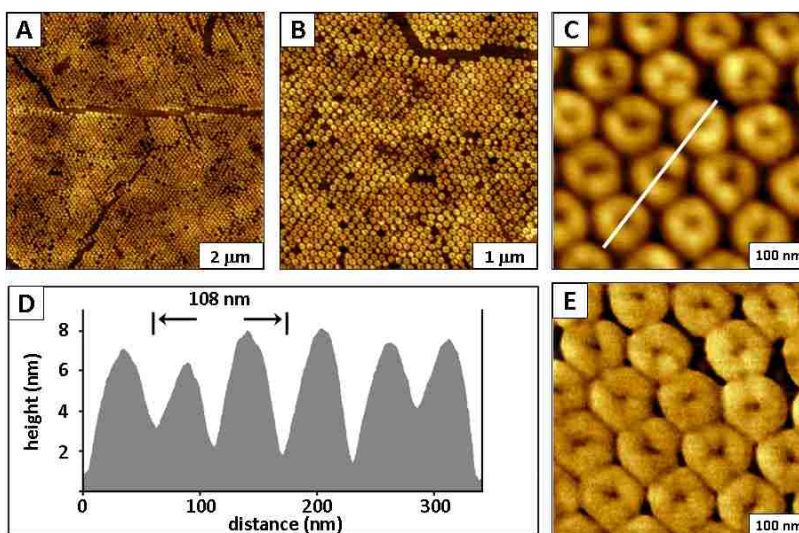
Figure 3.5 Rings of PEG-terminated silane SAMs prepared with 100 nm latex masks. (A) Long range order and packing of ring structures; (B) close-up view of nanopatterns; (C) zoom-in of 100 nm rings; (D) cursor profile for the line in panel C; (E) phase image of panel C.

Amine-terminated silane nanostructures can also be produced by particle lithography combined with vapor deposition. Periodic arrays of rings of *N*-(6-aminohexyl)aminopropyltrimethoxysilane (AAPTMS) were prepared on silicon surfaces using 150 nm latex masks that had been dried in air for 24 h (Figure 3.6). Within the 8 × 8 μm^2 topography image of Figure 3.6A there are 2310 rings, evidencing the high-throughput capabilities of particle lithography. The ring-shaped geometry of AAPTMS nanopatterns is highly consistent, shown by successive zoom-in views of Figure 3.6A, B, C. The average width of the AAPTMS rings formed by 150 nm latex spheres measures 117 ± 7 nm, and the size of pores within the rings is 56 ± 9 nm. The average periodicity of 155 ± 8 nm measured for the arrays of AAPTMS nanopatterns corresponds closely to the dimensions of the latex masks (151 ± 4 nm). The zoom-in topography (Figure 3.6C) and corresponding phase image (Figure 3.6E) reveal that the rings do not touch neighboring patterns. Phase images distinguish differences in surface chemistry and elastic response. The AAPTMS rings have a uniform surface composition

with a brighter contrast relative to the uncovered areas of silicon between the nanopatterns. The height of the AAPTMS nanopatterns measures 3.7 ± 0.5 nm (Figure 3.6D), which is taller than the expected dimensions for a single layer of AAPTMS (~2.0 nm).
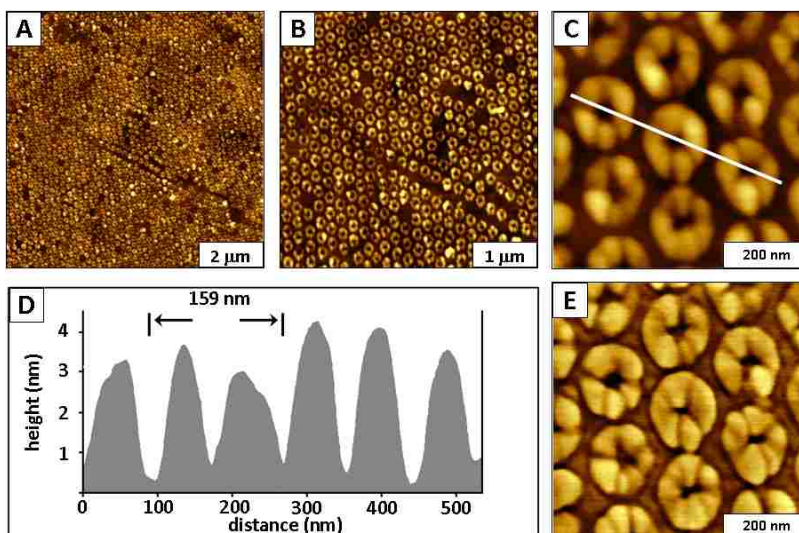
Figure 3.6 Amine-terminated silane nanopatterns produced using 150 nm latex masks. (A) Broad view of ring-shaped nanopatterns; (B) zoom view of silane nanostructures; (C) hexagonal arrangement of rings; (D) cursor plot for panel C; (E) phase image of panel C.

3.4 Conclusion

Particle lithography is a practical approach for fabricating nanopatterns with designed surface chemistry. Nanopatterns of organosilane SAMs can be generated reproducibly by combining particle lithography with chemical vapor deposition. The placement of water adsorbed to surfaces is a critical factor for determining the sites of hydrosilation to form silane nanostructures via vapor deposition. A general observation is that the surface morphologies were highly consistent and reproducible for a specific drying condition and particle diameter. Once the experimental conditions are optimized, dozens of samples prepared with the selected conditions exhibit identical nanoscale morphologies. The geometry of alkylsilane nanopatterns is determined by the drying conditions of the latex masks. The drying parameters provide a means to control the distribution and placement of nanoscopic residues of water. Silanes bind only to

33

the areas of the surface containing trace amounts of water, since water is essential for hydrosilation. By adjusting the time interval for drying the masks, nanoscopic residues of water on surfaces can be retained near the bases of spherical masks to spatially direct the sites for hydrosilation. The surface density, as well as the size and periodicity of the nanostructures can be selected by choosing various latex diameters. In future work, patterns of organosilane SAMs will be used as a foundation to attach metals, organic molecules and nanomaterials in well-defined surface architectures.

CHAPTER 4. NANOSTRUCTURES OF OCTADECYLTRISILOXANE SELF-ASSEMBLED MONOLAYERS PRODUCED ON AU(111) USING PARTICLE LITHOGRAPHY

4.1 Introduction

Self-assembled monolayers (SAMs) provide an ideal platform for engineering surfaces at the molecular level and provide a vehicle for investigating reactions on surfaces.[34, 35, 103] Well-defined organosilane self-assembled monolayers on oxide surfaces were first reported by Sagiv in 1980.[33] Since then, organosilane SAMs have become widely applied for surface passification and photoresists.[15, 35, 145] Organosilanes also provide a versatile molecular platform which can be applied for surface patterning and nanofabrication.[15-17, 20, 128] The interfacial functionalities of organosilane SAMs are tailorable for designing surface chemistries to attach various nanomaterials.[146-149] The robust covalent nature of organosilanes offers extensive mechanisms for further steps of chemical modification for designing surface chemistry at the nanoscale.[107, 133, 150-152]

The precise mechanism for surface assembly of organosilanes is not fully understood, and is complicated by parameters of sample preparation such as the nature of the immersion solvent and surface.[104] Organosilane SAMs are formed through hydrolysis reactions to make bridging siloxane bonds that anchor to the surface and also cross-link to form interconnections with adjacent molecules. Water is known to have an essential role in the self-assembly of organosilanes on surfaces.[113, 123-125, 153, 154] Nanoscopic amounts of water are essential for initiating a surface hydrosilation reaction; however, excess water can induce polymerization reactions to generate multilayers and branched structures. As silane SAMs are formed, there is a

competition between forming Si-O bridges to adjacent molecules, connections to the substrate or production of silanols, Si-OH.[33, 121, 122] Typical substrates used to prepare SAMs of organosilanes are silicon, quartz, glass, metal oxides, and mica.[34, 35] For substrates that contain relatively few hydroxyl groups, such as mica(0001), prehydrolysis of organosilanes[105] or exposure of the surfaces to water vapor[106] have been used to effect surface hydrosilation.

There are sparse reports which evidence that organosilanes such as octadecyltrichlorosilane (OTS) can be prepared on gold substrates in ambient environments, and for these accounts, the surface coverage and quality of the organosilane films has not been documented with scanning probe characterizations. Previously, it was considered that surfaces with free hydroxyl groups were required to form SAMs of organosilanes. This view was adjusted when organized monolayers of OTS were shown to form on gold, which is a substrate devoid of hydroxyl groups.[115, 155-158] In these reports, it was demonstrated that OTS molecules assemble on a thin film of water adsorbed on the gold surface rather than on the gold substrate itself. Functionalized organosilanes such as (3-aminopropyl)triethoxysilane (APS) or trimethylsilyacetylene (TMSA) also have been reported to form SAMs on gold surfaces.[159, 160] Reflection absorption infrared spectroscopy (RAIRS), ellipsometry, contact angle and quartz-crystal microbalance (QCM) studies reveal that APS adsorbed on gold to yield multilayer films.[159] For TMSA, scanning tunneling microscopy (STM) results indicate that SAMs of TMSA are generated with Si-Au chemical bonds.[160] In the absence of water under ultra-high vacuum (UHV) conditions, it was demonstrated that alkylsilanes ($H_{2n+1}C_nSiH_3$) formed a monolayer on gold through Si-H bond activation when deposited at room temperature.[161-163] Results with X-ray photoelectron spectroscopy (XPS) reveal that the silicon headgroups attached to the gold surface

to form a film. However, for samples prepared in UHV, characterizations with RAIRS and STM indicate that the alkyl chains form disordered monolayers as compared to alkanethiol SAMs.

The nature of gold surfaces limits applicability for surface reactions with organosilanes. Among the properties of gold surfaces, wettability has generated considerable controversy in literature reports.[164-168] With different techniques applied to measure the wettability of gold under varied conditions, reports for the contact angle of gold surfaces range from 0 to 65 degrees.[164-166, 169-171] A hydrophilic gold surface can be obtained after tedious cleaning processes, such as exposure to oxygen plasma,[156, 158, 172] piranha solution,[173] or ultraviolet (UV) irradiation.[174, 175] Gold surfaces were reported to have a contact angle of 0 degrees immediately after removal from vacuum, which rapidly increased to 40 degrees with exposure to the atmosphere.[168] Under ambient conditions complete wetting of gold is not achieved due to adsorption of organic molecules from the environment.[168] As a consequence, silanization of gold surfaces through hydrolysis to form dense, high quality SAMs is problematic, due to difficulties in achieving a consistent distribution of water throughout areas of the hydrophobic surface.

In this chapter, we present a facile high-throughput approach for preparing octadecyltrisiloxane nanostructures on surfaces of gold by combining particle lithography with vapor deposition of organosilanes.[36] To improve the wettability of the Au(111) surface, the substrates were exposed to UV irradiation before depositing aqueous solutions of latex. Essentially, the evaporative masks of latex produced with particle lithography were used to define the surface sites of nanoscopic residues of water. Successful results for preparing OTS nanopatterns are demonstrated with contact-mode AFM characterizations. Mechanism for water-directed assembly of OTS will also be discussed. The conductive nature of the gold

substrates further enabled protocols for current imaging and current-sensing AFM with the test platforms of OTS nanopatterns.

4.2 Experimental Section

4.2.1 Materials and Reagents

Octadecyltrichlorosilane was purchased from Gelest (Morrisville, PA) and used without further purification. Certified particle size standards of polystyrene latex (300 nm) were obtained from Duke Scientific (Palo Alto, CA). The latex particles were washed twice by centrifugation with deionized water (Milli-Q, Millipore, Bedford, MA) to remove possible contaminants such as charge stabilizers or surfactants. Gold thin films evaporated on mica substrates with thickness of 150 nm were obtained from Agilent Technologies Inc. (Chandler, AZ, USA). Ethanol (ACS grade, Pharmco, Aaper, TX) and toluene (reagent grade, EMD Chemical Inc., Gibbstown, NJ) were used to rinse samples.

4.2.2 Atomic Force Microscopy

Topography, friction and current-sensing AFM (CS-AFM) images were acquired using an Agilent 5500 scanning probe microscope equipped with PicoScan v5.3.3 software (Agilent Technologies Inc., Chandler, AZ). Silicon nitride tips with an average force constant of 0.5 N m^{-1} were used for contact mode AFM imaging in air (MSCT-AUHW, Veeco Instruments, Inc., Camarillo, CA). The silicon nitride probes used for contact mode AFM were coated with OTS to minimize tip-surface adhesion; and the total forces applied for imaging were < 1 nN. Current-sensing AFM was used to map the sample conductance while operating in contact mode. Different bias voltages (+6 V, 0 V and -6 V) were applied to the samples for acquiring CS-AFM data. The tips used for CS-AFM were highly doped silicon probes with a Ti/Pt coating with an average force constant of 0.2 N m^{-1} (ANSCMPC, Nanoscience Instruments, Inc., Phoenix, AZ).

Images were processed using Gwyddion (version 2.10) open source software supported by the Czech Metrology Institute, which is freely available on the internet.[138]

4.2.3 Particle Lithography

Particle lithography combined with vapor deposition was used to generate octadecyltrisiloxane nanostructures on gold substrates. Particle lithography, also known as nanosphere lithography uses the natural arrangement of spherical particles to produce arrays of nanostructures on surfaces.[22, 23, 176] Monodisperse particles self-assemble into periodic structures on flat surfaces to guide the deposition of various materials, such as SAMs,[28, 36, 135, 136] proteins,[30-32] inorganic materials[24, 48] and polymers.[27, 177] An overview of steps for particle lithography with vapor deposition is shown in Figure 4.1. To prepare nanostructures, the gold surfaces were exposed to ultraviolet light (254 nm) for 4 h. Next, a 20 µl volume of an aqueous solution containing (2%, w/v) polystyrene latex particles (300 nm) was immediately deposited on clean gold substrates with a micropipette (Figure 4.1A). A view of a 300 nm latex mask is shown within the area of the circle (topograph). The sample was then dried in ambient conditions (25 °C, relative humidity ~60%) for 2 h. As water evaporates during drying, capillary forces draw the latex spheres together to form organized crystalline layers (Figure 4.1A). Trace residues of water persist at the base of latex spheres to form a circular meniscus. The dried film of latex was then used as an evaporative mask for vapor deposition of organosilanes (Figure 4.1B). To accomplish the vapor deposition, the colloidal masks were placed into a glass vessel containing 300 µL of neat OTS. The reaction vessel (a glass jar) was sealed and placed in an oven at 70°C for 8 h to generate a vapor. During heating, the OTS vapors attach to the exposed areas not masked by latex spheres and bind covalently at sites containing water residues (Figure 4.1B). The mask of latex particles was removed by sonication in ethanol for 2 min followed by

further rinsing with deionized water, ethanol and toluene (Figure 4.1C). Nanopatterns of OTS were not removed from the surface by the rinsing procedure.
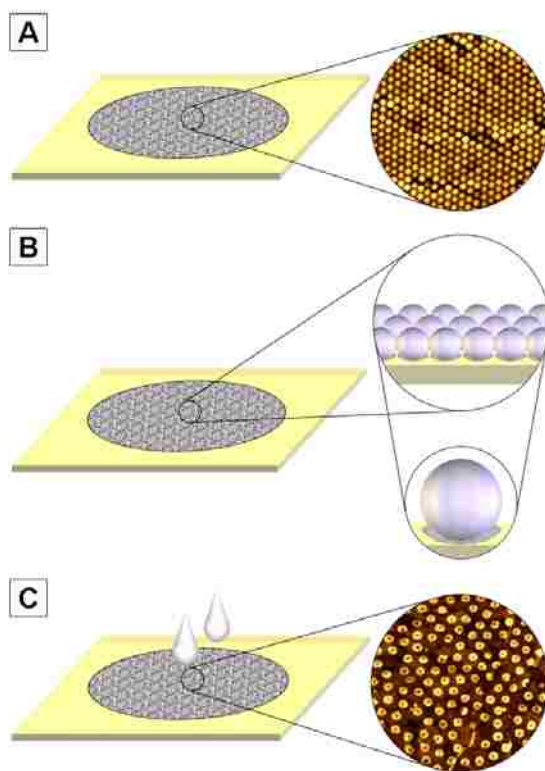
Figure 4.1 Steps of particle lithography for fabricating organosilane nanostructures on Au(111). (A) A mask of latex spheres was prepared on a ultraviolet-treated gold substrate; (B) after organosilane vapor deposition; (C) after rinsing, latex masks were selectively removed to reveal organosilane nanopatterns.

A control sample of an OTS film on Au(111) was prepared to match the conditions of the samples prepared by particle lithography, omitting the particle lithography step. To prepare control samples, the gold substrates were exposed to ultraviolet light of (254 nm) for 4 h. A volume of 20 μl of deionized water was then placed on the UV-treated gold substrates using a micropipette. The sample was dried in ambient conditions (25 °C, relative humidity ~60%) until the water evaporated (~35 min). The gold substrate was then placed inside a glass vessel containing 300 μL OTS. The vessel was sealed and placed in an oven and heated at 70 °C for 8

h. After vapor deposition was completed, the samples were rinsed with deionized water, ethanol and toluene.

4.3 Results and Discussion

Successful examples of ring-shaped nanostructures of OTS produced on Au(111) using particle lithography combined with chemical vapor deposition (300 nm latex masks) are demonstrated in Figure 4.2. Arrays of octadecyltrisiloxane nanostructures with ring-shaped morphologies are observed on the gold surfaces with irregularly shaped terraces. An AFM topograph of 893 rings produced within a 10 x 10 μm^2 area is shown in Figure 4.2A, which would scale to approximately 10^8 rings per cm^2. The arrangement of the organosilane rings conforms to the periodicity of the latex mask. The pores of the rings pinpoint the locations where the individual latex particles were rinsed away. The long-range order and organization of octadecyltrisiloxane rings are apparent, evidencing a few defects produced by missing particles. The hydrophobic nature as well as local defects of the gold substrate influences the long range periodicity and packing density of latex mesospheres. A few faint line patterns of OTS formed at the edges of gold terraces, defining the areas of the substrate that contained water residues.

The changes in surface chemistry between the organosilane rings and the gold substrate are viewed in the frictional force image of Figure 4.2B. Friction images result from differences in surface adhesion between the tip and sample, providing a sensitive map of changes in surface chemistry. Friction images also can reflect changes resulting from surface topography such as edge effects. The outlines of the nanopatterns predominate for the ring patterns, with bright or dark contrast at the pattern edges, as the tip travels up or down across the patterns. The edge effects are produced for the frictional force image due to changes in tip-surface interactions as the probe is scanned over the nanostructures, providing a precise outline of the ring geometries.

A hexagonal arrangement of rings is visible in the zoom-in topography image (Figure 4.2C) and corresponding cursor profile (Figure 4.2D). The shapes and dimensions of the nanopatterns are exquisitely reproducible at the nanoscale, with regular diameters of 246 ± 6 nm and the pore areas inside the rings of 48 ± 4 nm. The lateral periodicity measures 321 ± 13 nm between neighboring nanostructures, which matches closely with the 300 nm diameter of the latex masks. The average height of the rings is 3.7 ± 0.6 nm, which is slightly higher than the theoretical height of OTS (2.8 nm). In the zoom-in AFM image and cursor profile, it is apparent that at the nanoscale, the rings vary by as much as 1.2 nm in height. The height variability indicates branching within the siloxane network.
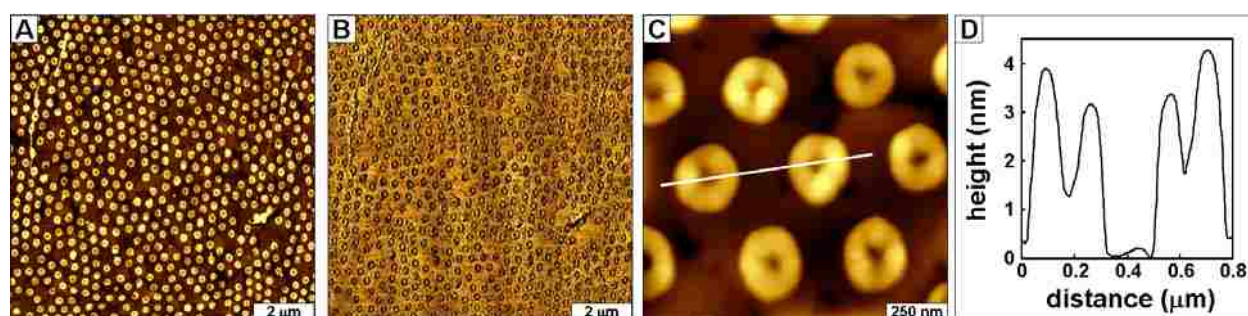
Figure 4.2 Ring-shaped nanostructures of octadecyltrichlorosilane prepared on gold using particle lithography combined with vapor deposition. (A) Wide area topograph; (B) corresponding frictional force image; (C) zoom-in view; (D) cursor profile for the line in panel **C**.

A control experiment was conducted without using a latex mask to further elucidate the role of water and surface wettability for self-assembly of OTS on Au(111). The Au(111) substrates were similarly exposed to ultraviolet light as in Figure 4.3, however the surface was moistened by applying a drop of water (20 µL) and allowing it to dry. The water droplet was dried in ambient conditions for 45 min and then placed into a sealed vessel containing 300 µL OTS for heated vapor deposition. Representative images of similar size areas of a bare gold substrate, control sample and OTS nanopatterns are compared side-by-side with contact-mode AFM topographs in Figure 4.3. The morphology typical of a vacuum-deposited gold/mica is revealed

42

in Figure 4.3A for the untreated Au(111) surface, exhibiting irregularly shaped terrace domains. The RMS roughness measured 2.9 nm for the area shown. After vapor deposition, a clustered, irregular morphology was revealed, with incomplete surface coverage of random island protrusions throughout terrace and step edge areas (Figure 4.3B). Protrusion islands of OTS are evident throughout areas of the surface, measuring 2.2 ± 0.4 nm in height, referencing shallower areas of the surface as a baseline. The baseline areas are not bare gold, the sample contains near complete surface coverage of an octadecyltrisiloxane film. The thickness of the OTS films is variable, which is likely caused by nanoscale variations in the distribution of water present on the surface. A comparable size area with octadecyltrisiloxane nanostructures is presented in Figure 4.3C, showing 132 rings of OTS. The nanostructures cover ~33 % of the surface and exhibit remarkably uniform thickness and geometries. Long-range order and regular spacing between the ring patterns of OTS are apparent throughout areas of the 1 x 1 cm^2 sample, with few defects.
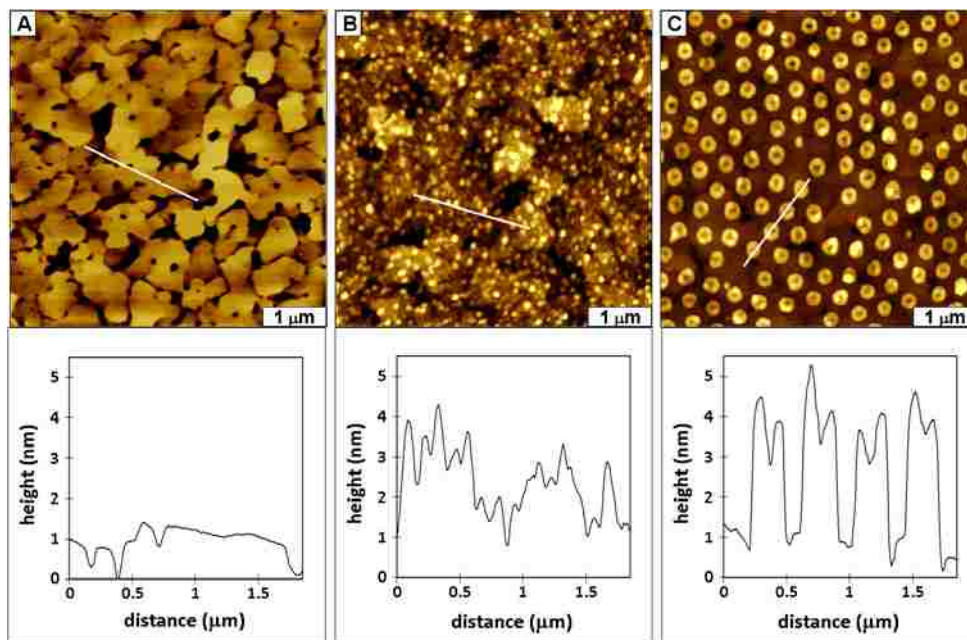
Figure 4.3 Water directed assembly of OTS on oxidized surfaces of Au(111) viewed for 5 x 5 μm^2 AFM topographs. (A) Untreated Au(111) substrate; (B) OTS film produced using vapor deposition without steps of particle lithography; (C) Ring-shaped nanostructures of OTS produced by vapor deposition through latex mask.

Characterizations with current-sensing atomic force microscopy (CS-AFM) were used to evaluate the conductivity of the OTS ring patterns (Figure 4.4). For CS-AFM, a bias voltage is applied to the substrate, and the current through the molecular film is measured when the AFM tip is placed in direct contact with the surface. For comparative reference, a topography image ($2.5 \times 2.5 \ \mu m^2$) acquired using the same metal-coated probe is presented in Figure 4.4A, which displays 51 rings of OTS arranged in diagonal rows and columns. The third horizontal row is shifted slightly downwards in alignment, providing a convenient *in situ* landmark for comparing the different data channels. The same scan area was imaged successively for the current frames. Current images display highly conductive regions as bright or dark features, depending on the bias polarity. As the polarity of the sample bias was switched from −6 V to +6 V, the contrast correspondingly changed. For measurements with CS-AFM, the metal-coated tip remains at virtual ground as a bias is applied to the sample. The current signal is positive when the sample surface is biased negatively, and reversed contrast is shown for opposite bias polarity. The bright areas of Figure 4.3B indicate that uncovered regions of the gold surface are highly conductive. When applying a positive voltage to the surface, the current likewise became negative. When the bias is zero, no contrast is visible for the current image (Figure 4.4C). With a positive bias, the bright contrast is attributable to less conductive areas as in Figure 4.4D. The current image in Figure 4D was acquired at +6 V and displays reverse contrast compared to Figure 4.4B.

The regions of the nanopatterns exhibit relatively homogeneous contrast in current images, in correspondence with observations of the regular surface topography and highly uniform thickness of the rings. The robust ring structures of OTS appear to be densely packed and were not observed to degrade despite repetitive AFM imaging in contact mode or at elevated bias.

44

The current contrast of the small pore areas within the rings matches the substrate, which is evidence that the mesosphere masks were cleanly removed to expose bare areas of the gold substrate. Nanopatterns of OTS prepared on Au(111) are suitable for investigations of charge transport and development of molecular scale measurements. Gold surfaces also furnish advantages as electrodes or for etching processes.
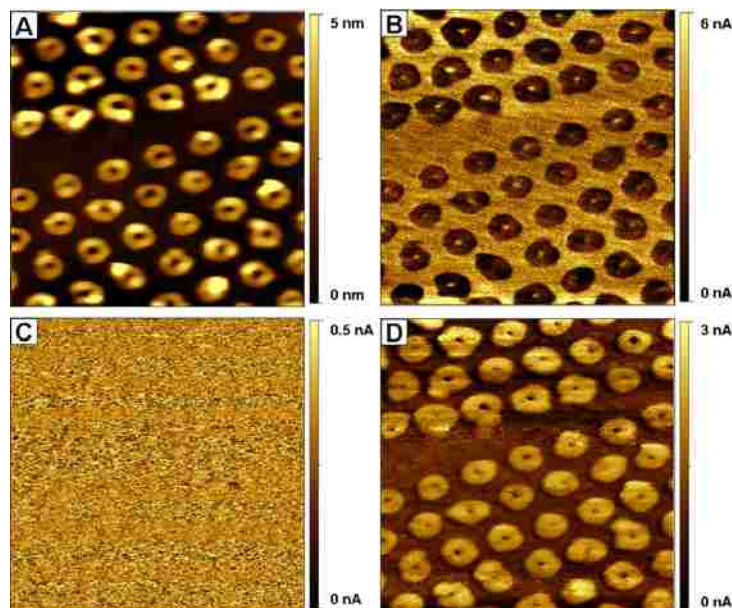
Figure 4.4 Evolution of changes in current-sensing AFM images acquired with various sample bias voltages. (A) Topography image of octadecyltrichlorosilane nanopatterns produced with 300 nm latex masks. Current-sensing images of octadecyltrisiloxane rings acquired with (B) −6 V, (C) 0 V and (D) +6 V for the same scan area.

The AFM probe can be placed directly on the surface of individual nanostructures to acquire local I-V spectra (Figure 4.5). Three rings were selected to evaluate the conductivity. The nanostructures selected for acquiring I-V spectra are identified in the topography image of Figure 4.5A. As the sample bias was scanned from −10 V to +10 V, slightly asymmetric, nonlinear I-V profiles were observed, comparing the forward and reverse bias sweeps (Figure 4.5B). The measurements match well with previously reported I-V spectra.[178-180] A sharp peak was observed between −4 V to −5 V which indicates the oxidation of OTS SAMs.[180] The

maximum current measured 1 ± 0.4 nA in both negative and positive bias regions, which displays the expected insulating nature of the alkyl chains of OTS.[181, 182] The bias values at the onset of current conduction from the I-V profiles were used to establish the conditions for acquiring current images for Figures 4.4B and 4.4D.
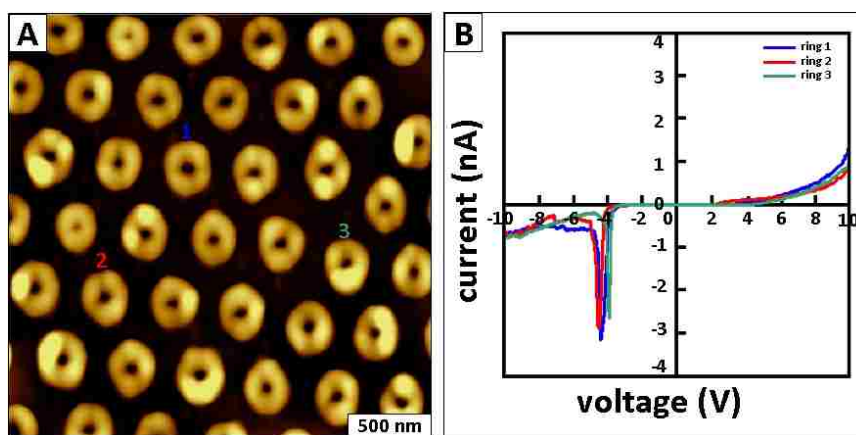
Figure 4.5 Current-sensing AFM measurements of octadecyltrisiloxane rings. (A) Topograph of the area selected for measurements; (B) current-voltage profiles acquired for three octadecyltrisiloxane nanostructures.

Approaches based on scanning probe lithography (SPL) have also been applied to produce organosilane nanopatterns.[21, 132, 133, 142] Methods of SPL provide exquisite nanoscale resolution and enable us to subsequently visualize the surface morphology with great detail. However, with SPL the patterns are fabricated one at a time, by slow serial writing processes which are not easily scalable for the high throughput and reproducibility needed for device manufacture. Approaches with particle lithography provide advantages of high throughput and reproducibility for generating millions of organosilane nanostructures, based on simple bench chemistry procedures. The size, shape and spacing of features can be precisely controlled with mesoparticle masks. Once the experimental conditions are optimized, dozens of samples prepared with the selected conditions exhibit identical nanoscale morphologies. Multiple samples were prepared, and images of Figures 4.2A and 4.4A are taken from samples prepared

46

separately on different days. The AFM views shown are representative of multiple areas throughout the surface.

The poor wettability of gold substrates in ambient conditions was addressed by ultraviolet light exposure, which is known to improve surface hydrophilicity and remove organic contaminants. During UV-irradiation, gold surfaces are oxidized, but recover hydrophilicity.[155, 175, 183, 184] In the presence of trace residues of water on oxidized gold surfaces, OTS molecules are hydrolyzed and reduce gold oxide with $SiCl_3$ moieties.[155, 156] Typically, trace amounts of water are required to form densely packed organosilane monolayers. The quality of organosilane SAMs depends on the degree of hydration on surfaces. For a substrate devoid of hydroxyl groups such as Au(111), UV surface treatment was used to improve the adhesion of water. With particle lithography, nanoscopic residues of water could be uniformly arranged and distributed throughout areas of the surface by latex mesoparticles to direct the binding of organosilanes.

With latex masks, nanoscopic amounts of water are spatially confined and retained underneath the spheres localized to a meniscus area at the base where the mesoparticles meet the surface. The masks were prepared by drying an aqueous solution of latex particles on the ultraviolet-treated gold substrate, under ambient conditions. During the drying step, most of the water evaporates from the surface and only tiny residues of water persist to form a uniform, circular meniscus near the base of latex mesospheres. The outer surfaces of latex spheres have sponge-like properties to absorb water, and retain small amounts of moisture when dried.[90, 91, 185, 186] When introducing OTS vapor to the latex masks, hydrolysis takes place selectively where water is present within the circular areas of the liquid meniscus. The shapes of the nanostructures correspond to the areas with a water meniscus near the base of the latex mesoparticles.

Surfaces with well-defined nanopatterns provide a platform for further chemical steps to adsorb proteins, nanoparticles or other nanomaterials. By selecting organosilanes with designed functionalities, nanoscale control of surface chemistry can be achieved. After organosilane nanopatterns are fabricated using particle lithography, uncovered areas of the Au(111) substrate are available for further steps of chemical patterning or etching. Circular organosilane nanostructures can be used as boundaries to isolate and direct adsorption of new materials in well-defined arrangements. Alkanethiol SAMs also can be deposited to backfill uncovered areas of the Au(111) substrate for defining surface selectivity at the nanoscale.

4.4 Conclusion

A robust, high-throughput nanofabrication approach was accomplished using steps of particle lithography combined with chemical vapor deposition to reproducibly generate periodic nanostructures of OTS on surfaces of Au(111). Pre-treatment of the gold substrates with UV-irradiation was used to improve surface wettability. Millions of OTS nanopatterns are produced with exquisitely regular and uniform geometries and arrangement. Current-sensing AFM measurements of nanostructures reveal the insulating nature of octadecylsiloxane on conductive gold surfaces.

CHAPTER 5. ELECTROLESS DEPOSITION OF METALS ON NANOPATTERNS OF ORGANOSILANE SAMS

5.1 Introduction

A current challenge in nanotechnology is to control surface chemistry at the nanoscale for fabricating functional nanostructures in electronic, optoelectronic, biological, or sensing applications.[3, 7, 187-189] Control of the relative position and orientation of nanomaterials on surfaces will contribute towards development of well-defined molecular architectures for protein chips or molecular junctions.[19, 87, 98] Advances in nanotechnology will depend on the ability to organize materials at the nanoscale to create designed functional assemblies that can display desirable properties and can be accurately replicated. Metal and semi-conductor nanomaterials demonstrate quantized electrical and optical properties that can be useful for future device applications.[8, 9, 44, 190] Surfaces with designed metal nanostructures can be used for fundamental investigations of chemical and physical properties such as magnetism, conductivity, and photonic properties.

Electroless deposition (ELD) is an autocatalytic redox process in which complexed metal ions are chemically reduced to metal at a surface without an external current source.[149, 191-197] The metal deposition process is usually initiated on a surface which contains active functional groups or catalysts. When immersing a substrate into an ELD solution, the reducing agent provides the electrons for converting metal ions into the metal at activated sites on the surface. The metal itself must also be catalytically active so that the deposition can continue to progress. Uniform metal coatings can be created over selected small areas using ELD. Processes using ELD have been applied widely in the electronic industry for metallization of plastics, ceramics,

Reproduced with permission from the Electrochemical Society.

and other insulating substrates.

We have developed a new approach to fabricate nanopatterns of metal nanostructures via electroless metallization on nanopatterned surfaces with organosilane thin films. Particle lithography using monodisperse latex particles as evaporative masks can be applied to pattern self-assembled monolayers (SAMs) of organosilanes on surfaces.[36] Different geometries of silane nanostructures are produced, depending on the spatial arrangement of nanoscopic residues of water surrounding the mesoparticle masks. Monodisperse latex spheres spontaneously self-assemble into crystalline arrays when dried, which furnish an evaporative mask to direct the surface sites for the hydrosilation reaction. Particle lithography can be applied to organize nanomaterials on surfaces with exquisite control of surface arrangements and chemistry. Not only are nanostructures produced with defined geometry and arrangement, particle lithography also enables one to define the surface chemistry and consequently the reactivity of the patterns for binding other molecules, nanomaterials and metals. Selective metallization of nanopatterns using ELD can produce nanostructures which are a few nanometers in thickness, by controlling parameters of solution chemistry. Results from atomic force microscopy (AFM) characterization will be presented which demonstrate the selectivity for ELD on organosilane nanopatterns.

5.2 Experimental Section

5.2.1 Materials

Octadecyltrichlorosilane (OTS) and 3-mercaptopropyltrimethoxysilane (MPTMS) were purchased from Gelest (Morrisville, PA) and used without further purification. Iron (II) chloride tetrahydrate, sodium nitrite and sodium acetate were obtained from Sigma-Aldrich (St. Louis, MO). Ruby muscovite mica (S&J Trading Co., NY) and double-sided polished silicon(111) wafers doped with boron (Virginia Semiconductor Inc., Fredericksburg, VA) were used as

substrates. Silicon wafers were cut (1×1 cm^2) and cleaned by immersing in piranha solution for 1 h. Piranha solution is highly corrosive and should be handled carefully, it is a mixture of sulfuric acid (96%, EMD Chemical Inc., Gibbstown, NJ) and hydrogen peroxide (30%, Sigma-Aldrich) at a (v/v) ratio of 3:1. Silicon substrates were then rinsed with deionized water (Milli-Q, Millipore, Bedford, MA). Monodisperse polystyrene latex solutions were purchased from Duke Scientific (Palo Alto, CA). To remove contaminants such as charge stabilizers or surfactants the latex particles were washed twice with deionized water by centrifugation. Ethanol (Pharmco, Aaper, TX) and toluene (EMD Chemical Inc., Gibbstown, NJ) were used to rinse samples.

5.2.2 Sample Preparation

Several chemistry steps using particle lithography, solution self-assembly and ELD were used successively to fabricate metal-organic nanostructures. Particle lithography combined with vapor deposition can be applied to nanopattern organosilanes on silicon(111).[36] The nanopatterned surfaces are then exposed to a second organosilane by solution immersion. Finally, ELD was used to selectively generate metal deposits on nanopatterned surfaces of silicon.

5.2.3 Particle Lithography Combined with Vapor Deposition of OTS

In the first step, an aqueous solution containing purified monodisperse latex particles (150 nm) was deposited on clean silicon substrates or freshly cleaved pieces of mica. Next, the samples were dried in air for 1-12 h. As water evaporates during drying, capillary forces draw the latex spheres together to form organized crystalline layers on flat surfaces. The film of ordered latex particles provides an evaporative mask for vapor deposition of organosilanes. Next, the dried colloidal masks were placed into a reaction vessel containing 300 μL OTS. To generate a vapor, the reaction vessel was placed in an oven at 70 °C under ambient pressure. During heating, the vapors of OTS molecules adsorb to the interstitial areas between latex

spheres and bind covalently to the substrate. Next, the mask of latex particles was removed by sonication in ethanol for 15 min followed by further rinsing with ethanol and deionized water. Nanopatterns of octadecyltrichlorosilane were not removed from the surface by the rinsing procedure.

5.2.4 Deposition of a Reactive Silane by Immersion Self-Assembly

Areas of the surface that were not covered with OTS were filled with thiol-terminated MPTMS by solution self-assembly via immersion. Substrates with OTS nanopatterns were immersed for 4 h in a solution containing 0.1 mM MPTMS prepared in toluene. Afterwards, the samples were cleaned by sonication for 15 min in toluene and ethanol, respectively.

5.2.5 Selective Electroless Deposition of Iron Oxide

Deposits of iron oxide (Fe_3O_4) were produced using ELD for organosilane nanopatterns on silicon surfaces. A solution of 30 mM sodium nitrite and a solution containing 10 mM iron(II) chloride tetrahydrate in a 65 mM sodium acetate buffer at pH 7.4 were prepared for ELD. Nanopatterned silicon substrates were immersed in a mixture of the two solutions at a v/v ratio of 10:1 $FeCl_2$: $NaNO_2$. The reaction was performed at 70 °C for 25 min. After ELD was completed, the samples were rinsed with deionized water and dried in air.

5.2.6 Sample Characterization

Organosilanes and metal nanostructures were characterized with a model 5500 scanning force microscope (Agilent Technologies, Tempe, AZ) using acoustic AC-mode AFM, which operates the cantilever in the intermittent contact regime. Rectangular silicon nitride cantilevers with force constants ranging from 21 to 98 N m^{-1} and a resonance frequency of 165 kHz were purchased from Nanosensors (Lady's Island, SC) and used for AC-mode imaging. Images were

processed using Gwyddion open source software, which is freely available on the internet and supported by the Czech Metrology Institute.[138]

5.3 Results and Discussion

5.3.1 Controlling Nanopattern Morphologies via Surface Hydrosilation

Particle lithography, which is also known as nanosphere lithography uses colloidal masks to produce ordered arrays of regular nanostructures on surfaces.[22, 198, 199] Monodisperse spheres self-assemble on flat surfaces into periodic structures with designed dimensions and interparticle spacing, which can then be used as structural templates or masks to guide the deposition of metals,[48, 200] inorganic materials,[24, 25] polymers,[27, 201] catalysts,[55, 202] proteins[30, 31] and organosilanes.[36, 136] The various steps of particle lithography can be characterized using AFM. A view of an evaporative mask is presented in Figure 5.1 for 150 nm latex particles. The top-view of latex spheres shown by the AFM topography image displays the two-dimensional close-packed organization of mesospheres, exhibiting long-range order with few defects or missing particles (Figure 5.1B). The AFM topograph shows the ordering of the top-most layer, whereas the organosilane patterns are formed at the bottom surface layer of mesospheres. Even for mesospheres as small as 150 nm, a close packed crystalline mask is produced by simply drying an aqueous solution of latex (Figure 5.1B). The diameter of the latex spheres defines the periodicity of the nanopatterns; however, the final size of the surface patterns is determined by the actual physical area of contact between the spheres and substrate.

To spatially control the deposition of metal on surfaces with nanoscale reproducibility, particle lithography combined with vapor deposition was used to define the surface chemistry and control the nanopattern geometry (e.g. pitch, diameter). Self-assembled monolayers of organosilanes offer advantages such as resistance to oxidative or thermal degradation and

capabilities to tailor the surface chemistry with further steps of chemical modification. The surface coverage and geometry of OTS nanostructures on mica exhibit distinct differences when the latex masks were dried under different conditions (Figure 5.2). By controlling the drying conditions of the latex masks, nanoscopic amounts of water can be used to direct the placement of nanopatterns through surface hydrosilation.[36] Tiny amounts of water are essential for preparing organosilane films on surfaces. If too much water is present a polymerization reaction can take place, which prevents the development of a surface film. When latex masks were fully dried in an oven, OTS nanostructures were not generated after exposure to organosilane vapors, as viewed in Figure 5.2A. After rinsing away the template latex particles, a few loose adsorbates are present on the mica surface, which affect tip adhesion. However, there are no defined periodic structures present in the AFM topograph of Figure 5.2A. The cursor profile provides further evidence that OTS structures did not form for templates which were dried in an oven.
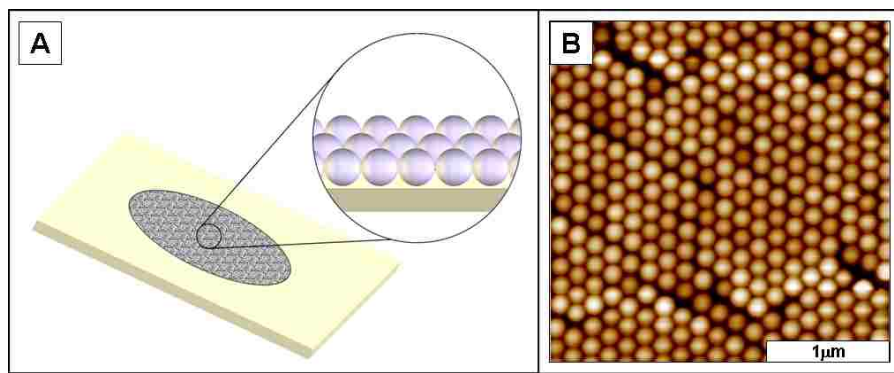
Figure 5.1 Arrangement of latex particles on surfaces. (A) Close-packed arrangement of mesoparticles; (B) topograph of 150 nm latex spheres.

For latex masks that were dried briefly (20 – 60 min) under ambient conditions, arrays of OTS nanopatterns with pore-shaped morphologies were produced as shown in Figure 5.2B. A film of OTS with circular areas of uncovered substrate is revealed, where the latex spheres were rinsed away. The thickness of the OTS layer is relatively even across the surface, uniformly

covering the areas between the cavities where latex particles were displaced. The thickness of the film measures 2.3 ± 0.3 nm, referencing the uncovered areas of the substrate as a baseline, which matches with values for an OTS monolayer (2.65 nm) as previously reported with mica substrates.[113] Measurements of the periodicity were calculated by averaging the distances between the centers of the pores for at least 200 nanostructures from several representative areas of the surface. The average periodicity of OTS pores measured 309 ± 8 nm and matches well with the expected diameter of the latex mesospheres (299 ± 6 nm).

Ring structures of OTS can be generated drying the latex masks under ambient temperatures for 12 h, as displayed in Figure 5.2C. Ring-shaped OTS nanopatterns form a hexagonal arrangement with precisely replicated geometries. For masks which have been dried for several hours, the AFM image reveals that OTS only binds in areas near the base of the latex spheres to form ring structures. The height of the rings measures 2.2 ± 0.4 nm which matches the dimension of the pore shaped OTS nanopatterns. The periodicity of the OTS rings averages 311 ± 6 nm which corresponds to the diameter of the latex spheres.

For organosilanes to covalently bind to substrates, nanoscopic amounts of water are needed to initiate surface hydrosilation. After vapor deposition of silanes and rinsing steps, AFM images in Figure 5.2 clearly display surface areas where an OTS film has formed where water was present. These results demonstrate that the amount of water on surfaces is a critical parameter for controlling the sites for hydrolysis of OTS. For latex masks which were fully dried in an oven, nanostructures of OTS did not form in the absence of water (Figure 5.2A). For latex masks that have been dried briefly (20 − 60 min), water is distributed homogeneously throughout areas of the surface to enable vapor phase assembly of OTS into the interstitial areas between latex particles (Figure 5.2B). The areas masked by the latex spheres are protected from silane

adsorption. When colloidal masks are dried under ambient conditions for longer intervals (12 h), most of the water evaporates from the surface. Only tiny residues of water persist to form a circular meniscus in areas surrounding the base of latex spheres. When the partially-dried latex masks are exposed to OTS vapor, hydrolysis occurs only where water is present at the base of the spheres to form ring-shaped nanostructures of organosilanes (Figure 5.2C).
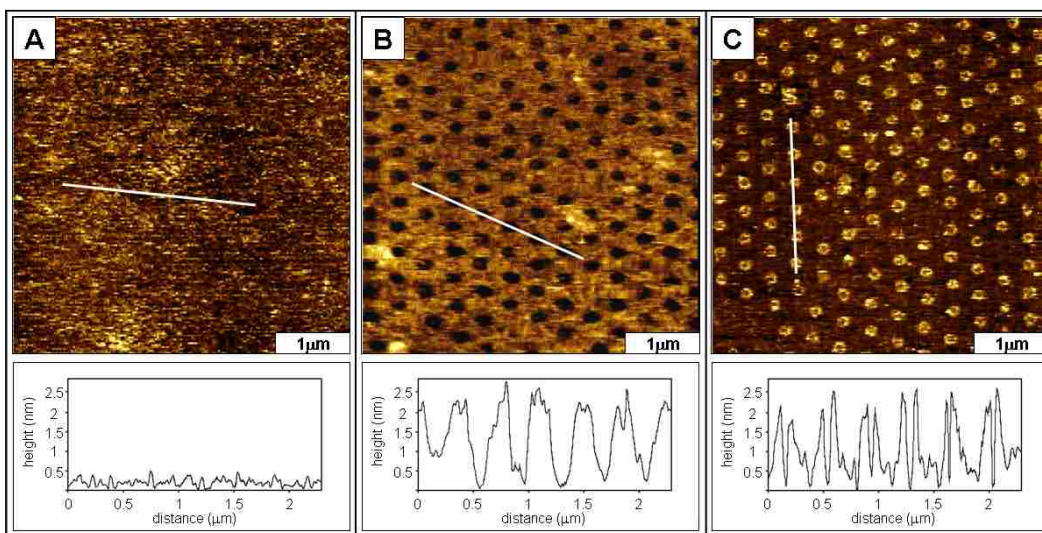
Figure 5.2 Different morphologies were produced for OTS nanopatterns with various drying conditions for 300 nm latex masks. (A) Nanopatterns of OTS were not generated when using oven-dried masks. (B) Pore-shaped nanopatterns were produced with latex masks that were dried briefly (< 60 min). (C) Ring shaped nanostructures were fabricated for latex masks dried under ambient conditions for 12 h.

5.3.2 Electroless Deposition of Iron Oxide on Nanopatterned Surfaces

To deposit metals on organosilane nanopatterns, ELD was used to selectively deposit iron oxide on areas backfilled with MPTMS, which were surrounded by OTS. The areas passivated with methyl-terminated OTS resisted the adsorption of metals, and thus the iron oxide deposited selectively on thiol-terminated nanopatterns of MPTMS. Electroless metal deposition is a convenient, rapid and low cost method to produce thin metal films on a variety of substrates. This method uses an autocatalytic reaction that involves a reducing agent and complexed metal ions as the source of the metal. When immersing substrates into an ELD solution, the reducing

agent provides the electrons to convert the metal ions into the metal films at activated sites on surfaces. In this investigation, iron (II) chloride tetrahydrate in sodium acetate buffer was the source of the metal and sodium nitrite served as a reducing agent.

Iron oxide nanostructures can be generated using ELD on nanopatterned surfaces. The topography image in Figure 5.3 displays views of a two-dimensional array of Fe_3O_4 deposits formed on MPTMS nanopatterns. The long-range order and organization of Fe_3O_4 nanostructures is apparent in the AFM views (Figures 5.3A and 5.3B) with only a few defects. Nanopatterned silicon substrates with different functional groups provide nanoscale selectivity for adsorption of iron oxide. Methyl-terminated OTS provides a hydrophobic surface which resists the adsorption of iron oxide under these conditions. Thiol-terminated MPTMS serves as an adhesive monolayer for site-selective ELD of iron oxide. The metal conforms precisely to the geometry of the back-filled areas of MPTMS. The areas surrounding each metal nanostructure are passivated with OTS. The representative cursor profile (Figure 5.3C) indicates the periodicity measured for the arrays of iron oxide nanostructures (158 ± 11 nm), which corresponds closely to the dimensions of the latex masks (151 ± 4 nm). The average size of iron oxide nanostructures is 10 ± 3 nm in height and 56 ± 10 nm in diameter. With ELD, the deposition of a few nanometers of Fe_3O_4 can be achieved rapidly, within 30 min.
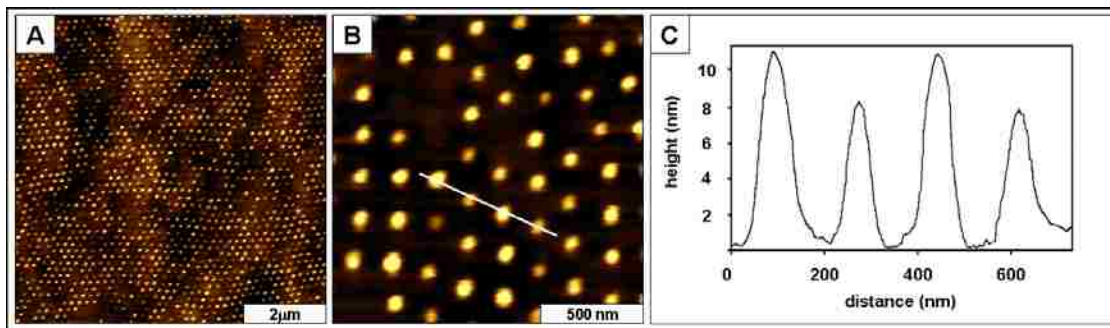
Figure 5.3 Metal nanostructures produced using electroless deposition on organosilane nanopatterns. (A) Broad view of periodic 150 nm arrays of iron oxide nanostructures; (B) zoom-in view; (C) cursor profile for panel B.

57

Iron oxide nanostructures produced using ELD on nanopatterns conform to the hexagonal arrangement of latex mesospheres. The spacing between each nanostructure is uniform and periodic. Within the 1.5×1.5 μm^2 frame of Figure 5.3B, there are 57 iron oxide nanostructures, and the larger area (8×8 μm^2) of Figure 5.3A has ~1600 iron oxide nanostructures. This yields an estimated surface density of 2.5×10^9 nanostructures per square centimeter. Thus, combining ELD with vapor deposition of silanes offers advantages of high throughput and reproducibility. The final heterostructure of iron oxide deposited on an MPTMS nanopattern formed on silicon is a metal-molecule-semiconductor junction. Such heterostructures are suitable for scanning probe microscopy (SPM) investigations of molecular conductance, towards development of nanoscale electrical contacts for molecular electronics. Future investigations are directed towards incorporating more complicated molecules with aromatic backbones within the hybrid nanostructures.

5.4 Conclusions

Selective metallization of organosilane nanopatterns can be accomplished using particle lithography and ELD. Deposition of iron oxide occurs via an autocatalytic reaction in which iron (II) ions are reduced in a solution of sodium nitrite, and deposit specifically on nanopatterned regions of MPTMS. Nanopatterned surfaces containing OTS and MPTMS provide adhesive and resistive regions for site-selective adsorption of iron oxide. The deposition of iron oxide with a few nanometers thickness occurs in less than 30 min. Results from AFM images reveal the selectivity for metal deposition on nanopatterns. The metallized nanopatterns are smaller than the latex mesospheres, however the inter-pattern spacing corresponds precisely to the periodicity of mesoparticle masks. Designed nanostructures provide a practical test platform for investigations of surface properties, since well-defined arrays enable precise reproducible dimensions for

multiple successive SPM measurements. The particle templates used for preparing test platforms can be scaled to very small dimensions. Metal contacts formed on organosilane nanopatterns produced by particle lithography combined with vapor deposition may be suitable for SPM investigations of molecular conductance, towards development of nanoscale electrical contacts and heterojunctions.

CHAPTER 6. ENGINEERING THE SPATIAL SELECTIVITY OF SURFACES AT THE NANOSCALE USING PARTICLE LITHOGRAPHY TO PATTERN ORGANOSILANES

6.1 Introduction

Engineering the chemistry of surfaces at the nanoscale poses a significant challenge for nanotechnology.[1-3, 87, 203] Many strategies for nanoscale lithography have emerged, which hold promise for development of practical devices such as high density storage devices[204, 205], memory[98, 206], optoelectronic components[207-209] and highly sensitive detectors.[209-211] In choosing nanolithography approaches for manufacturing devices, one of the most critical issues to be addressed is high throughput. Nanoscale technologies will undoubtedly require the ability to prepare millions of reproducible structures with high fidelity, at low expense. The great promise of nanotechnology depends on the ability to organize materials at the nanoscale to generate designed assemblies that exhibit desirable properties. Molecular architectures with well-defined functionalities and composition will advance applications for molecular electronics[97, 98, 212, 213] or biosensing applications.[18, 96, 214]

Particle lithography, which has also been referred to as nanosphere lithography or colloidal lithography, uses the close-packed arrangement of spherical particles to produce ordered arrays of regular nanostructures.[22, 23] Monodisperse spheres self-assemble on flat surfaces into periodic structures with designed dimensions and interparticle spacing, which can then be used as structural templates or masks to guide the deposition of metals,[24, 48] polymers,[27, 58] catalysts,[55] nanoparticles,[215, 216] self-assembled monolayers (SAMs)[28, 36, 135, 136] and proteins.[29-32] We recently developed a method to pattern organosilanes on conventional surfaces such as glass, silicon wafers, mica and gold using particle lithography.[36, 37] Organosilane SAMs attach to the unmasked interstitial areas of the surface between masks of mesospheres through vapor deposition.

Well-defined self-assembled monolayers of organosilanes formed on oxide surfaces were first reported by Sagiv in 1980.[33] Since then, organosilanes have been have been widely applied to engineer surface properties and provide a versatile molecular platform for surface patterning and nanofabrication.[34, 35, 103, 217, 218] The interfacial functionalities of organosilane SAMs provide a way to tailor the chemistry of surfaces to attach various nanomaterials such as nanoparticles[146, 149] and biomolecules.[29, 147, 148] The robust and covalent natures of organosilanes enable further steps of chemical modification to regulate surface chemistry at the nanoscale.[107, 150-152]

A range of lithographic approaches have been developed to pattern organosilane monolayers. Photolithography with silane SAMs is accomplished by UV irradiation through photomasks.[15] Organosilane monolayers in exposed regions can be selectively removed by a photocleavage mechanism or can alter the functionality of surface head groups by UV-activated photochemistry.[126] The resolution of patterns produced by photolithography is limited by the diffraction of light sources. Electron beam lithography can overcome the diffraction limit to generate smaller patterns with dimensions less than 100 nm.[127, 128] However, e-beam lithography requires considerable training and expensive instrumentation. Soft lithography, such as microcontact printing with polydimethylsilane (PDMS) stamps, has been applied successfully for patterning silane monolayers.[16, 129] The dimensions of organosilane patterns are limited to the size of the PDMS stamps, most typically at the micrometer scale. Scanning probe lithography (SPL) approaches such as Dip-Pen nanolithography,[17, 130] nanoshaving,[131, 132] bias-induced lithography,[21] and constructive nanolithography[20, 43, 133] have also been applied to write nanopatterns of organosilane SAMs. Methods of SPL provide exquisite nanoscale resolution; however the fabrication steps are time-consuming due to slow serial writing processes, which are not easily scalable for the high throughput requirements of device manufacture.

61

Approaches based on steps of particle lithography, vapor deposition of organosilanes and selective deposition of nanoparticles will be described in this report. The size, shape and spacing of nanopatterns can be precisely controlled by the diameters of mesoparticle masks used for particle lithography. The surface selectivity can be engineered to define nanoscale sites for surface passivation or reactivity using well-defined functionalities of silanes. Engineered nanopatterns of adhesive and resistive silane SAMs offer exquisite surface selectivity, which can be used as a foundation for site-directed adsorption of nanoparticles. The nanoparticles attach precisely to well-defined areas to form reproducible geometries and scalable surface coverage.

6.2 Materials and Methods

6.2.1 Atomic Force Microscopy

Samples were characterized using either contact mode or acoustic AC-mode AFM with a model 5500 scanning probe microscope (Agilent Technologies, Chandler, AZ). Rectangular silicon nitride cantilevers with force constants ranging from 21 to 98 N/m and an average resonance frequency of 165 kHz were used for AAC-mode (tapping) characterizations (Nanosensors Lady's Island, SC). Contact mode AFM images were acquired using V-shaped cantilevers with oxide-sharpened silicon nitride probes, which had an average force constant of 0.5 N/m (Veeco Probes, Santa Barbara, CA). Images were processed using Gwyddion open source software, which is freely available on the internet and supported by the Czech Metrology Institute.[138] The analysis data presented was estimated using the commercially available SPM analysis software, SPIP, with multiple images.

6.2.2 Preparation of Organosilane Nanopatterns

Particle lithography with vapor deposition was used to generate organosilane nanopatterns on surfaces, as previously reported.[36] Polished silicon wafers, Si(111) doped with

boron (Virginia Semiconductor Inc., Fredericksburg, VA) and glass cover slides (Fisher Scientific, Pittsburgh, PA) were used as substrates. Substrates were cleaned by immersion in piranha solution for 1 h, which is a mixture of sulfuric acid and hydrogen peroxide at a (v/v) ratio of 3:1. Piranha solution is highly corrosive and should be handled carefully. Substrates were then rinsed copiously with deionized water and dried in air. Size-sorted polystyrene latex spheres (Thermo Scientific, Waltham, MA) were washed by centrifugation to remove contaminants such as charge stabilizer or surfactants. The latex pellet formed by centrifuging was resuspended in deionized water, and a 20 µL drop of the latex solution (2 % w/v) was deposited on a clean substrate. The samples were dried in ambient conditions (25 °C, relative humidity ~60 %) to produce evaporative masks for particle lithography. As water evaporates during drying, capillary forces pull the mesospheres together to form organized crystalline layers on flat surfaces. During the drying step, most of the water evaporates and only tiny residues persist to form a meniscus surrounding the base of the spheres. Next, the substrates with latex masks were placed into a sealed reaction vessel containing 300 µL of the selected organosilane. Organosilanes such as OTS, AAPTMS, MPTMS and PEG-silane were purchased from Gelest (Morrisville, PA), and used without further purification. To generate an organosilane vapor, the reaction vessel was placed in an oven and heated at 70-80 °C for at least 6 h under ambient pressure. During vapor deposition, organosilanes adsorbed to uncovered interstitial areas of the surface between latex spheres which contain water residues. The latex masks were removed completely by sonication and rinsing with ethanol and deionized water.

6.2.3 Deposition of a Second Organosilane by Solution Immersion

Areas of the surface that were not covered with nanopatterns could be backfilled with a second organosilane by solution immersion. Substrates with silane nanopatterns were immersed

for 4 h in a toluene solution containing 1 mM of the chosen organosilane. Afterwards, the samples were cleaned by sonication in toluene and ethanol for 15 min.

6.2.4 Attachment of Gold Nanoparticles to Organosilane Nanopatterns

Gold nanoparticles were synthesized according to a previous procedure.[219, 220] Surfaces of silicon or glass containing binary nanopatterns of OTS and MPTMS were immersed in a solution of gold nanoparticles for 8 h. Afterwards, the samples were briefly sonicated in ethanol for 2 min and then rinsed with ethanol and deionized water. Ultraviolet-visible spectra for arrays of gold nanoparticle were recorded with a Varian Cary 50 UV-Vis spectrophotometer (PaloAlto, CA).

6.3 Results and Discussion

6.3.1 Successive Steps for Defining Surface Chemistry via Particle Lithography

Solutions of monodisperse mesoparticles spontaneously self-assemble to form close-packed layers when dried on flat surfaces, as viewed in the AFM topography image of a film of 200 nm latex spheres (Figure 6.1A). The latex film exhibits hexagonal arrays of periodic, well-ordered domains with relatively few defects. The AFM topograph displays only the uppermost layer of the latex spheres, whereas the bottom layer in contact with the substrate actually provides the mask for chemical vapor deposition. Often the bottom layer will have fewer defects and better packing than the top surface, because rows of particles are filled in from upper layers of spheres.[137, 143] After preparing masks of monodisperse mesoparticles, the surfaces were exposed to heated organosilane vapors in the next step. The time intervals for vapor exposure ranged from 6-24 hours, depending on the nature of the organosilane molecules that were chosen. The mesospheres are removed in the next step by simple immersion or sonication in deionized water or solvents. Two properties of latex facilitate complete removal of the masks from the

surface: the buoyancy of the spheres as well as the tendency for the spheres to swell when liquid is added. Nanopatterns of organosilanes such as octadecyltrichlorosilane (OTS) remain securely attached to the surface, as shown by a representative AFM topograph in Figure 6.1B. Ring-shaped nanopatterns of OTS were produced on Si(111) via vapor deposition using a mask of 150 nm latex. During vapor deposition, OTS molecules adsorb through hydrosilation onto uncovered interstitial areas of the surface between latex spheres. The area of contact between the substrate and the base of the spheres is effectively masked to produce patterns with circular geometries. The latex masks are selectively and completely removed with the rinsing step, whereas the organosilanes remain covalently bound to the substrates.
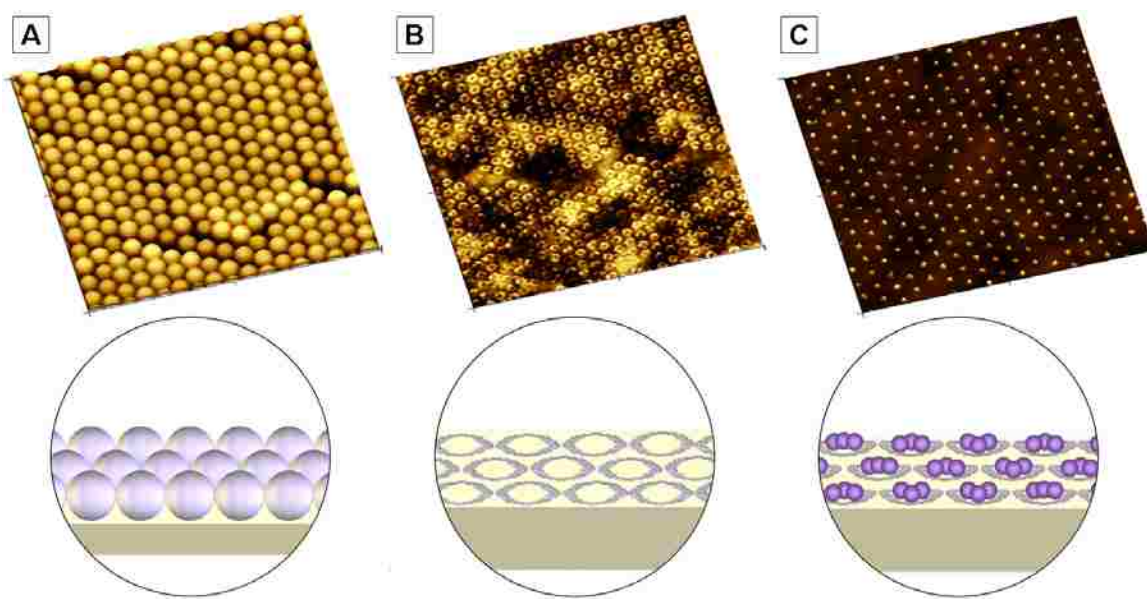
Figure 6.1 Snapshots of the key steps of particle lithography. (A) Evaporative mask of 200 nm latex, 4×4 μm^2 AFM contact-mode topograph; (B) Ring patterns of OTS formed on Si(111) viewed after latex removal (4×4 μm^2 topograph); (C) Arrays of gold nanoparticles attached to thiol-terminated patterns of organosilanes (4×4 μm^2).

After preparing organosilane nanostructures, additional steps can be accomplished to backfill uncovered areas of the surface with new molecules or nanomaterials. A second organosilane with different terminal groups can be used to backfill the bare areas of the

65

substrates by immersion. Another successive chemical step can be accomplished by immersing the binary patterned surface into solutions of other molecules or nanoparticles. An example is shown for gold nanoparticles deposited on nanopatterns of sulfur-terminated 3-mercaptopropyltrimethoxysilane (MPTMS) in Figure 6.1C. Because of the strong affinity between thiols and gold, gold nanoparticles adsorb selectively on the regions containing MPTMS. Arrays of gold nanoparticle aggregates were generated on surfaces of Si(111) nanopatterned with OTS and MPTMS. The spacing and periodicity of the deposits of gold nanoparticles conform to the areas with MPTMS nanopatterns, and the areas of OTS provide an effective resist to prevent nonspecific binding in the surrounding areas.

6.3.2 Change in Nanopattern Morphology with Different Drying Conditions of Masks

Molecules of OTS adsorb onto unmasked interstitial areas of the surface surrounding latex mesospheres where water residues are located.[36] The amount of water present on the masked surface is affected by the drying intervals as well as the size of the mesospheres. Of course, a larger area of contact is observed for larger particles. The spherical particles appear to trap tiny amounts of water in a local meniscus surrounding the base of the spheres, and this area increases progressively for larger diameters. For smaller particles, more of the surface areas are masked by latex, to produce less uncovered space between spheres. The area of contact directly underneath the spheres is effectively masked to produce patterns with circular geometries. Figure 6.2 demonstrates how the intervals for drying latex masks affect the morphology of organosilane nanopatterns on mica(0001). For latex masks that have been dried briefly (25 min), water is distributed homogeneously throughout areas of the surface to enable vapor phase assembly of OTS into the entire interstitial areas between latex particles (Figure 6.2A). The areas masked by the latex spheres are protected from silane adsorption to produce a uniform OTS film

66

with uncovered pore structures (Figure 6.2B and 6.2C). The thickness of the film measures 2.2 ± 0.4 nm, referencing the uncovered areas of the substrate as a baseline (Figure 6.2D). When mesoparticle masks are dried under ambient conditions for longer intervals (12 h), only tiny residues of water persist to form a circular meniscus in areas surrounding the base of latex spheres (Figure 6.2E). When the partially-dried latex masks are exposed to OTS vapor, hydrolysis occurs only where water is present at the base of the spheres to form ring-shaped nanostructures of organosilanes as displayed in Figure 6.2F and 6.2G. The height of the rings measures 2.3 ± 0.3 nm which matches the dimensions of the pore patterns within the OTS film (Figure 6.2H). For latex masks which were fully dried in an oven, no water is available to initiate hydrosilation (Figure 6.2I). After rinsing away the template latex particles of the oven-dried masks, no nanostructures are visible on the mica surface. There are no defined OTS nanostructures present in the AFM topograph of Figures 6.2J and 6.2K. The cursor profile in Figure 6.2L further evidences that OTS structures did not form for templates which were dried in an oven.

Nanoscopic amounts of water are essential to initiate surface hydrolysis for organosilanes to bind to substrates. The distribution of water can be spatially controlled on surfaces using latex or colloidal silica mesoparticles as masks to direct the placement of water residues. The amount of water on surfaces is a critical parameter for controlling the sites for hydrolysis of organosilanes such as OTS, which can be regulated with the drying intervals. When latex masks are dried briefly in ambient conditions, water is distributed homogeneously throughout areas of the surface to form an ultrathin film between mesoparticles. The organosilane nanopatterns bind to the surface according to the arrangement and locations of water residues, essentially providing a fingerprint of the local distribution of water for AFM images of the nanopatterns. For

mesoparticle masks that are dried under ambient conditions for longer intervals, water accumulates and form an exquisitely regular circular meniscus at the base of latex spheres. As OTS vapor is introduced, hydrosilation only occurs where water is present to produce ring-shaped nanopatterns. Latex masks serve to define the locations of nanoscopic residues of water on gold surfaces which in turns spatially directs the sites for hydrosilation. The vapor deposition strategy for nanopatterning has been used successfully for patterning surfaces of mica(0001), Si(111), glass and indium-tin oxide surfaces. Even the relatively hydrophobic surfaces of Au(111) can be successfully applied as substrates with particle lithography.[37]
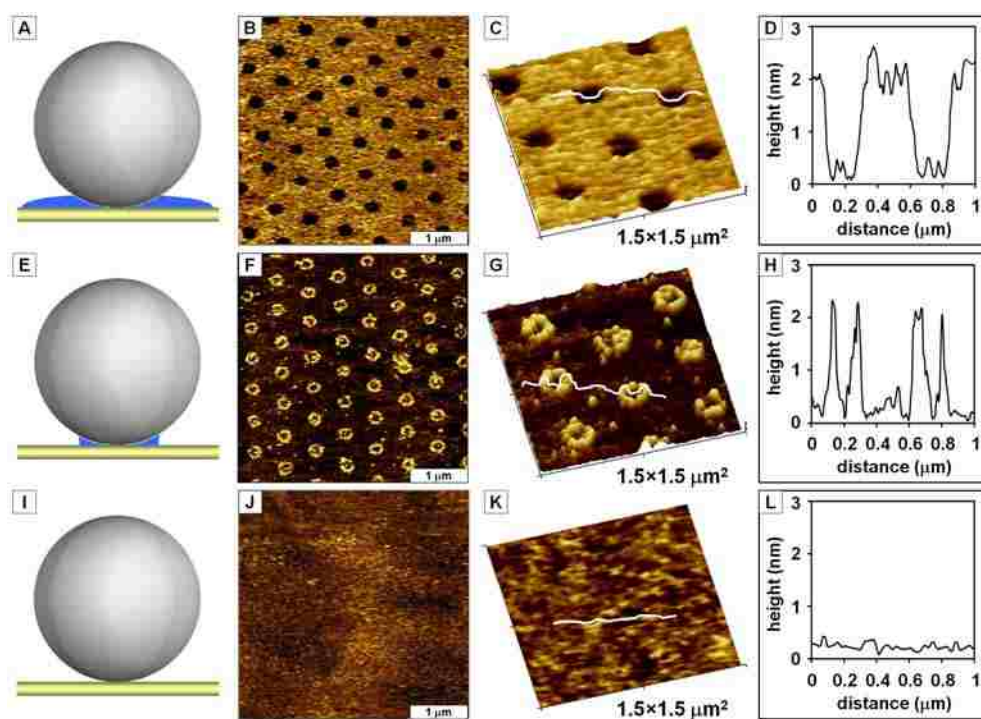
Figure 6.2 Sites of water residues determine the surface morphology of organosilane nanostructures. (A) Interstitial areas between colloidal spheres are covered with water when mask is dried briefly; (B) topography image of a porous OTS film on mica(0001) formed by briefly drying 500 nm latex masks; (C) zoom-in view of B; (D) cursor profile for line in C; (E) water meniscus forms at the base of spheres when mask is dried for several hours under ambient conditions; (F) topograph of an array of OTS ring patterns on mica(0001) generated by partially drying latex masks (500 nm); [G] zoom-in view of F; (H) height profile for cursor line in G; (I) colloidal masks which are dried completely results in the absence of water on the surface; (J) topographic view revealing that no nanopatterns of OTS are generated on the surface when evaporative masks are dried completely; (K) zoom-in image of J; (L) cursor profile for line in K.

6.3.3 Nanoscale Control of Periodicity and Surface Coverage

Changes of certain experimental parameters provide a means to systematically define the periodicity and surface coverage of nanostructures produced by particle lithography. For example, changing the diameter of the mesoparticle masks will alter the interpattern spacing as well as the size and surface densities of silane nanostructures. An example is presented for arrays of 2-[methoxy(polyethylene-oxy)propyl] trimethoxysilane (PEG silane) nanopatterns produced with latex masks of various diameters, shown by a series of AFM topographs in Figure 6.3. The surface density increases as the diameter of the latex spheres used as evaporative masks is changed from 500 nm to 300, 200, 150 and 100 nm for Figures 6.3A, 6.3B, 6.3C, 6.3D and 6.3E, respectively. For example, in the successive zoom-in views of Figure 6.3, the third column shows a 1 x 1 μm^2 view. The number of particles progresses from 3 nanopatterns per μm^2 in Figure 6.3A to 9, 19, 32 and 52 rings per μm^2 for Figures 6.3B-6.3E, in succession. The periodicity of the ring patterns of PEG silane can be measured with cursor line profiles, and were found to closely match the expected diameters of the latex masks. The long-range order and organization of PEG-silane rings is apparent in the successive zoom-in views, with only a few defects produced by missing particles. The ring-shaped geometries of PEG-silane nanopatterns are remarkably consistent. Regardless of the latex diameters, the heights of the PEG ring patterns are quite uniform at the nanoscale, ranging from 6.4 to 7.1 nm. The unevenness of the height is likely produced by beading of water on the surface areas during the vapor deposition step, causing slightly irregular wetting of the surface. The self-assembly process of various organosilanes have been reported to proceed via an island growth mechanism.[35, 113, 221, 222] The adsorption of preorganized aggregates of organosilane molecules first occurs on surfaces where

the nanoscopic residues of water are confined with latex masks. Slower adsorption processes continue to form a more dense layer until hydrosilation is completed.
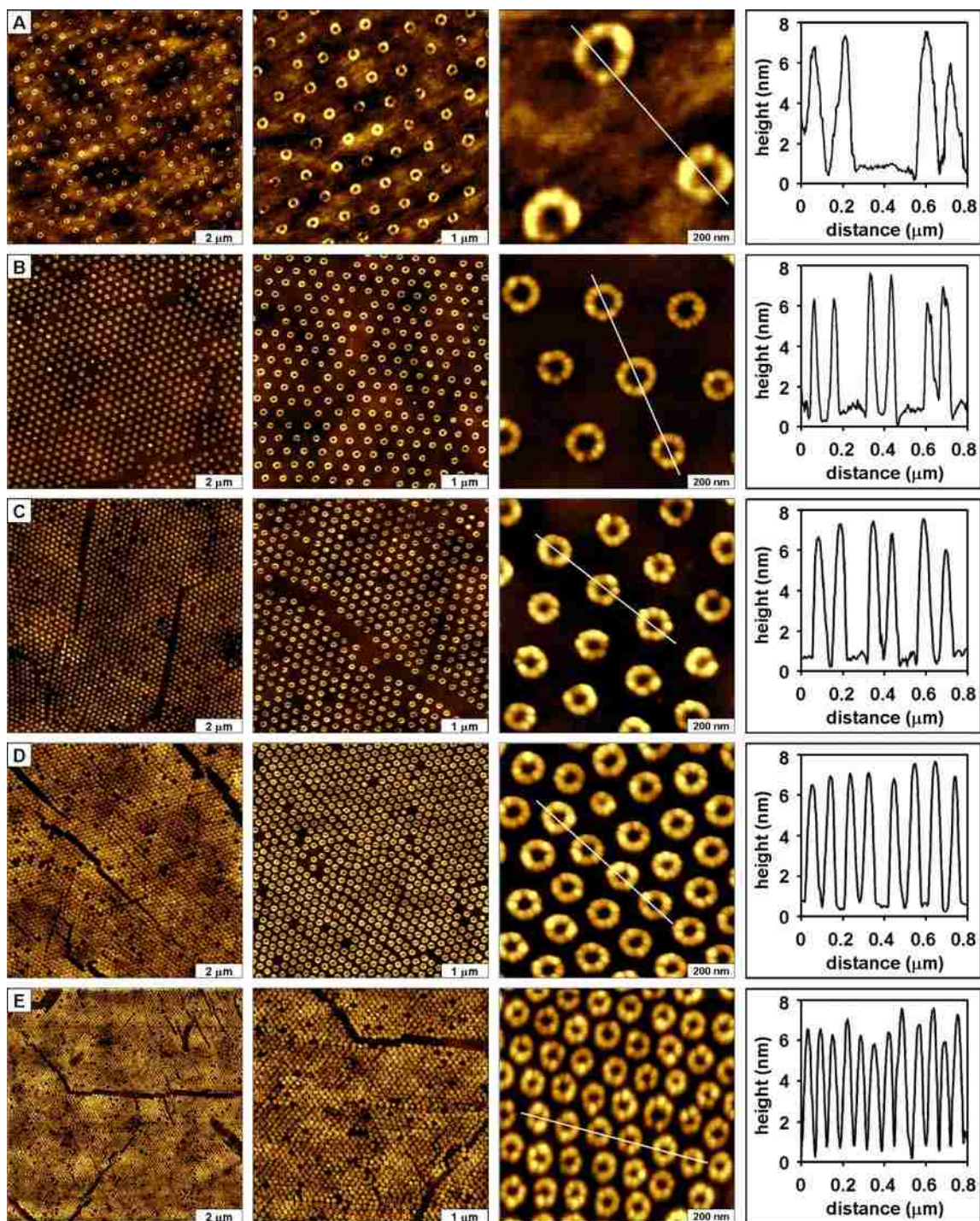
Figure 6.3 Changes in surface coverage and periodicity of organosilane nanopatterns using different mesosphere diameters. Tapping mode views of PEG silane nanopatterns on Si(111) fabricated using (A) 500, (B) 300, (C) 200, (D) 150, and (E) 100 nm diameter latex.

70

Estimates of the surface coverage as well as the surface areas of the rings and pores of the PEG-silane nanopatterns are plotted in Figure 6.4. The charts clearly demonstrate that the surface area of the uncovered substrates as well as the areas covered by the ring patterns change accordingly with mesoparticle diameters. The estimates were made using AFM analysis software with multiple images. The surface coverage for PEG-silane nanopatterns changes from 32 to 74 percent as the diameters of latex masks decrease from 500 nm to 100 nm (Figure 6.4A). With smaller latex mesoparticles, close-packed evaporative masks offer more sites for surface hydrosilation to generate a larger number of nanopatterns, thus resulting in higher surface coverage. The surface areas covered with PEG-silane within the rings changes with latex diameters (Figure 6.4B), ranging from 3000 nm^2 (100 nm sphere diameter) to 14000 nm^2 (500 nm diameter). The variation in the surface area of the rings results from changes in the size of water meniscus formed at the base of spheres. The areas of the rings are defined by the areas wetted by nanoscopic amounts of water. Larger mesoparticles enable more water to become trapped as residues at the base of the spheres, forming a larger water meniscus for hydrosilation.

The area of the patterns is also strongly affected by the drying conditions of latex masks. The surface areas of uncovered pore areas inside the PEG rings was observed to increase with larger latex diameters (Figure 6.4C). The pore sizes change from 1900 nm^2 to 14000 nm^2 as the latex diameter is increased from 100 to 500 nm. Measurements of the surface areas of uncovered pore sites within the PEG rings provide a way to assess the actual region of contact between latex spheres and the surface. The hydrodynamic radius of latex particles change upon wetting and the swelling of latex can cause the diameters of spheres to change at the nanoscale. As latex solutions are deposited and dried, the deformability of polystyrene latex results in changes for the area of contact between the latex spheres and the surface.

71
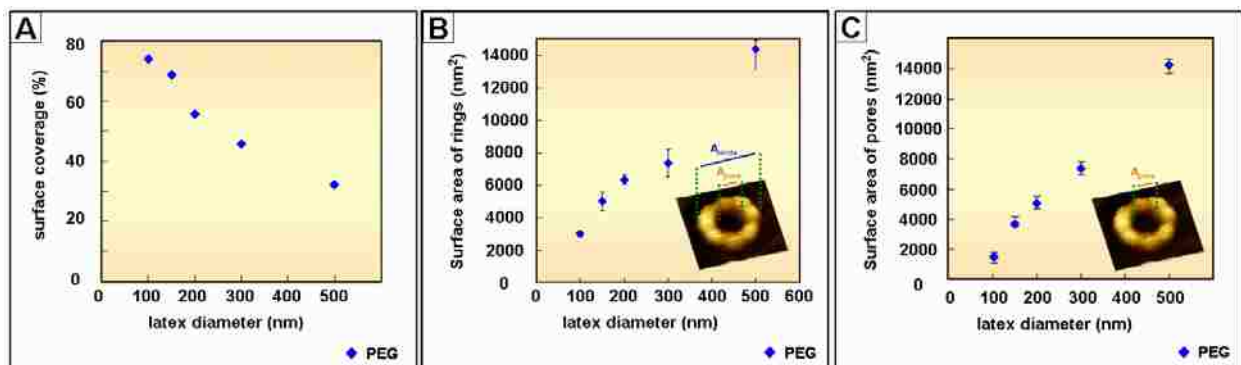
Figure 6.4 Data analysis of the effect of latex diameter on (A) surface coverage of PEG silane nanostructures, (B) surface area of PEG silane ring patterns, and (C) surface area of uncovered pores.

6.3.4 Applicability of Particle Lithography for Different Terminal Moieties

Particle lithography was also applied successfully for patterning amine-terminated silanes. Nanopatterns of N-(6-aminohexyl) aminopropyltrimethoxysilane (AAPTMS) are shown in Figure 5 for various diameters of latex masks. Successive zoom-in views reveal that AAPTMS nanopatterns exhibit exquisitely uniform and regular ring morphologies, regardless of the different latex diameters (Figure 6.5A, 6.5B, and 6.5C). The heights of the PEG ring patterns are quite consistent, ranging from 3.2 to 3.7 nm. The periodicity corresponds closely to the dimensions of latex masks. The surface coverage and density of AAPTMS nanopatterns are changeable with the diameters of mesoparticle masks used for particle lithography. The zoom-in images display a very slight unevenness of the height on the order of ±0.2 nm, which results from the subtle differences in surface wettability during the vapor deposition step.

The changes in surface density were evaluated and compared as a function of latex diameter (Figure 6.6A) for AAPTMS and PEG silane nanostructures. Since the number of nanostructures is determined by the packing density of the latex spheres of the evaporative masks, the surface densities are nearly identical. The numbers of PEG rings range from 3.9×10^8 nanostructures per cm^2 for 500 nm spheres, to as high as 7.6×10^9 for 100 nm latex.

72
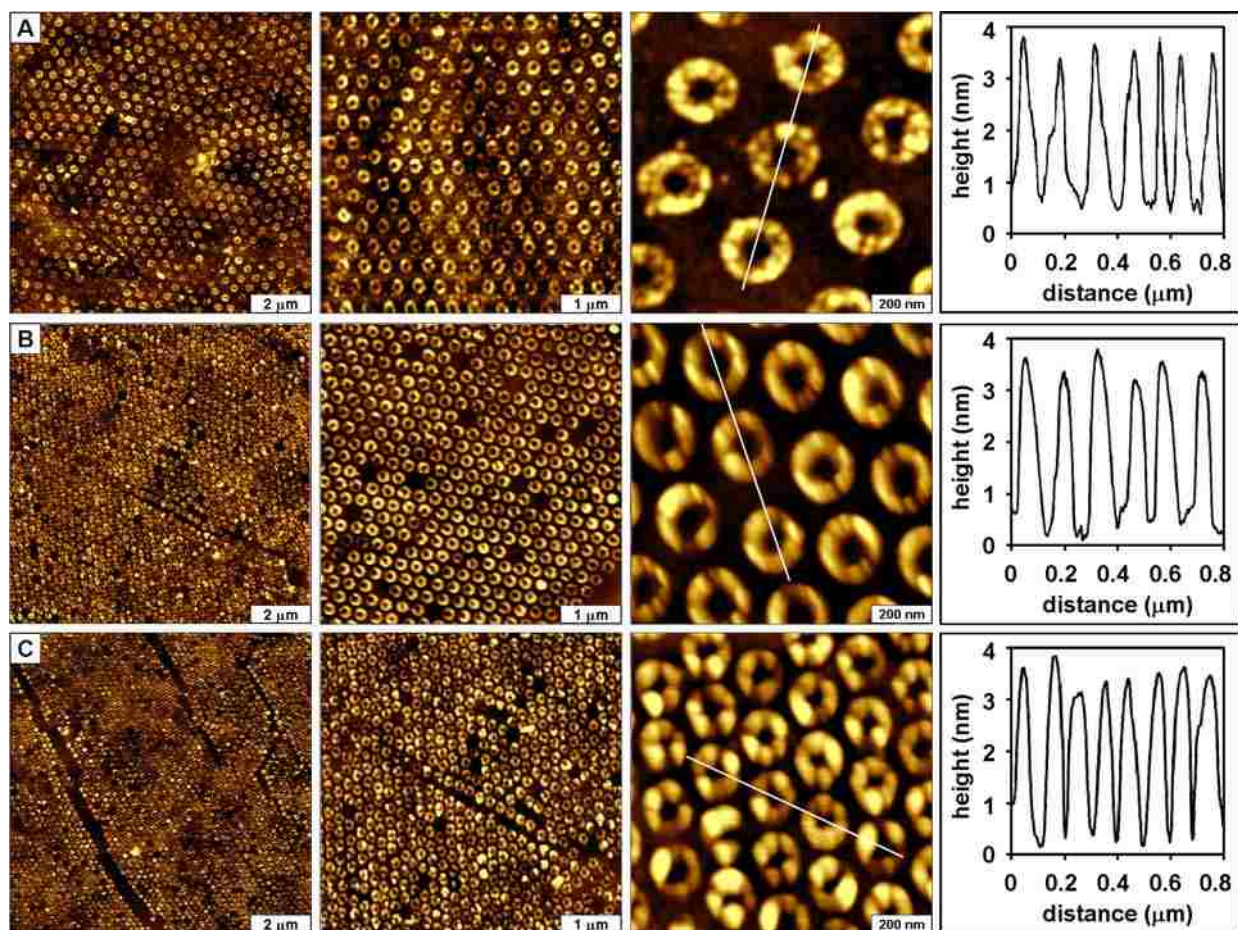
Figure 6.5 Periodic nanostructures of AAPTMS on Si(111) produced using particle lithography combined with heated vapor deposition. Tapping-mode AFM topographs of AAPTMS nanopatterns produced with latex masks having periodicities of (A) 300 nm, (B) 200 nm, and (C) 150 nm.

The steps of particle lithography combined with chemical vapor deposition are shown to generate high surface densities with excellent reproducibility and well-defined geometries. Once the experimental conditions are optimized, dozens of samples prepared with the selected conditions exhibit identical nanoscale morphologies. Several samples were prepared to acquire data for the surface coverage and density, and the areas shown in Figure 6.3 and Figure 6.5 are representative of multiple areas and views throughout the surface.

Interestingly, AFM images display distinct differences in surface area for the rings of AAPTMS (Figure 6.5) compared to PEG silane nanopatterns (Figure 6.3). The self-assembly

process and reactivity of organosilanes influence the resulting structures formed with silanes. The longer polymer chains of PEG-silane molecules aggregate and interdigitate to form relatively larger clusters and proceed with a slower adsorption process on surfaces until hydrosilation is complete. The shorter chains of the amine-terminated silane, AAPTMS, can self-catalyze the hydrolysis leading more aggressively to forming a monolayer compared to PEG-silane.[223-225] Due to interactions of head and tail groups between amine and silanol moieties, AAPTMS forms multilayers on surfaces, resulting in more disordered structures.[112, 226] Zoom-in AFM views of AAPTMS nanopatterns reveals that the ring shaped structures are composed of smaller clusters. Comparison of the surface coverage of AAPTMS and PEG-silane nanopatterns is presented in Figure 6.6B. A slight difference in surface coverage is observed for AAPTMS versus PEG-silane. The observed differences may attributable in part to AFM imaging artifacts. The widths of AFM probes can differ greatly at the nanoscale, and contribute to broadening of lateral dimensions of very small surface features. However, it is more likely that the differences in overall surface area of the rings arise from natural differences in self-assembly and physical dimensions of AAPTMS versus PEG silanes. The surface coverage of nanopatterned surfaces with AAPTMS corresponds with the size of the latex masks: 47 %, 54 % and 65 % for 300 nm, 200 nm and 150 nm, respectively.
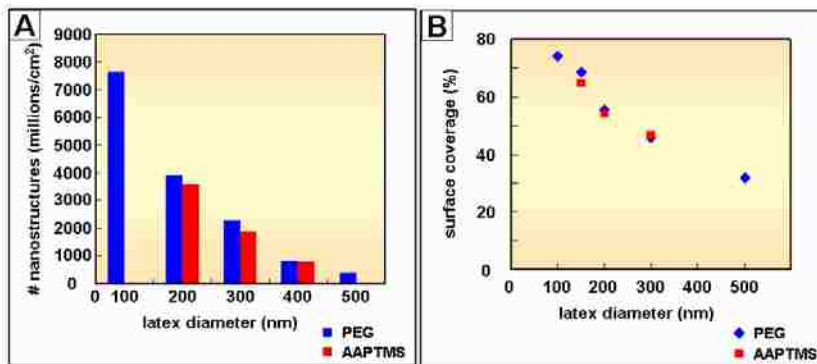
Figure 6.6 Comparison of (A) the surface densities and (B) the percent surface coverage between PEG and AAPTMS nanostructures produced with various latex diameters.

An example of the high throughput capabilities of particle lithography for fabricating organosilane nanopatterns is presented in Figure 6.7. The long-range order and organization of PEG-silane nanopatterns produced with 150 nm latex mesoparticles are apparent in the tapping mode AFM topograph, exhibiting relatively few defects over the 20×20 μm^2 scan area (Figure 6.7A). For a specific fabrication condition, the surface morphologies were highly consistent and reproducible. The simultaneously acquired phase image in Figure 6.7B reveals that the PEG rings do not touch neighboring patterns. Phase images can sensitively distinguish differences in surface chemistry, elastic response as well as edge effects.[227-230] The surfaces of PEG-silane rings exhibit a fairly uniform composition with a brighter contrast relative to the uncovered areas of silicon between the nanopatterns. The fast Fourier Transform (FFT) analysis for the AFM image of PEG rings is shown in Figure 6.7C. The FFT image clearly evidences the long range order and periodic hexagonal arrangement for arrays of PEG-silane rings.
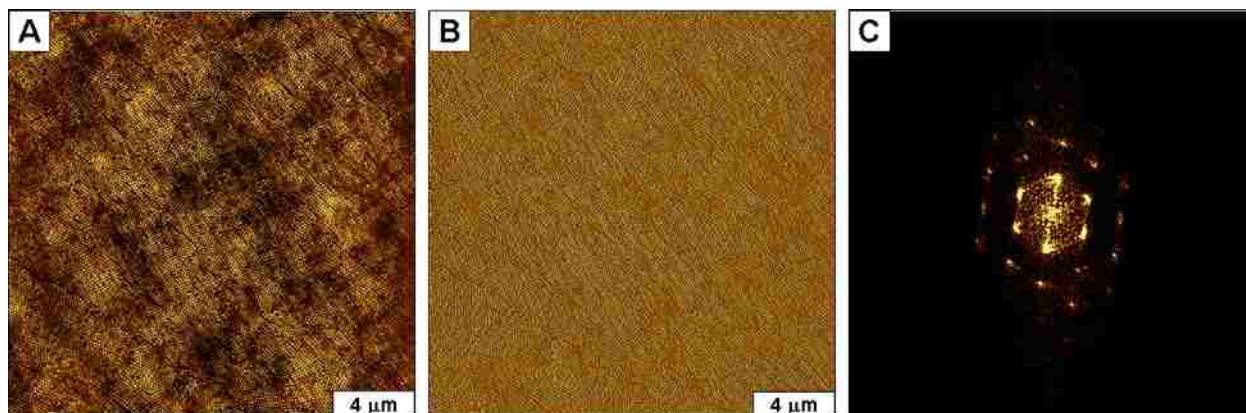
Figure 6.7 Wide area view of PEG-silane nanopatterns on silicon demonstrates the high throughput capabilities of particle lithography. (A) Topograph and (B) simultaneously acquired phase image acquired in ambient conditions with tapping mode AFM. (C)] The FFT analysis for the AFM topography image in A.

6.3.5 Spatial Selectivity for Generating Arrays of Gold Nanoparticles

Organosilane nanostructures can be used to direct the placement of metal nanoparticles on surfaces. An example is presented in Figure 6.8 for the steps of patterning a resist silane of

OTS, backfilling uncovered areas via an immersion step with a thiol-terminated organosilane, and the attachment of gold nanoparticles at defined sites using selected chemistries. In the first step, methyl-terminated patterns of OTS were generated either on silicon or glass substrates using the previously described approach for vapor deposition through mesoparticles masks (Figure 6.8A). Arrays of OTS nanopatterns with pores of uncovered areas of substrate were produced as shown in Figure 6.8B (topograph) and 6.8C (lateral force image). Referencing the uncovered areas of the substrate as a baseline, the thickness of the OTS film is fairly even throughout the surface, exhibiting uniform coverage between pores. The dark areas of the lateral force or friction image pinpoint the locations where latex particles were displaced. The differences in surface chemistry between the OTS film and the uncovered areas of the silicon substrate are apparent in Figure 6.8C. The bright color of the OTS areas is quite uniform in contrast, indicating a homogeneous chemistry at the interface. Within this 4×4 μm^2 frame there are 1495 nanopores providing 36 % of the surface area for additional adsorption sites.

The uncovered areas of the silicon surface enable further chemical steps to deposit a second organosilane via solution immersion. A short chain silane with thiol head groups was deposited in the pore areas by 4 h immersion in a solution of 1 mM MPTMS in toluene (Figure 9D). The overall surface design therefore contains circular areas (ca. 68 nm diameter) presenting thiol groups surrounded by passivated areas with methyl-terminated OTS. The changes in surface topography after the MPTMS immersion step are shown in Figures 9E and 9F. At this magnification, the shapes of the pores can no longer be clearly distinguished in the topography frames. The height differences between OTS and MPTMS are small in comparison to the roughness of the surface of polished silicon. The RMS roughness measured 1.6 nm for the area shown. However, the differences in surface chemistry can be clearly distinguished in the

corresponding lateral force image of Figure 9F. The differences in adhesion between the tip and

sample provide a sensitive map of the surface chemistry of the headgroups of OTS versus

MPTMS. The brightest color corresponds to the areas with methyl groups (OTS) whereas the

thiol groups (MPTMS) inside the pores are darker in contrast. A tiny black dot at the center of

the pores indicates that no MPTMS was deposited at the very center spot where the latex spheres

made contact with the substrate. This suggests that saturation coverage was not completely

achieved for the pore areas.
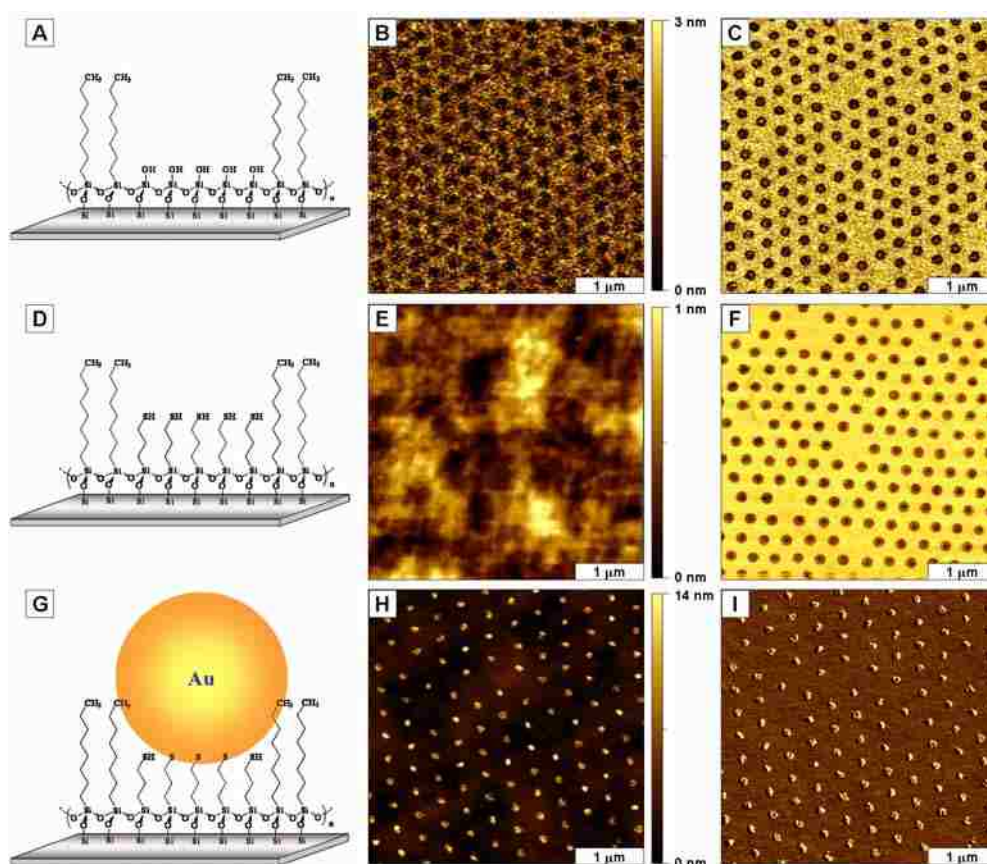
Figure 6.8 Sequence of the chemical steps for selective attachment of gold nanoparticles onto
nanopatterns of organosilanes. (A) Nanopatterning OTS using particle lithography; (B)
topography of an OTS film with pore-shaped structures produced with 300 nm latex particles; (C)
corresponding frication image for B; (D) deposition of MPTMS onto uncovered surfaces inside
OTS nanopatterns; (E) topography of nanopatterned surfaces with mixed silanes of OTS and
MPTMS; (F) friction image for E; (G) gold nanoparticles selectively adsorbed onto reactive
domains of MPTMS; (H) topography of arrays of gold nanoparticles produced using selective
adsorption; (I) simultaneously acquired friction image for H.

77

The MPTMS nanopatterns can be used for selective deposition of gold nanoparticles via S-Au chemisorption (Figure 6.8G). The thiol-terminated MPTMS patterns provide sites to selectively confine and anchor gold nanoparticles to the surface. The methyl-terminated films of OTS provide a highly effective resist to prevent binding at boundary areas surrounding the circular areas of MPTMS. Due to the strong affinity between thiols and gold, [231-233] the gold nanoparticles adsorb selectively and uniformly at the regions with MPTMS, as demonstrated in the AFM images of Figures 6.8H and 6.8I. Within the 4×4 μm^2 topograph of Figure 6.8H, there are 1324 aggregate nanostructures comprised of 3-5 gold nanoparticles within the clusters. The corresponding lateral force image exhibits interesting changes for gold nanoparticles attached to MPTMS, the edges of individual nanoparticles can be resolved, providing a means to outline the shapes of individual nanoparticles (Figure 6.8I).

Successive zoom-in views of an array of gold nanoparticle clusters that were selectively adsorbed on a surface template of MPTMS nanopatterns surrounded by OTS are presented in Figure 6.9, for a sample prepared from masks of 300 nm latex mesospheres. A representative 10 $\times$ 10 μm^2 topograph reveals the overall organization of the gold nanoparticles on the silicon substrate (Figure 6.9A). The interstitial areas that are covered with methyl-terminated OTS provided a highly uniform and selective resist for preventing nanoparticle adsorption, whereas the pore regions filled with MPTMS define surface attachment sites presenting thiol groups to direct the binding of nanoparticles. A further close-up view in Figure 6.9B discloses the symmetry and arrangement of 188 gold nanoparticle ensembles, which cover 31 % of the total surface. The clusters are composed of aggregates of 3-5 gold nanoparticles, approximately 13 % of the clusters containing 2 nanoparticles. Within the 1×1 μm^2 area of Figure 10C, nine clusters of gold nanoparticles are apparent the 3-D zoom-in view. These images are representative of

areas throughout the sample, and demonstrate the exquisite spatial selectivity of organosilane nanopatterns. An average periodicity of 310 ± 14 nm was measured for the arrays of gold nanoparticles (Figure 6.9D), which corresponds closely to the dimensions of the latex masks (301 ± 4 nm). The average height of the gold nanostructures measured 13 ± 3 nm, with lateral dimensions ranging from 32 to 53 nm.
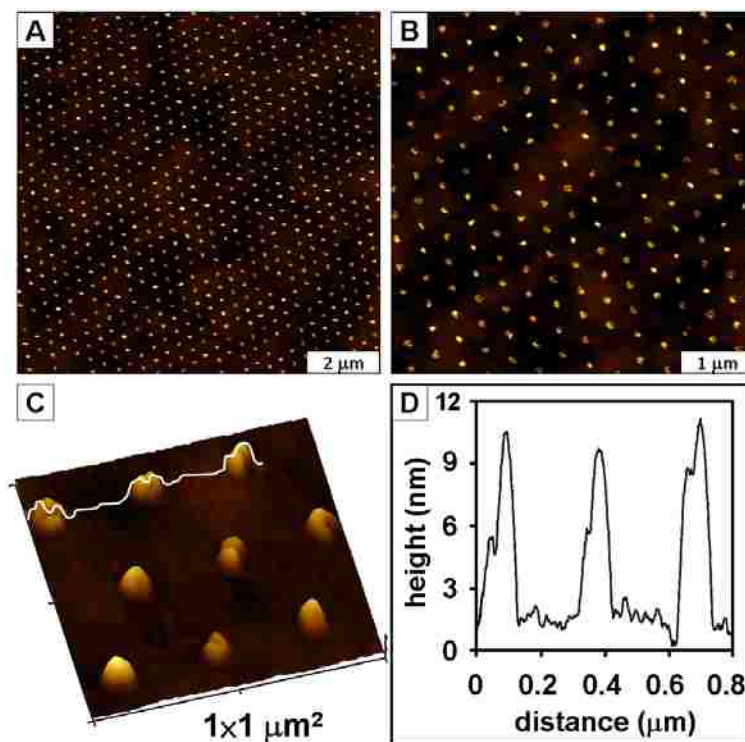
Figure 6.9 Successive magnified views of the clusters of gold nanoparticles produced on Si(111). (A) Wide area topograph of periodic arrays of gold nanoparticles (10×10 μm^2); (B) close-up view of the nanoparticle aggregates (5×5 μm^2); (C) zoom-in view of the clusters of gold nanoparticles (1×1 μm^2); (D) cursor profile for the line in C.

Characterizations with ultraviolet-visible spectrophotometer were used to investigate the optical property of arrays of gold nanoparticle clusters (Figure 11). For comparative reference, UV-Vis spectra were acquired for a gold nanoparticle solution and for a piece of glass with organosilane nanopatterns. A significant absorption peak was observed at 521 nm in the UV-Vis spectrum for the solution of suspended gold nanoparticles (green curve in Figure 11). The

spectrum in Figure 11 (blue curve) does not exhibit a prominent absorption peak in the visible region (350-700 nm). For the sample of gold nanoparticles adsorbed onto nanopatterned surfaces, a remarkable red-shift up to a value of 632 nm was observed in the UV-Vis spectrum (red curve in Figure 11). The red spectral shift is attributed to the changes of interparticle distance as gold nanoparticles assemble on the confined areas of the surface.[234-237] With spatially directed confinement of gold nanoparticles on nanopatterned glass surfaces, the arrays of nanoparticles aggregates retain characteristic optical properties.
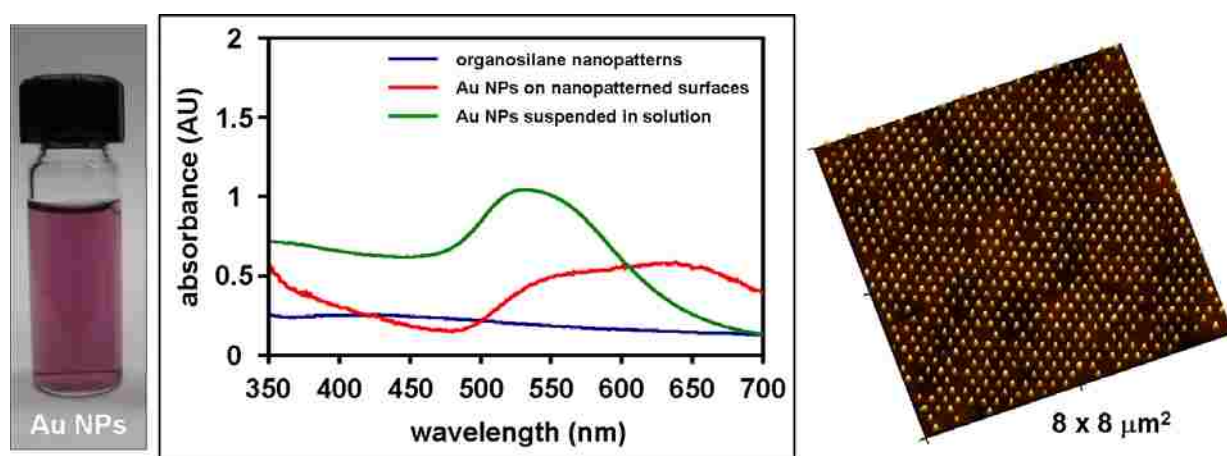
Figure 6.10 Investigating the optical property of arrays of gold nanoparticle clusters with ultraviolet-visible spectrophotometer. Red curve is the spectra of the gold nanoparticle solution. Blue curve corresponds to spectra of nanopatterned surfaces without gold nanoparticle adsorbed. Green curve displays the spectra of arrays of gold nanoparticle clusters produced using selective adsorption.

6.4 Conclusion

Particle lithography provides advantages of high throughput for patterning organosilanes, furnishing nanoscale control of the surface coverage, geometry and dimensions of nanostructures. If there was ever a concern that molecularly thin films could be used effectively to spatially define sites for successive stepwise chemistry or to direct the adsorption of nanomaterials at very small size scales, the examples presented should definitively illustrate the capabilities of surface

chemistry for defining spatial selectivity. This report is a prelude to new directions for nanoscale

patterning, with bench chemistry steps that are accessible in most laboratories.

CHAPTER 7. DETECTING THE MAGNETIC RESPONSE OF IRON OXIDE CAPPED ORGANOSILANE NANOSTRUCTURES USING MAGNETIC SAMPLE MODULATION AND ATOMIC FORCE MICROSCOPY

7.1 Introduction

Studies of the size-scaling effects for magnetic nanomaterials are an important direction for surface investigations, if the difficulties for characterizing properties at very small dimensions can be overcome. Understanding magnetic size scaling is not only important for understanding the behavior of existing nanomaterials but is also valuable for efforts to develop new materials with engineered properties. Magnetic nanomaterials are used for magnetic fluids,[238-240] catalysis,[241-243] magnetic separations,[244-246] magnetic resonance imaging,[247-249] data storage[250-252] and biosensing/biomedical technologies.[253-255] In this chapter, a hybrid AFM mode will be described for highly sensitive and selective characterizations of the vibrational motion of magnetic nanomaterials responding to the flux an alternating electromagnetic field.

For scaling effects of magnetic nanomaterials, precise knowledge of the relationships between particle shape and size, surface structure and the resulting magnetic properties is incomplete. The fundamental magnetic properties of nanomaterials, such as blocking temperature, spin lifetime, coercivity and susceptibility are influenced by size scaling.[42, 256] Changes of magnetic properties with nanoscale dimensions are not well defined even for simple particles composed of pure materials such as Fe, Co, or Ni, whereas the bulk properties are well understood.[257] Basically, the physics and properties of magnetic nanostructures cannot necessarily be inferred from scaled down properties of bulk materials.[258] Unique magnetic phenomena are exhibited for nanoparticles, which are different than bulk properties. As particle sizes decrease, more of the atoms of a nanoparticle are surface atoms; therefore surface and interface effects predominate.[10] For magnetic materials, surface effects can lead to a decrease of

the total magnetization in comparison to the bulk value, such as for oxide nanoparticles.[259] However, an enhancement of the magnetic moment was reported for metal nanoparticles of cobalt.[260] Another surface-driven effect is enhancement of the magnetic anisotropy, K_{eff} with decreasing particle size.[260, 261]

Several measurement modes with scanning probe microscopy (SPM) provide surface characterizations for evaluating size-dependent effects for scaling magnetic properties. Imaging modes have been developed such as magnetic resonance force microscopy (MRFM),[262-265] magnetic AC or MAC-mode,[266-269] and magnetic force microscopy,[270-273] however all of these methods require the use of tips with a magnetic coating. Magnetic probes can be problematic, since the magnetic properties of the thin metal films which coat the underside of the probes diminish over time, requiring remagnetization. Also, after continuous contact mode scanning, the thin metal films can be worn away. The thickness of the magnetic coatings is on the order of tens of nanometers, which greatly decreases resolution for imaging small surface features. Intrinsically, the resolution of SPM methods depends on the geometry of the coated probe; and metal coatings produce relatively large, blunt tips.

The conventional approach for magnetic imaging with SPM is known as magnetic force microscopy (MFM).[274-279] For MFM, a tip that is coated with a magnetic material is operated in non-contact mode, and used as a magnetic force sensor to detect the relatively weak long-range forces of magnetic areas of surfaces operating over distances from 50-200 nm. Thus, for MFM the magnetic field of the sample must be strong enough to deflect or attract a micrometer-sized cantilever for mapping the surface domains. The MFM approach provides a means to map the strength of the magnetic field at various distances, (e.g. 50, 100, 150 nm) from the surface. Thus, MFM indicates the relative strength and polarity of magnetic regions. The limits of MFM

detection intrinsically depend on the size and spring constant of the magnetic lever. The lateral resolution of MFM is related to the dimensions of the magnetic coating at the apex of the probe, with a metal film thickness that is typically ~100 nm.[280, 281]

This chapter presents a new approach for mapping the magnetic response of nanomaterials by combining magnetic sample modulation with contact mode AFM. The method employs a soft, non-magnetic cantilever operated in contact mode for detecting the physical motion of nanoparticles which are driven to vibrate by an AC electromagnetic field. The periodic motion of the sample vibration can be tracked by changes in the deflection of the tip. The changes in phase angle and amplitude as the tip interacts with the vibrating sample are plotted as a function of tip position to create MSM phase and amplitude images. Also, frequency spectra of the nanomaterials in response to an applied magnetic field can be acquired with MSM by placing the AFM tip in direct contact with a vibrating nanostructure and sweeping the field frequency. A key strategy for these investigations was to use particle lithography to produce arrays of regular nanostructures as test platforms with tailorable sizes and spacing.[36] Successive steps of particle lithography, chemical vapor deposition and electroless metal plating were used to fabricate arrays of iron oxide nanostructures as model test platforms for MSM characterizations.[39] Millions of nanostructures can be reproducibly prepared with relatively few defects and high surface density to enable multiple successive SPM measurements of well-defined structures.

7.2 Materials and Method

7.2.1 Materials and Reagents

Octadecyltrichlorosilane (OTS) and 3-mercaptopropyltrimethoxysilane (MPTMS) were purchased from Gelest (Morrisville, PA) and used without further purification. Iron (II) chloride tetrahydrate (ReagentPlus), sodium nitrite (ACS Reagent) and sodium acetate were obtained

from Sigma-Aldrich (St. Louis, MO). Silicon wafers doped with boron (Virginia Semiconductor Inc., Fredericksburg, VA) were used as substrates. Silicon wafers were cut into small pieces (1×1 cm^2) and cleaned by immersion in Piranha solution for one h. Piranha solution is a mixture of sulfuric acid (96%, EMD Chemical Inc., Gibbstown, NJ) and hydrogen peroxide (30%, Sigma-Aldrich) at a ratio of 3 : 1 (v/v). This solution is highly corrosive and should be handled carefully. Silicon substrates were then rinsed with deionized water (Milli-Q, Millipore, Bedford, MA) and dried in ambient air. Monodisperse polystyrene latex solutions were purchased from Duke Scientific (Palo Alto, CA). The latex spheres were washed twice with deionized water by centrifugation to remove contaminants such as charge stabilizers or surfactants. A pellet is formed by centrifuging latex suspensions for 15 min at 14000 rpm, which can then be resuspended in aqueous solutions.

7.2.2 Scanning Probe Microscopy

An Agilent 5500 SPM system equipped with a multipurpose AFM scanner (maximum area 11 x 11 μm^2) was used for surface characterizations (Agilent Technologies, Tempe, AZ). The scanner was operated with open-loop feedback for continuous imaging in contact mode. A magnetic AC mode (MAC-mode) sample plate was used to generate an alternating electromagnetic field for MSM. The scanner has a scanning tip configuration, which incorporates interchangeable nose cones for various imaging modes. An empty plastic nose cone assembly without metal components was used for MSM imaging. Picoscan v5.3.3 software was used for data acquisition. Digital images were processed with Gwyddion (version 2.9) open source software supported by the Czech Metrology Institute, which is freely available on the Internet.[138] Commercially available non-magnetic silicon nitride cantilevers with force constants ranging from 0.1 to 0.5 N m^{-1} were used for AFM imaging, (Veeco Probes, Santa Barbara, CA).

7.2.3 Sample Preparation

Samples to be interrogated by MSM must be moveable, which underscores the critical role of lithography approaches for sample preparation. Custom test platforms of magnetic nanostructures were prepared using successive steps of particle lithography, organic vapor deposition and electroless deposition of iron oxide, to enable AFM characterizations at the level of individual nanostructures.[36] The steps for fabricating nanostructured test platforms are outlined in Figure 7.1. First, an aqueous solution containing monodisperse latex particles (200 nm) was deposited on clean Si(111) substrates. Next, the sample was dried in air to form a latex film. As the water evaporates during drying, capillary forces draw the latex spheres together to form organized crystalline layers. The film of close-packed latex particles provides an evaporative mask for heated vapor deposition of organosilanes. The colloidal masks were placed into a reaction vessel containing a few drops of neat OTS (300 µL). To generate a vapor, the vessel was placed in an oven at 70 °C under ambient pressure. During heating, a vapor of OTS is produced in which the vapor-phase molecules permeate between latex spheres of the colloidal mask and adsorb onto the uncovered interstitial areas of the substrate. After cooling, the latex particles were then removed by sonication in ethanol (ACS grade, Pharmco, Aaper, TX) for 15 min, followed by rinsing with ethanol and deionized water. Nanopatterns of OTS remain covalently bound to silicon substrates and were not removed by the rinsing step.

In the next lithography step, a second molecule was deposited by immersion to backfill uncovered areas of the surface. The pores of the OTS patterns were filled by immersing the sample in a solution containing 0.1 mM MPTMS in toluene (reagent grade, EMD Chemical Inc., Gibbstown, NJ) for 4 h. The sample surface was then further cleaned by successive sonication in toluene and ethanol for 15 min. The final step employed electroless deposition to generate

nanostructures of iron oxide (Fe_3O_4) on MPTMS nanopatterns.[282, 283] A 10 mM solution of iron

(II) chloride tetrahydrate in sodium acetate buffer (65 mM) at pH 7.4 was mixed with a 30 mM

solution of sodium nitrite at a ratio of 10:1 ($FeCl_2$: $NaNO_2$, v/v). The patterned substrates were

immersed in the mixed solutions for 25 min at 70 ºC for electroless deposition. Afterwards the

samples were rinsed with deionized water and dried in air. A model of the nanostructures

produced using electroless deposition of iron oxide on MPTMS nanopatterns is presented in

Figure 7.1.
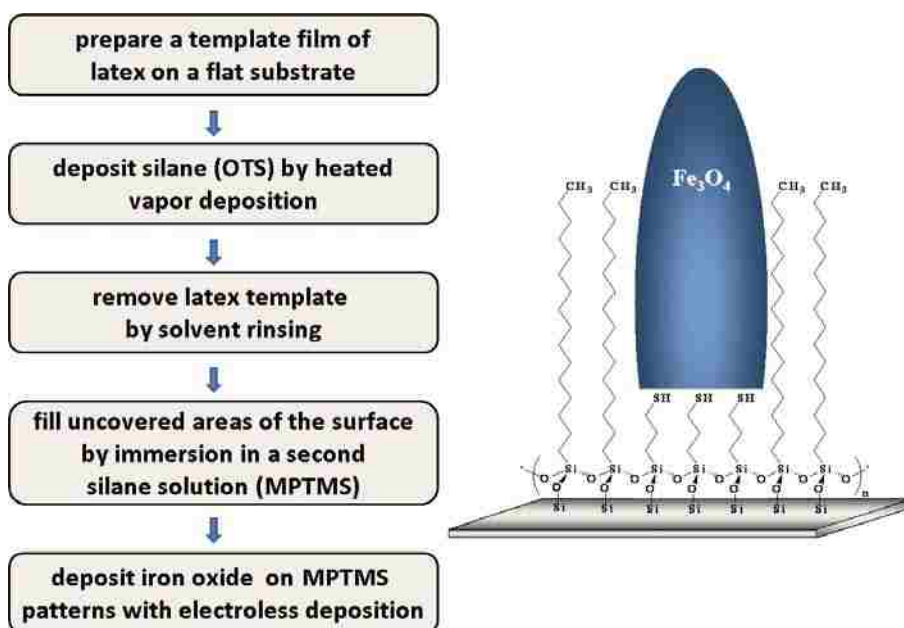
Figure 7.1 Steps for fabricating magnetic nanostructures (left); model for iron oxide nanostructures formed on MPTMS nanopatterns (right).

Topographic views of the test platforms acquired using conventional contact-mode AFM

are shown in Figure 7.2. The upper row displays 2D and 3D images of the OTS nanopatterns

before the steps of backfilling with MPTMS and metal deposition. The bottom row reveals

surface changes after forming metal nanostructures. A relatively wide area of the surface is

presented in Figure 7.2A for an 8×8 μm^2 frame, which is representative of the morphology

throughout the entire sample. The morphology of the underlying surface of a polished silicon

87

wafer is apparent; uncovered substrates have an RMS roughness of 2.4 nm. A high surface density and periodic arrangement of rings are prominent in Figure 7.2A, there are approximately 1900 nanopatterns within this image, which scales to 3×10^9 nanopatterns/cm^2. Zooming in for a closer look, the 1×1 μm^2 topograph reveals the regular geometries and interpattern registry of the OTS nanopatterns (Figure 7.2B). The center-to-center spacing corresponds to the diameter (200 nm) of the mesosphere mask; however, the central pore areas which define locations for depositing MPTMS and iron oxide are much smaller, ranging from 56 to 67 nm. The heights measured for the ring nanostructures is 2.6 ± 0.4 nm, which matches well with the predicted 2.5 nm height for a densely packed OTS self-assembled monolayer (SAM) with an upright orientation (Figure 7.2C). The areas surrounding the ring structures evidence height changes after OTS adsorption; however the density and surface coverage are lower for the areas between the rings. The central areas of some of the pores evidence small residues of OTS, which are likely caused by imperfect contact of the latex spheres with the silicon surface. The latex spheres mask a well-defined circular geometry for the subsequent backfilling step with MPTMS. Thiol-terminated MPTMS was used to link the metal nanostructures to the surface, whereas OTS furnishes a hydrophobic interface to spatially constrain and confine the deposition of iron oxide selectively in the regions with MPTMS.

An array of Fe$_3$O$_4$ deposits formed on the templates of MPTMS/OTS nanopatterns is demonstrated in Figures 7.2D and 7.2E. After the electroless deposition step, rows of metal dots are observed throughout areas of the surface arranged in a regular periodic array. A representative topograph is shown in Figure 7.2D which corresponds to the same size area as Figure 7.2A. The interstitial areas that are covered with methyl-terminated OTS provide an effective resist for preventing metal adsorption, whereas the pore regions filled with MPTMS

define surface attachment sites presenting sulfur groups to direct metal binding. The zoom-in view of Figure 7.2E reveals the remarkable symmetry and uniformity of 28 iron oxide nanostructures. An average periodicity of 208 ± 12 nm was measured for the arrays of iron oxide nanostructures, which closely matches the dimensions of the latex masks (Figure 7.2F). With electroless deposition, the growth of a few nanometers of Fe_3O_4 occurs rapidly, within 30 min. The average height of the iron oxide nanostructures is 10 ± 3 nm, and the lateral dimensions ranged from 39 to 75 nm with an average size of 56 ± 10 nm. The height of the nanostructures can be tailored by changing the immersion intervals or concentration of the plating solutions. Size analysis of 56 iron oxide nanostructures revealed a size variation of 26 %. The variability at the nanoscale for the dimensions of iron oxide nanostructures furnishes a useful geometry parameter for comparing magnetic response with MSM characterizations.
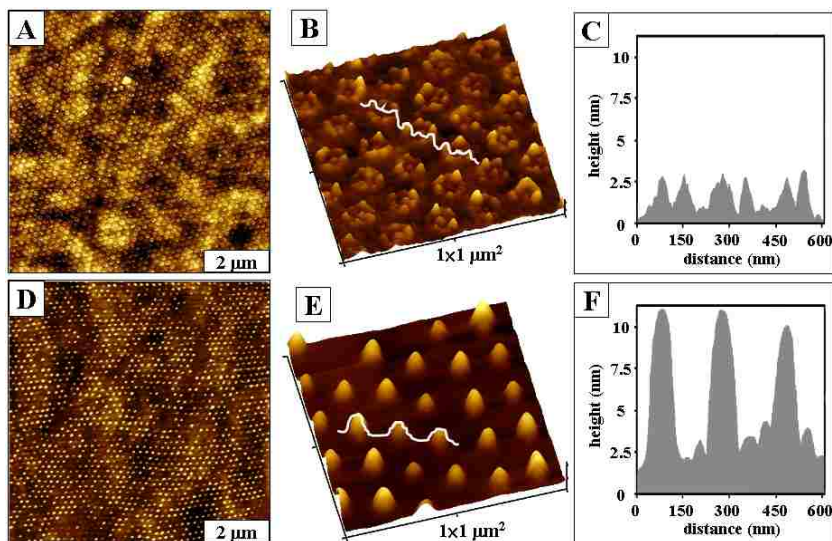
Figure 7.2 Particle lithography produces regular periodic nanostructures for MSM. (A) Topograph of OTS nanopatterns; (B) close-up view; (C) cursor profile for the line in B. (D) Topograph of iron oxide nanostructures; (E) zoom-in view; (F) cursor profile for the line in E.

7.2.4 Operating Principle for Magnetic Sample Modulation AFM

The instrument set-up for MSM is a hybrid of contact mode AFM combined with selective actuation of magnetic samples (Figure 7.3A). For the typical imaging procedure, first

conventional contact mode images are acquired without applying a magnetic field. Next, the same area of the surface is scanned again with an applied oscillating electromagnetic field. The polarity, oscillation and flux of the magnetic field are generated and controlled by selection of parameters for the AC current applied to the wire coil solenoid, which is located underneath the sample plate. A photograph of the underside of the sample stage is shown in Figure 7.3B. The center of the plate contains a wire coil solenoid embedded within an epoxy resin. When an electromagnetic field is applied to samples, only the magnetic domains are driven to vibrate, providing selective contrast for areas that are in motion. The differences for images with and without an applied magnetic field are used to map magnetic domains. Changes in the phase and amplitude of vibrating nanomaterials are mapped relative to the driving AC current applied to the solenoid. A lock-in amplifier is used to acquire the amplitude and phase components of the deflection signals, which furnishes exquisite sensitivity for slight changes in tip movement. Using MSM, responses of both the amplitude and phase signal simultaneously acquired with the topographic channel, as well as spectra of the vibrational response, can be mapped with angstrom resolution.
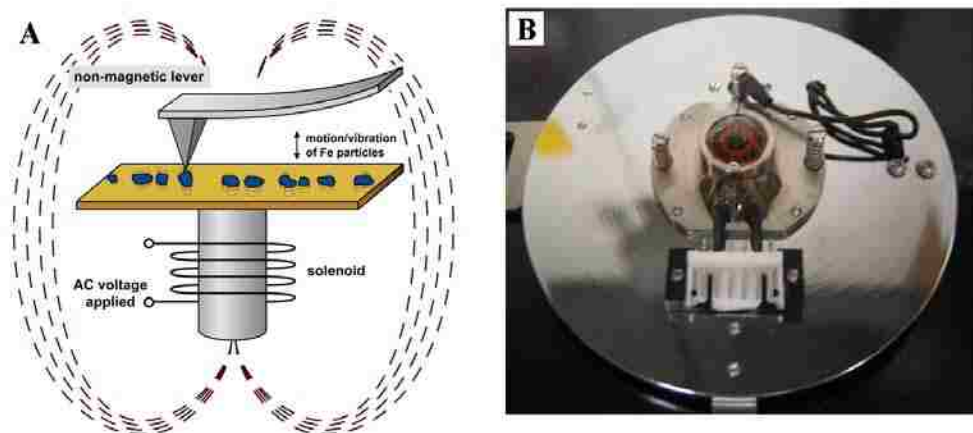
Figure 7.3 Imaging concept for magnetic sample modulation AFM. (A) Instrument setup; (B) photograph of a wire coil solenoid located underneath the sample plate.

For the instrument setup of MSM, the typical force-deflection settings for scanning in contact mode are used for topographic data acquisition. For conventional contact mode AFM, the tip is scanned in continuous contact with the surface in an X-Y raster pattern, as illustrated in Figure 7.4A. The beam from a diode laser is focused onto the back of the AFM cantilever, and deflected to a quadrant photodetector. As the tip is rastered across the surface, changes in the tip position as it profiles the surface features correspondingly change the amount of light incident on the quadrants of the detector. The feedback loop of the AFM scanner adjusts the voltages of the piezoscanner to maintain a certain set-point corresponding to the initial tip deflection. The voltage changes for positional adjustment are mapped with the X-Y position of the tip to generate a 3D map of surface topography and friction.[12, 284-289]

Typically, the magnetic AC (MAC) mode uses a sample stage with a wire coil solenoid to drive the oscillation of an AFM tip for tapping, when using a cantilever with a magnetic coating on the top side of the probe (Figure 7.4B). For MAC-mode, an AC voltage is applied to the solenoid of the sample plate to generate a magnetic field which alternates in polarity, frequency and strength to precisely drive the actuation of the tapping tip.[266, 290] A tip that is coated with a magnetic film is required for MAC-mode imaging. The positional feedback for tapping mode is quite different from contact-mode AFM. The voltages applied to the piezoscanner are adjusted to maintain a constant amplitude of tip oscillation. For MAC-mode the tip is driven to intermittently "tap" the surface to minimize stick-slip adhesion and prevent damage to soft or sticky samples. Two key differences between contact versus tapping mode AFM are the feedback mechanisms for controlling the tip position as well as the presence/absence of tip oscillation. In contrast, the setup for MSM imaging requires non-magnetic probes. For MSM

imaging, a MAC-mode sample stage is used to apply an AC electromagnetic field to drive the sample vibration rather than for driving tip oscillation.

Force modulation AFM is a related imaging mode, in which the entire sample is induced to vibrate as the tip is operated in continuous contact with the sample surface (Figure 7.4C).[11, 131, 291-293] The sample is driven to oscillate at a selected frequency and amplitude while using the force-deflection feedback loop typical of contact mode AFM. When the modulated surface is interrogated by the AFM tip, energy transfer causes the cantilever to vibrate. Amplitude and phase signals are generated simultaneously with acquisition of topographic information. The dampening or enhancement of the amplitude and phase components of the cantilever vibration depends sensitively on the softness and viscoelastic properties of the sample.
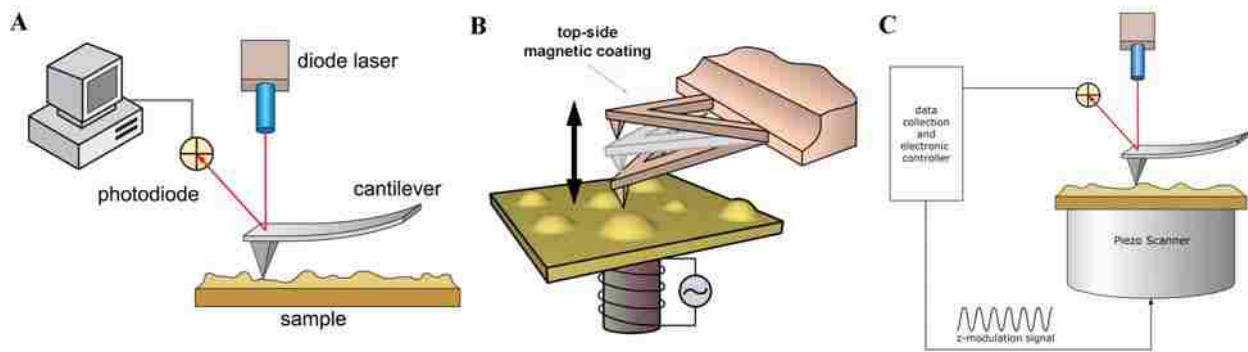
Figure 7.4 Operating principle of AFM imaging modes that are related to MSM imaging. (A) Contact-mode; (B) MAC-mode; (C) Force modulation AFM.

The approach for MSM imaging is a hybrid of three AFM imaging modes, in which the tip is operated in contact mode using a MAC-mode sample plate to apply an alternating magnetic field for selective modulation of magnetic domains. Essentially, MSM is a variant of force modulation AFM with selectivity for actuating and characterizing magnetic nanomaterials. With MSM, the periodic motion of the sample vibration can be tracked by changes in the deflection of the tip. Changes in the phase angle and amplitude as the tip interacts with the vibrating sample

are plotted as a function of tip position to create MSM phase and amplitude images. Digital channels for the amplitude and phase components of the tip motion are obtained by directing an auxiliary output channel from the photodiode to the input of a lock-in amplifier, using the driving AC waveform as a reference signal. The mechanical motion of the sample will produce differences in contrast exclusively for vibrating domains responding to the flux of the magnetic field. With MSM imaging, the differences displayed for images with and without an applied magnetic field are used to selectively map areas of magnetic nanomaterials.

For MSM imaging, it is important to select a tip holder assembly (nose cone) and non-magnetic tip to ensure that the tip is not driven to oscillate. A magnetized probe or tip assembly would respond directly to the flux of the magnetic field and thereby interfere with the tip-sample response. For the MSM set-up, the flux of the alternating magnetic field selectively induces mechanical vibration for magnetic nanomaterials on surfaces. The dynamic motion of the magnetic nanomaterials driven by an oscillating magnetic field is sensed by an AFM tip only when it touches the vibrating domains. Only magnetic domains vibrate, providing selectivity. The spectra of the vibrational responses as the frequency or strength of the AC electromagnetic field are ramped can also be plotted with nanoscale resolution using MSM, to enable dynamic imaging protocols.

7.3 Results

7.3.1 Mapping Magnetic Nanomaterials Using Magnetic Sample Modulation (MSM)

Images were acquired with MSM for samples prepared with and without electrolessly deposited Fe_3O_4 nanostructures. Samples without iron oxide nanopatterns were tested as a control. Images and frequency spectra of the nanostructures without metal deposits are shown in Figure 7.5. The data was acquired using contact mode AFM while an AC electromagnetic field

of 0.29 T was applied to the sample stage. The topography channel displays a periodic array of organosilane ring structures spaced at 200 nm intervals (Figure 7.5A). There are approximately 124 nanopatterns within Figure 7.5A and the nanostructures cover ~31 % of the surface, exhibiting uniform thickness and geometries. No surface features are evident in the amplitude (Figure 7.5B) or phase channels (Figure 7.5C) when the AC electromagnetic field is applied, as would be expected for non-magnetic materials. When sweeping the frequency of oscillation from zero to 300 kHz, only a few small background blips are detected for the baseline of the control sample, resonance peaks are not evident with applying the flux of a magnetic field (Figure 7.5D).
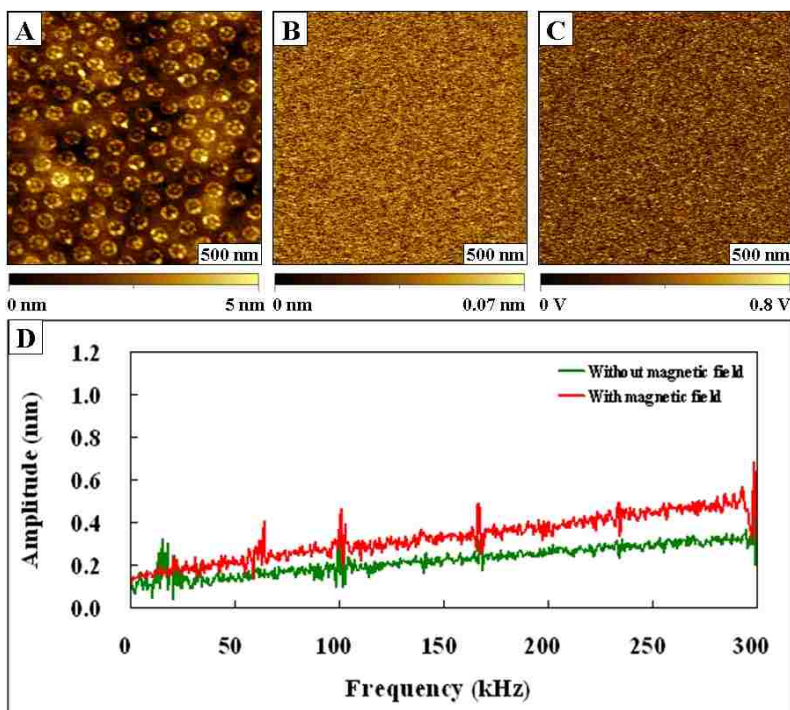
Figure 7.5 Control sample of organosilane nanostructures imaged with MSM (without metal deposits). (A) Topography frame (2×2 μm^2) acquired with an applied AC magnetic field of 0.1 T; (B) concurrently acquired amplitude and (C) phase images for the same area. (D) Frequency spectra for the control sample.

Successful results for imaging the iron oxide nanostructures with MSM are presented in Figure 7.6. The color scales were selected arbitrarily to readily map and identify the oscillating

94

magnetic domains. For MSM imaging a field strength of 0.29 T at a frequency of 42 kHz was applied to induce sample vibration. The topography frame reveals the size, shape and arrangement of the metal deposits; approximately 19 % of the total surface is covered with iron oxide nanostructures. Within the $2 \times 2 \ \mu m^2$ area there are 117 nanostructures, which scales up to $\sim 10^9$ nanostructures per cm^2. Both amplitude and phase images clearly resolve the locations of magnetic domains (Figures 7.6B and 7.6C). Thus, the flux of the AC electromagnetic field produces sufficient mechanical motion of the magnetic nanostructures to produce a detectable response with the AFM probe. The AFM tip response has a periodic motion that can generate changes in amplitude and phase channels for the vibrating magnetic domains. The color scales chosen for the phase and amplitude channels do not reflect changes in magnetic polarity. The phase channel would require complex algorithms to interpret, due to the periodic nature of the sinusoidal AC waveform of the driving current. However, the magnitude of the changes in amplitude response corresponds to changes in the tip deflection in the z-direction, on the order of 1-5 nm. The amplitude response was scaled in nm, to indicate the displacement of the AFM tip as it interacts with vibrating nanostructures.

The resonance spectrum of the AFM tip when placed in contact with the iron oxide nanostructures (Figure 7.6D) displays multiple broad peaks in the presence of an applied AC electromagnetic field. The maximum resonance occurs at a frequency of 42 kHz, which is different than the natural resonance of the cantilever (28 kHz). When the tip is lifted from the surface, no peaks are detected in the presence of the applied field. The probe must be placed directly in contact with the surface of a magnetic nanostructure to obtain a frequency profile such as in Figure 7.6D. Resonance spectra provide a convenient means to optimize the experimental parameters (driving frequency and field strength) for MSM imaging.
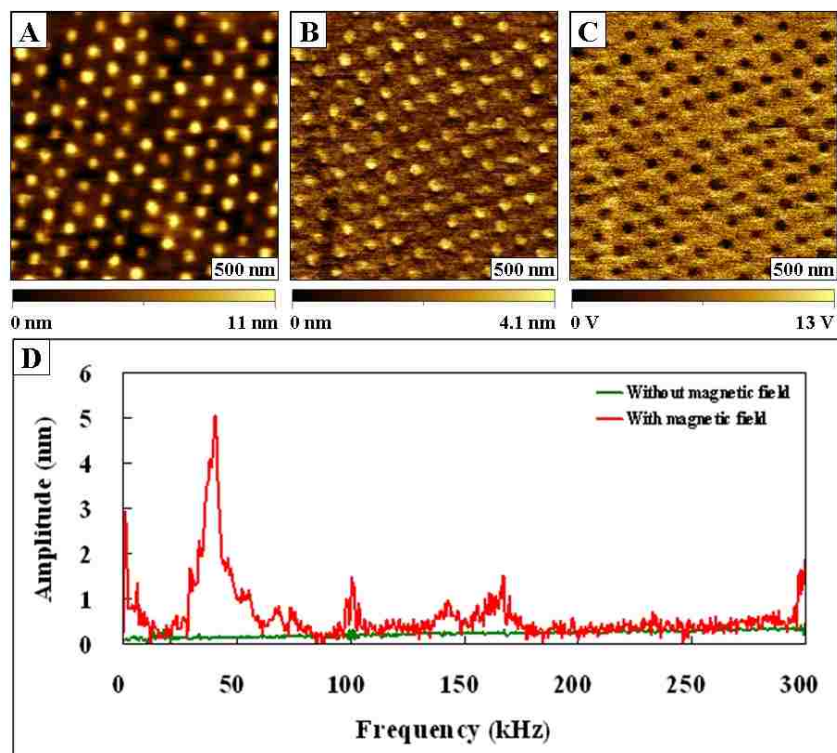
Figure 7.6 Images of iron oxide nanostructures acquired using MSM. (A) MSM topography frame (2×2 μm^2); (B) corresponding amplitude and (C) phase channels; (D) plot of frequency sweep when the tip was placed on an iron oxide nanostructure.

As the samples are scanned with MSM, parameters such as the field strength and driving frequency can change images at any point during image acquisition. To demonstrate changes in the vibration of magnetic domains induced with MSM, an image was acquired with and without applying the AC electromagnetic field (Figure 7.7). The sample was scanned beginning at the bottom of the frame with the field turned off. After scanning half of the image area, an AC magnetic field of 0.29 T was applied. Within the 2×2 μm^2 topographic frame, the resolution and view of the array of Fe_3O_4 nanostructures has not noticeably been changed when the field is turned on (Figure 7.7A). The magnitude of the vibration is on the order of a few nm, which is relatively small. However, the changes in the amplitude and phase channels (Figures 7.7B and 7.7C) when the field is activated become apparent immediately.

96
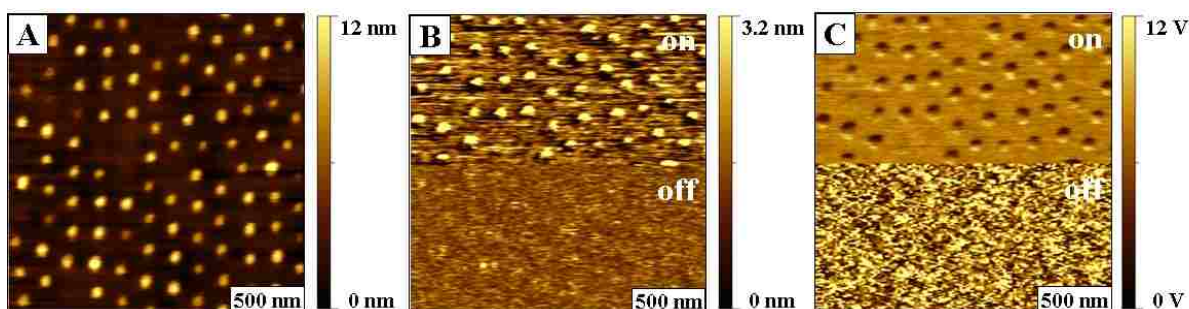
Figure 7.7 Changes for MSM images when the field was activated during the process of data acquisition. (A) Simultaneously acquired topography; (B) amplitude; and (C) phase images acquired with and without the alternating magnetic field.

7.3.2 Effect of Changing the AC Frequency Parameter

Changes in the vibration of magnetic domains driven by the external magnetic field can be investigated *in situ* by successively changing the frequencies for driving the AC electromagnetic field during data acquisition of a single image (Figure 7.8). This protocol enables investigations of the frequency or amplitude dependence of imaging magnetic domains by autoscaling a side-by-side comparison within a single frame. Figure 7.8 presents MSM images acquired with four different frequencies near the resonance peak position, with an applied magnetic field strength of 0.29 T. The frequencies were changed *in situ* without halting data acquisition. Artifacts, such as transition bands or line spikes, were not produced for the topographic image (Figure 7.8A). Views of the morphology of the iron oxide nanostructures are not noticeably affected by changes in modulation frequencies in the topography frames. However, differences are clearly apparent in amplitude and phase channels (Figures 7.8B and 7.8C). The amplitude frame correlates with the magnitude of the tip response, and the changes follow accordingly with the height of the peak positions of the frequency profile. The maximum peak height evidences the greater change in the magnitude of vibration response. Four frequencies were selected along the broad resonance peak, 42 kHz, 34 kHz, 23 kHz and 12 kHz. At the maximum resonance frequency of 42 kHz, the magnetic domains exhibit sharp contrast for both the amplitude and phase frames. For the

97

frequencies below 42 kHz, the images display correspondingly smaller changes in contrast within the amplitude image. Due to the periodic nature of the sinusoidal AC waveform of the driving current for MSM, changes observed for the phase channel are difficult to interpret. Trends for changes in the phase images of the tip oscillation do not scale with the magnitude of the tip displacement. For example, the phase response at 23 kHz is sharper and more readily distinguishable than observed at the resonance peak of 42 kHz. Phase images often visualize the finer details of surface shapes, such as for defining the boundaries and lateral dimensions of nanostructures. The experiment of Figure 7.8 indicates that MSM imaging is highly sensitive according to the parameters selected for the driving modulation frequency.
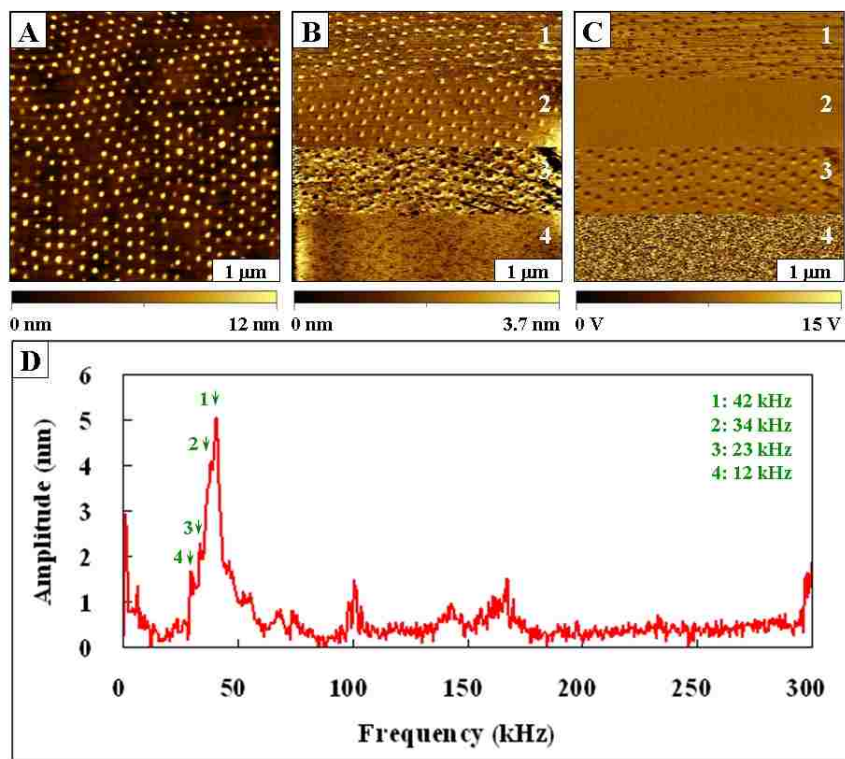
Figure 7.8 Dynamic modulation experiment for autoscaling changes in MSM images as the resonance frequencies are changed *in situ*. (A) Topograph (4×4 µm^2); (B) amplitude image; (C) phase image; (D) frequencies selected for the modulation parameters.

The flux of the alternating electromagnetic field selectively induces vibrational motion for magnetic nanomaterials on surfaces during acquisition of MSM frequency spectra. A

comparison of frequency spectra at different field strengths is presented in Figure 7.9. Three levels of electromagnetic field strength were selected to evaluate the changes in frequency spectra. For non-magnetic nanopatterns of OTS, prominent changes were not observed within the frequency spectra as the strength of field was successively increased from 0 to 2.9 T (Figure 7.9A). Only a few small background signals are apparent within the frequency range of 0 to 300 kHz. The control experiment demonstrates that the tip does not vibrate in response to the applied AC field. When the tip was placed in contact with an iron oxide nanostructure (Figure 7.9B) multiple broad peaks became apparent in the presence of an applied magnetic field. Multiple resonance peaks were observed as the field strength was increased, and the magnitude of the peaks also increased accordingly with field strength. The resonance frequency was observed to shift from 45 kHz (0.12 Tesla) to 42 kHz (0.29 Tesla) depending on field strength.
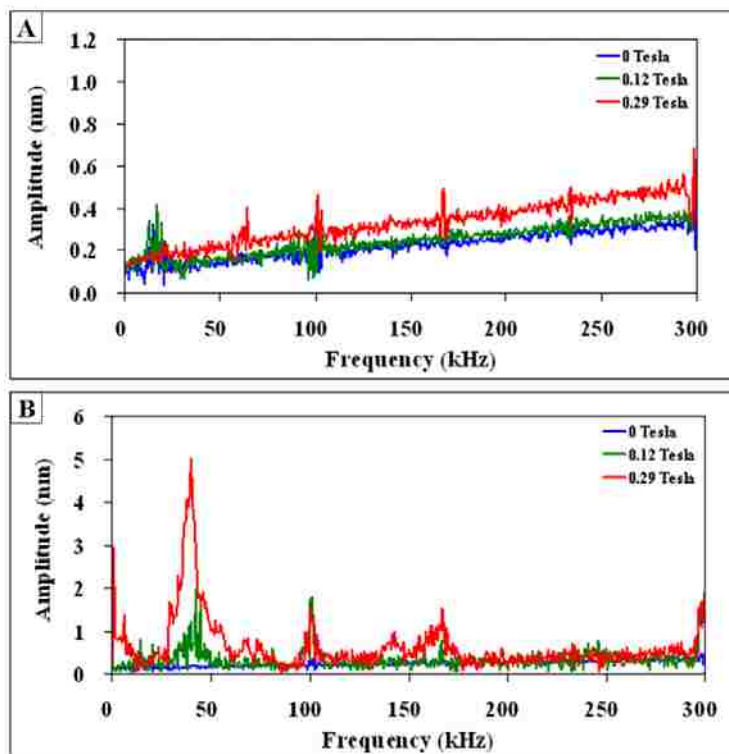
Figure 7.9 Changes in MSM frequency spectra as the strengths of the applied electromagnetic field varied. (A) Frequency spectra for organosilane nanopatterns; (B) frequency profiles acquired with iron oxide nanostructures.

7.3.3 Investigation of Size-Dependent Properties of Magnetic Nanostructures Using MSM

An analysis of the trend in size versus the displacement measured by cursor profiles for the MSM amplitude images is shown in Figure 7.10 for the Fe_3O_4 deposits of the previous example. Cursor analysis of 100 iron oxide nanostructures from MSM amplitude images were plotted as a function of the lateral size of the deposits. The amplitude of the tip oscillation becomes greater for larger iron oxide nanostructures, within the size range displayed. As the size and volume of ferromagnetic materials is increased, mass magnetization increases.[256, 294] The chart of Figure 7.10 reveals that within the size range of 38-77 nm, a greater vibrational amplitude is observed for larger iron oxide deposits for electrolessly deposited Fe_3O_4, which follows the predicted linear trend of size scaling for mass magnetization effects. The trend line for the experimental measurements generated an R^2 value of 0.912. Nanomaterials of Fe_2O_3 and Fe_3O_4 are known to exhibit superparamagnetic properties under applied magnetic fields.[10, 295-297] For this size regime, the linear trend of Figure 7.10 follows the predictions of the scaling laws known for bulk ferromagnetic materials. The amount of vibration scales proportionately with the size of magnetic domains.
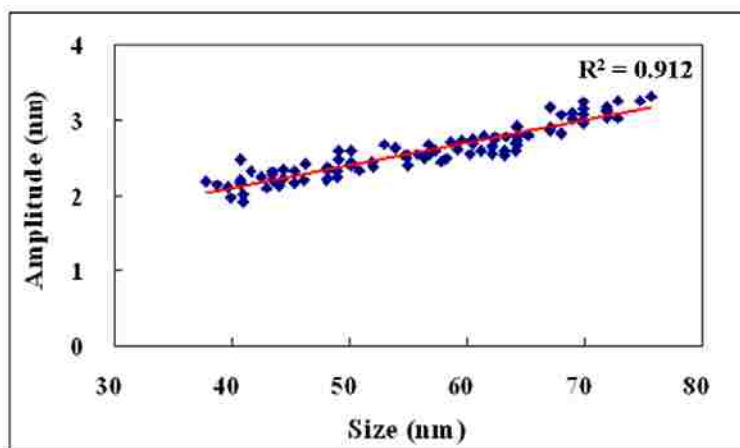
Figure 7.10 The amplitude response was shown to scale linearly with the size of magnetic nanostructures.

7.4 Discussion

In nearly all of the established modes of SPM imaging, the nature of the tip is used as a mechanism for detection of forces. For example, a biased tip is used for scanning polarization force microscopy;[298-300] a magnetized tip is used for magnetic force microscopy;[274, 301-303] a chemically functionalized tip is used for chemical force microscopy;[13, 304] a metal tip is used for current imaging;[14, 305-307] an actuated tip is used for tapping mode and phase imaging[228, 230, 308-310] and so on. Unlike previous SPM imaging modes which use specifically designed tips to interrogate samples, for MSM imaging the changes in *sample dynamics* form the basis for measurements of magnetic properties. The sample is driven to vibrate in response to an externally applied electromagnetic field and the tip is used as a force and motion sensor for mapping the vibrational response. For MSM, the samples are induced to vibrate in concert with the flux of an externally applied electromagnetic field. A soft, *non-magnetic* AFM tip is operated in contact mode to detect the force and motion of magnetic nanomaterials which vibrate according to the rhythm of the externally applied oscillating magnetic field. Lock-in-detection is used for sensitively tracking changes in the amplitude, phase and frequencies of motion compared to the driving AC electromagnetic field. The MSM technique provides exceptional sensitivity and is selective for distinguishing samples which have a magnetic moment in the presence of an applied AC electromagnetic field.

The proof-of-concept results with test platforms of iron oxide nanostructures demonstrate successful characterizations using the MSM imaging mode. For mapping the vibrational response of magnetic nanomaterials, patterned surfaces of organosilane SAMs were used to prepare test platforms, to ensure that magnetic nanomaterials can move and vibrate in response to an externally applied magnetic field. The silane SAMs serve as linker groups for anchoring

metal deposits to the surface. The organosilanes enable a spring-like response for the motion of metal deposits. With the designed silicon-silane-metal nanostructures, the iron oxide deposits can be induced to vibrate in response to the flux of the applied field. If the magnetic materials were embedded within the surface, then vibration could not be detected with the MSM imaging mode. However, the MSM mode is well suited for characterizations of the magnetic response of individual composite nanostructures containing magnetic elements, or systems of magnetic nanoparticles. Future reports will disclose MSM results which have been acquired for other systems of smaller magnetic nanoparticles and ferroproteins, such as ferritin.

Understanding magnetic size scaling is not only important for understanding the behavior of existing nanomaterials but is also valuable for efforts to develop new materials with engineered properties. The size-scaling effects of nanomagnetism often produce anomalies at reduced dimensions, which have been attributed to sample inhomogeneity, defects, or surface effects. The MSM imaging mode should provide insight on irregularities in nanoscale magnetic properties at the level of individual nanoparticles. The capabilities of the MSM imaging mode pushes beyond the 200 nm size detection threshold of MFM for characterization of magnetic particles as small as tens of nanometers. The information obtained from the MSM includes maps of the location of individual magnetic domains, which respond to the flux of an AC generated electromagnetic field as well as spectra of the characteristic resonance frequencies of the vibrating nanomaterials. Future directions will be to use the force measurement capabilities of an AFM probe to directly measure the magnetic response of the nanoparticles. By applying successively higher forces to the AFM probe, the vibration of the nanostructure can be halted. This will be compared as a function of applied AC field strength and as a function of the dimensions of individual nanostructures.

7.5 Conclusion

A different AFM imaging strategy is applied for magnetic sample modulation (MSM), which requires nonmagnetic tips to detect the vibration of magnetic nanomaterials. A soft, non-magnetic cantilever is used to detect motion and vibrational response rather than directly measuring magnetic forces. The information acquired from MSM images include the distribution of individual magnetic domains, which respond to the flux of an AC generated magnetic field, as well as spectra of the characteristic resonance frequencies of the vibrating nanomaterials. Analysis of the amplitude response of the AFM probe demonstrates that the magnitude of the vibration increases linearly with increasing size for iron oxide nanostructures, for the size range from 38 to 77 nm. The new approach for MSM imaging may become an important technique among the growing arsenal of AFM characterizations applied for investigating properties of nanomaterials.

CHAPTER 8. INDIRECT MODULATION OF NON-MAGNETIC PROBES FOR FORCE MODULATION ATOMIC FORCE MICROSCOPY

8.1 Introduction

Mechanical properties such as the elastic compliance and viscoelastic behavior of thin films and surface structures have been investigated by force modulation atomic force microscopy (FM-AFM) using a variety of different instrument configurations.[227, 311, 312] Using FM-AFM, images which map changes in the phase and amplitude of the tip oscillation can sensitively distinguish differences in the local elastic properties of surfaces.[228, 291, 311, 313-318] Dynamic AFM imaging modes such as FM-AFM are also beneficial for imaging soft materials, (e.g. biological surfaces) with greatly reduced forces to prevent damage to samples.[11, 319-321]

For a typical instrument configuration for FM-AFM, either the tip or sample is driven to vibrate by applying a sinusoidal voltage with controlled frequency and amplitude to a piezoceramic actuator.[131, 292, 293, 322] The periodic oscillation leads to a modulation of the force between the tip and sample, and the viscoelastic properties of the surface influence the tip deflection and motion. For locating resonance frequencies of the tip-sample contact, the amplitude and the phase changes are observed to be highly frequency-dependent.[227] The in-phase amplitude of the harmonic response is a function of elasticity, whereas the viscosity changes induce a phase shift.[11] For FM-AFM, a periodic modulation is applied to the cantilever in the z-direction, while the tip is scanned in direct contact with the sample. Such experiments are typically conducted at selected resonant frequencies and oscillation amplitudes. Positional feedback for dynamic scanning force microscopy (SFM) can be accomplished with the configuration typically used for topographic imaging with contact mode. The amplitude of the bending of the cantilever caused

---

Reproduced with permission from the American Chemical Society.

by interactions of the tip and sample are recorded by a photodetector. The modulation amplitude of the deflection is larger when the tip interacts with hard surface regions than when it interacts with softer regions of the surface. Contact with softer materials will cause the cantilever to oscillate at reduced amplitude and a different phase.[11, 291, 311, 314] During imaging, the amplitude and phase response of the cantilever are detected by a lock-in amplifier and recorded as a function of the tip position for surface mapping. Differences between the measured amplitude and phase versus the periodic function of the driving AC signal are used to generate digital images of changes in surface elastic properties.

Different strategies have been developed to drive the oscillation of tips for FM-AFM, with inherent advantages and disadvantages. For scanners with the tip mounted directly on the piezotube, an AC waveform can be applied directly to the piezo segments which drive the z position of the sample.[322] Alternatively, the tip can be mounted on a small piezoceramic chip to directly drive the tip vibration.[323] An external AC electromagnetic field can be used to drive the motion of an AFM tip for which a thin film of magnetic material is applied to the top side of the probe.[270-273, 324, 325] A general disadvantage when using magnetically coated cantilevers is that the magnetic strength of metal coating decreases with time, and the cantilevers need to be re-magnetized before use. Also, the magnetic coating often peels off over time, limiting the shelf-life of the coated AFM probes.

In this chapter, an alternate instrument configuration for force modulation AFM will be described, which will be referred to as indirect magnetic modulation (IMM). The operating principle is based on using an external AC electromagnetic field to oscillate the tip holder assembly or nosecone of the scanner, which indirectly drives the vibration of non-magnetic

cantilevers. Our goals are to evaluate and test the capabilities of the IMM instrument configuration, using designed test platforms of nanostructures prepared by particle lithography combined with vapor deposition of organosilane SAMs.[36] Silane self-assembled monolayers (SAMs) on solid substrates provide a model system for investigations of surface mechanical properties. Proof-of-concept results will be presented with FM-AFM, to assess the reproducibility and applicability of the IMM instrument set-up for characterizing designed test platforms of nanostructures of organosilane SAMs.

8.2 Materials and Methods

8.2.1 Materials and Reagents

2-Methoxy(polyethyleneoxy)propyl trichlorosilane (PEG-silane) and octadecyltrichlorosilane (OTS) were purchased from Gelest (Morrisville, PA) and used without further purification. Ethanol (ACS grade) was acquired from Pharmco (Aaper, TX). Certified particle size standards of polystyrene latex were obtained from Duke Scientific (Palo Alto, CA). Double-side polished silicon(111) wafers doped with boron were used as substrates (Virginia Semiconductor Inc., Fredericksburg, VA). Silicon substrates were cleaned with sulfuric acid (96%, EMD Chemical Inc., Gibbstown, NJ) and hydrogen peroxide (30%, Sigma-Aldrich). Ethanol, toluene (reagent grade, EMD Chemical Inc., Gibbstown, NJ) and deionized water (18 MΩ·cm, Milli-Q, Millipore, Bedford, MA) was used for rinsing samples.

8.2.2 Substrate Preparation

Pieces of silicon wafers (1×1 cm^2) were cleaned by immersion for 1 h in a mixture of sulfuric acid and hydrogen peroxide at a 3:1 v/v ratio (Piranha solution). Piranha solution is highly corrosive and should be handled with care. Silicon substrates were then rinsed with deionized water and dried in air.

106

8.2.3 Preparation of Test Platforms

Particle lithography with latex mesoparticles can be accomplished with vapor deposition of organosilanes to generate well-ordered hexagonal arrays of nanopatterns on silicon(111). The well-defined arrays of nanostructures produced by particle lithography provide precise reproducible dimensions for multiple successive measurements. The detailed steps for fabricating test platforms of organosilanes using particle lithography were previously reported.[36] First, solutions of latex particles were washed twice with deionized water by centrifugation, to remove contaminants such as charge stabilizers or surfactants. A solid pellet formed after centrifuging latex suspensions for 15 min at 14000 rpm. The supernatant containing contaminants was decanted, and the pellets were then resuspended in deionized water. Aqueous solutions containing monodisperse latex spheres (300 nm) were deposited on clean silicon substrates and then dried in air. During the drying step, capillary forces from the evaporation of water draw the latex spheres together to form organized crystalline layers on silicon surfaces. To produce nanopatterns, the substrates with latex films were used as evaporative masks placed within a sealed vessel containing 300 μL of organosilanes. The vessel was placed in an oven at 70 °C (ambient pressure) and heated to generate a vapor. Silane patterns were produced after 8 h exposure to organosilane vapor. The mask of latex particles was removed completely by successively rinsing the surface in ethanol and deionized water for 15 min with sonication. An example topograph acquired in air suing contact-mode AFM is presented (Figure 8.1A) for a view of 20 nanopatterns of PEG-silane within a $1.5 \times 1.5 \ \mu m^2$ area, which would scale to an estimated density of 10^8 nanostructures per square centimeter. The geometries of the rings are uniform and regular, achieving nanometer precision. The height of PEG-silane nanopatterns

measures 6.8 ± 0.4 nm with the average periodicity of 311 ± 8 nm (Figure 7.1B) which matches

closely with the diameter of the latex mask (300 ± 6 nm).
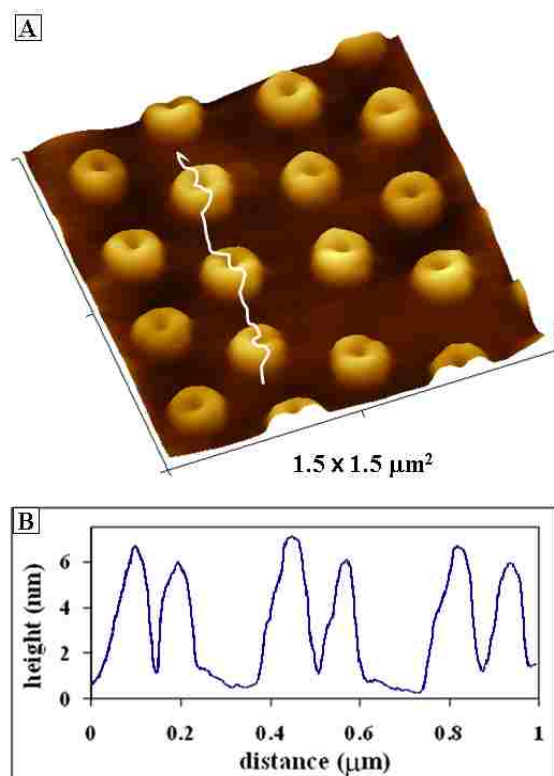
Figure 8.1 Rings of PEG-terminated silane produced with 300 nm latex masks: (A) three-dimensional AFM topograph acquired in air using contact-mode AFM; (B) corresponding cursor profile for the line in panel A.

8.2.4 Scanning Force Microscopy

An Agilent 5500 SFM equipped with Picoscan v5.3.3 software (Agilent Technologies, Tempe, AZ) was used for these investigations. Digital images were processed using Gwyddion (version 2.9) open source software, which is freely available on the Internet and supported by the Czech Metrology Institute.[138] A magnetic AC mode (MAC-mode) sample plate was used to generate an external AC electromagnetic field for IMM. An Agilent 5500 AFM multipurpose scanner with a scanning area of 11 x 11 μm^2 was used for imaging, with interchangeable nosecones. The scanner has a scanning tip configuration, which incorporates interchangeable

108

nose-cones for various imaging modes. For example, with current imaging a preamp is integrated within the nose cone for sensing current, the AC tapping-mode nose cone design has a piezoceramic chip to actuate an AFM tip; the "top-MAC" mode has a solenoid built into the nose cone. The PI's group has found that the nose-cone assemblies contain ferromagnetic metal components. Thus, when a magnetic field is applied by the solenoid within the sample stage, the entire tip holder assembly (nosecone) for the AFM tip is driven to vibrate. This indirect mode of tip vibration provides a means to accomplish dynamic modes of AFM imaging, and has particular advantages for acquiring FM-AFM images. The scanner was operated with open-loop feedback control for continuous imaging in contact mode. Silicon cantilevers with force constants of 0.2 N m^{-1} and a resonance frequency of 12 kHz were used for contact mode and IMM imaging in Figures 8.3 and 3-5. (SICON, NanoScience Instruments, Phoenix, AZ). Silicon nitride cantilevers with force constants of 0.1 N m^{-1} and resonance frequency of 26 kHz were used to test the reproducibility of IMM imaging in Figure 8.6. (MSCT-AUHW, Veeco Probes, Santa Barbara, CA).

8.2.5 Indirect Magnetic Modulation (IMM)

A MAC-mode sample plate was used for IMM imaging, which contains a wire coil solenoid underneath the sample plate (Figure 8.2). When an AC current is applied to the solenoid, an oscillating magnetic field is generated in the vicinity of the sample and tip-holder assembly. A non-magnetic tip is required for IMM imaging; the vibration of the nosecone assembly drives the motion of the AFM tip. The typical imaging procedure first involves acquiring conventional contact-mode images with the magnetic field turned off. Next, the same area of the surface is scanned again, with an applied AC electromagnetic field ranging from 0.05-0.4 T. A frequency sweep can be acquired to obtain dynamic information about tip-sample resonances. Because of

the nanoscale variability of tip geometries, a survey of the tip resonances must be accomplished for each experiment to locate frequencies for imaging. Three channels of data are acquired simultaneously, producing a topographic image and the corresponding amplitude and phase images. Channels of a lock-in amplifier are used to monitor changes in the phase and amplitude of the tip vibration, since slight changes in the periodic motion of the tip can be sensitively tracked and mapped with tip position.
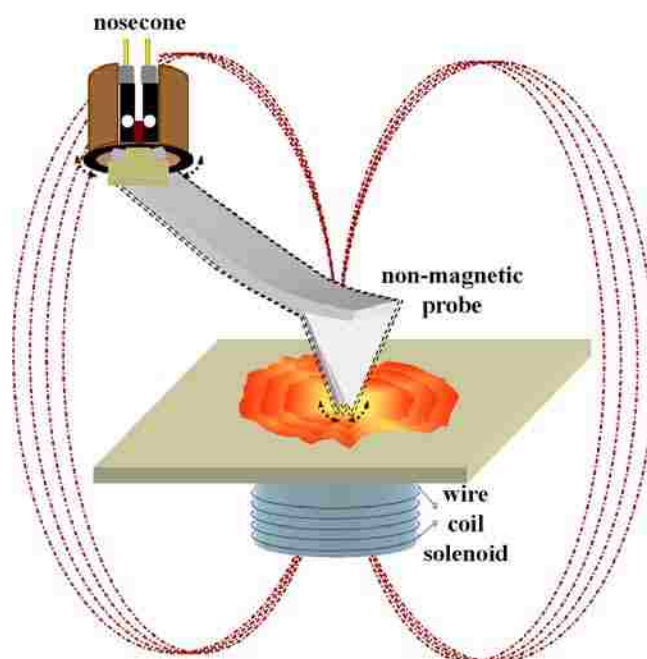
Figure 8.2 Operating principle for dynamic AFM with indirect magnetic modulation of the probe.

8.3 Results and Discussion

To evaluate the suitability of the IMM instrument configuration for FM-AFM, well-defined arrays of PEG-silane nanostructures were characterized, which furnish precise reproducible dimensions during multiple successive scans. Nanopatterns of PEG-silane are relatively soft in comparison to uncovered areas of the silicon(111) substrates, providing a practical soft organic material for mapping out differences in elastic compliance. Additionally, the masks of latex

mesoparticles used to prepare the nanopatterned test platforms can be scaled to very small dimensions to enable studies of elastic properties at a scale of tens of nanometers.

8.3.1 Frequency Spectra Using Indirect Magnetic Modulation (IMM)

The conventional approach for vibration with FM-AFM relies on actuation of either the tip or sample by applying an AC voltage to a piezoceramic element.[311, 326] For the examples to be presented with IMM, the instrument configuration used an AC electromagnetic field to indirectly drive the vibration of the tip holder assembly containing non-magnetic cantilevers. For IMM, parameters such as the frequencies for driving the cantilever motion were determined experimentally by comparing spectra of the vibrational resonances. Spectra were acquired when the tip was disengaged and also when placed in contact with the surface (Figure 8.3). When the tip is lifted away from the surface, the most prominent peak typically corresponds to the natural resonance of the free cantilever. However, for the example in Figure 8.3, the resonance frequency of the cantilever (12 kHz) is not apparent. As the tip is brought into contact with the surface, the amplitude of the resonance peaks are dampened and shifted to the left. When the tip is engaged, five prominent peaks are detected for tip-surface resonance frequencies, at 55, 104, 158, 214 and 322 kHz (red curve in Figure 8.3). Note that one of the resonances (214 kHz) does not have a corresponding peak when the tip was disengaged from the surface, and thus originates from tip-sample contact. Comparing the heights of the peaks, the order of the magnitude from low to high response correspond to 104, 214, 322, 55 and 158 kHz, respectively.

Unlike direct modulation modes, the resonance of the tip was not apparent for the cantilever, instead there were five peaks observed when the tip and sample are brought into contact. Additional peaks can arise from overtones, resonances of the mechanical system, as well as influences of the tip-sample contact. Since the entire tip-holder assembly is driven to vibrate, the

frequency spectra indicate the natural resonances of the larger assembly as well as background vibration of the sample stage. When selecting frequencies for data acquisition, typically one or more of the tip-sample contact resonances are chosen to drive the tip oscillation.
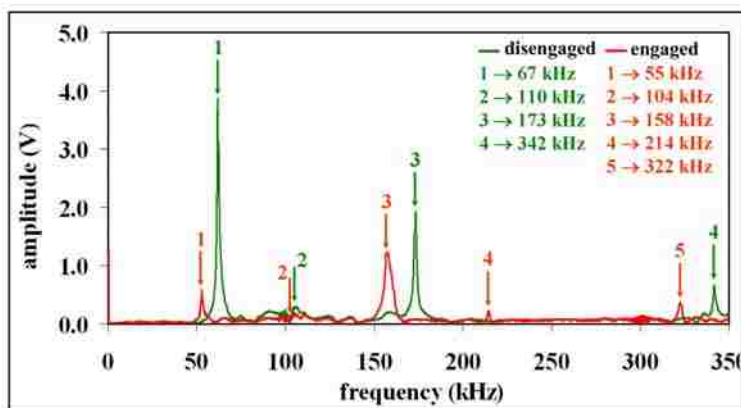
Figure 8.3 Response of an AFM probe to indirect magnetic modulation.

8.3.2 Images Acquired with IMM at Different Driving Frequencies

Using IMM, images of PEG-silane nanopatterns (3.5×3.5 μm^2 frames) were acquired at the frequencies of the five peaks detected when the tip was engaged with the surface (Figure 8.4). The selected sample and area were imaged successively with the same tip and force setpoint (0.84 nN), with an average magnetic field strength of 0.16 T. The images for all of the various frequencies (Figures 8.4A-8.4E) display nanostructured rings of PEG-silane nanopatterns on silicon(111) which can be distinguished in topography, amplitude and phase frames. There are several missing patterns within the field of view, which adventitiously provide a landmark for *in situ* imaging. The same uncovered areas are present in each series of images, providing a frame of reference. For the topography images, the bright contrast corresponds to the taller structures and the dark areas distinguish the bare substrate. The color scales for height changes in the topography channels remain unchanged despite changes in the driving frequency with IMM.

112

However, significant changes in the magnitude of the color scales are apparent for the amplitude and phase channels, according to the magnitude of the response at the selected frequencies.

What ultimately determines whether features of the surface are light or dark for phase and amplitude images results from several factors, including the choice of the driving frequency and amplitude[230, 313, 327, 328] and whether the tip is operated in the attractive or repulsive regime.[230, 329, 330] The amplitude images display changes for the vibrational amplitude as the motion of the tip is enhanced or diminished when it interacts with the sample, and thus correlates with differences in the hardness/softness of materials. The phase images are more complex to interpret, displaying changes in phase lag compared to the driving signal. Phase images are often extremely sensitive for mapping surface features that are indistinguishable in the topography channels, but do not necessarily originate from differences in elastic response. The circular areas inside the PEG-silane rings are uncovered areas of substrate, approximately 100 nm in diameter. For all of the phase and amplitude images displayed in Figure 4, the color of the central areas within the rings matches the substrate, evidencing nanoscale sensitivity for IMM imaging.

For the images in phase or amplitude columns of Figure 8.4, the contrast for the ring elements of arrays is observed to change according to the selected frequency parameters. The smallest peak from the spectra of Figure 8.3 (104 kHz) provided the weakest amplitude (94 mV) and phase response (0.014 V), for the images of Figure 8.4B. The remaining peaks provided excellent sensitivity, and do not scale predictively with the magnitude of the response from the spectra of Figure 8.3. The phase and amplitude images with the greatest sensitivity (according to the magnitude of the color scales) were observed at 322 kHz, which exhibited an intermediate peak height in the frequency spectra. An interesting effect is apparent when comparing the amplitude and phase images at different frequencies. All of the amplitude images indicate a dark

color for the rings, and a bright color for the substrate except the data acquired at 214 kHz. Similar flips in contrast are apparent at 104 kHz and 158 kHz when comparing the phase channels.
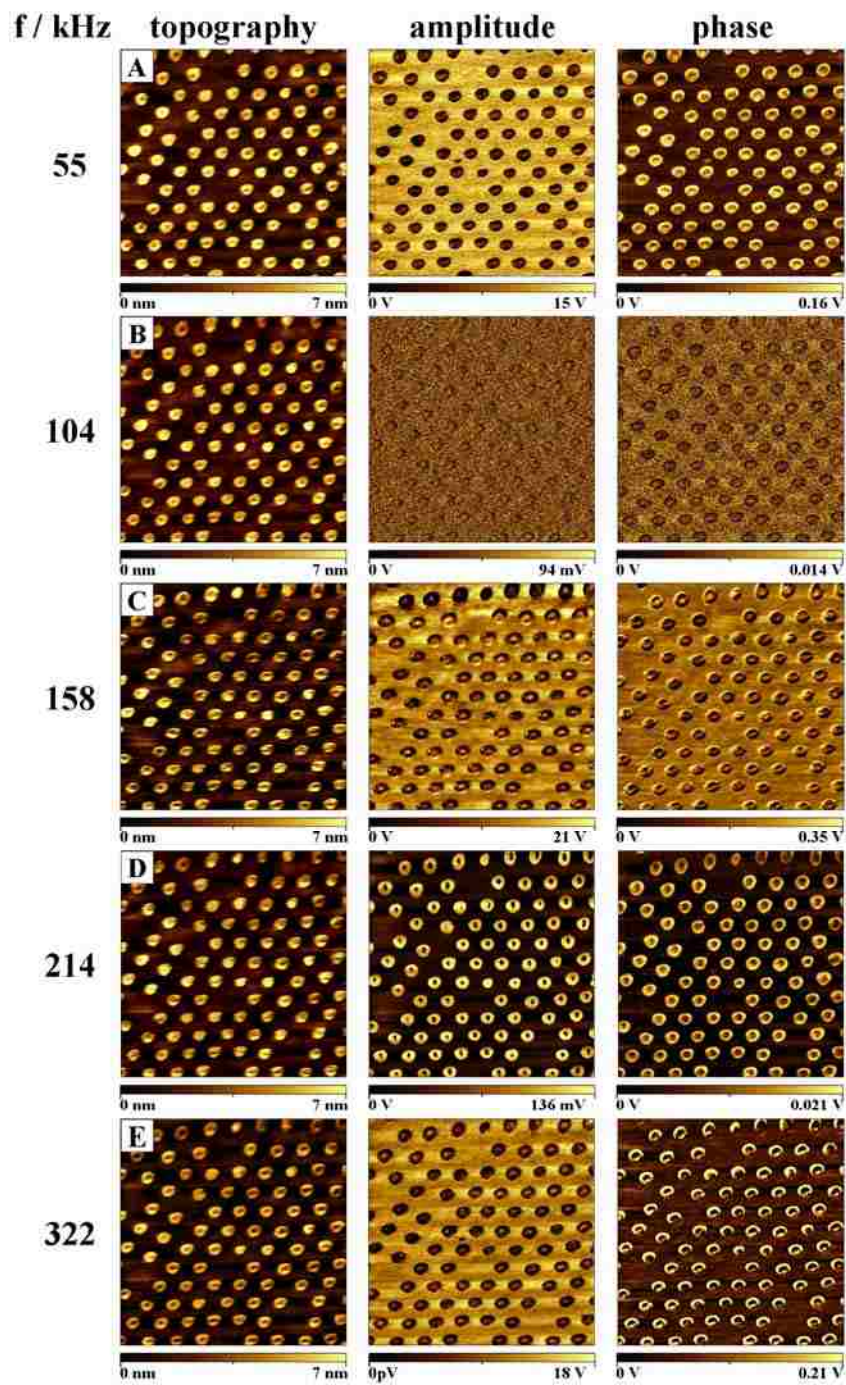
Figure 8.4 Images of PEG-silane nanopatterns acquired with IMM at frequencies of (A) 55, (B) 104, (C) 158, (D) 214, and (E) 322 kHz.

The contrast changes for the series of images in Figure 8.4 result from combined effects of tip-surface interactions as well as the applied amplitude and frequency parameters. The IMM images in Figure 8.4 reveal contrast reversals at certain resonances as the tip is operated at the interface of the repulsive and attractive regimes of contact. The silicon substrate is viewed to be harder (dark color) than the PEG-silane nanostructures for both the phase and amplitude channels only at 214 kHz. All of the remaining frequencies indicate color differences which do not correlate with the hardness/softness of the sample. Recall that the 214 kHz peak originated when the tip was brought into contact with the sample, and was not present when the tip was disengaged.

The strong dependence of the elasticity images on the driving frequency observed in Figure 8.4 highlights the complexity of the dynamics of the tip-surface contact. All of the resonance peaks of the free cantilever provided mixed results for evaluating whether the substrate or nanostructures were softer. For example, at 55 kHz, the amplitude channels display dark rings against a bright surface, whereas the corresponding phase image evidences light rings on a dark surface. With this set of experiments, to distinguish the softness of the sample the optimal contrast was achieved at a resonance frequency which was independent of the tip oscillation when it was disengaged. Contrast reversals have been observed and described previously for nanostructured monolayers of octadecyltriethoxysilane prepared on mica(0001).[131] Jourdan et al. suggest that the thin film of water that is present under ambient conditions forms a capillary neck at the contract, which influences the tip motion.[131] Liquid media damp the oscillating motion of the cantilever.[229, 313, 331-334]

A protocol for ramping the driving frequency was developed to view the successive changes within a single image (Figure 8.5). Seven frequencies were selected for this example, including

five resonances from tip-surface contact (55, 104, 158, 214 and 322 kHz) and two randomly selected resonances from background noise (65 and 137 kHz). After rastering across an area of 0.5 μm, the driving frequency was changed without halting/interrupting data acquisition. This protocol enabled a side-by-side comparison of the changes in elastic response within a single frame, evaluated simultaneously against a common response scale.
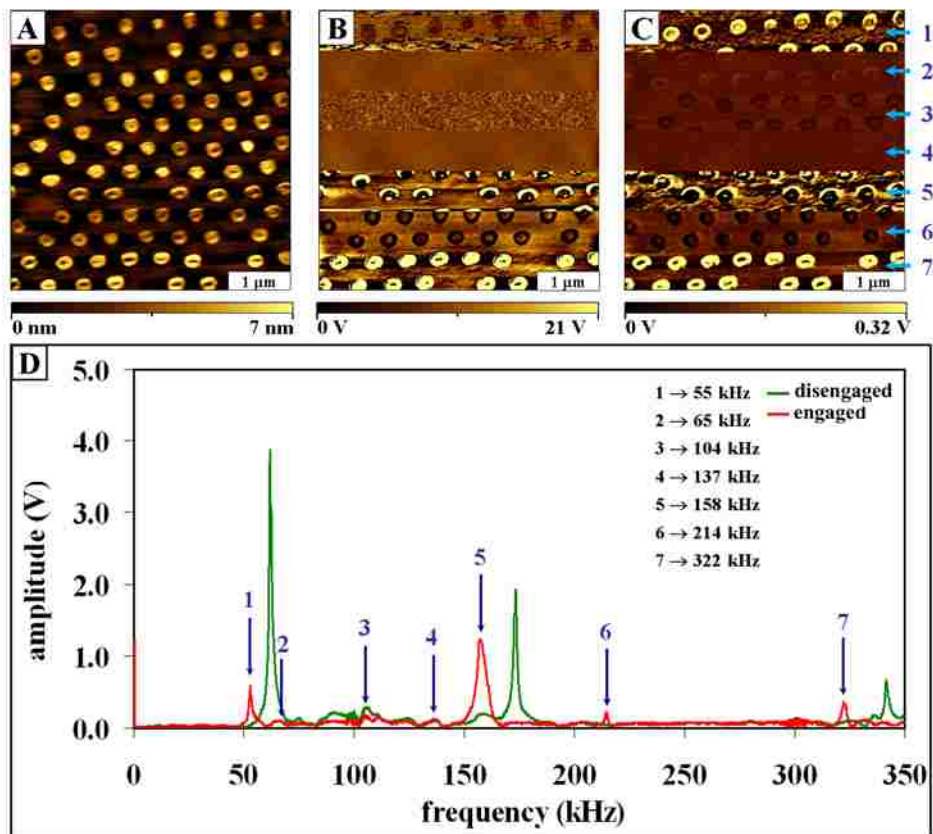
Figure 8.5 Dynamic IMM images of PEG-silane nanopatterns acquired with different frequencies in a single scan: (A) topography image, (B) amplitude image, (C) phase image, and (D) frequency plot.

Prominent changes are not observed within the topographic frame of Figure 8.5A, as the frequency is successively ramped during the scan; however there are subtle changes for nanoscale resolution. The pore structures within the rings provide a reference structure for comparing resolution, and the holes are more clearly distinguishable at 214 kHz and 322 kHz.

116

Enhancement of topographic contrast at certain frequencies has previously been reported as a mechanism for imaging soft and sticky surfaces. On the other hand, for the simultaneously acquired phase and amplitude frames (Figures 8.5B and 8.5C) changes in contrast are clearly apparent as the frequency is ramped. Sharp changes in contrast are apparent immediately when the driving frequency is changed, providing clear linear boundaries in the phase and amplitude frames. The changes for driving frequencies images do not evidence stretching, elongation, or distortion of the ring geometries when imaging in air. This suggests that very little time (< 1 second) is needed for the tip motion to equilibrate with changes in the rhythm of IMM driven oscillation. The color scale variations for the frequency sweep experiment mostly match the trends of Figure 8.4, except at the highest frequencies. When scanning at the four resonances from tip-surface contact (number 1, 3, 5 and 7 in Figure 8.5), the contrast in amplitude and phase images are the same as those presented in Figure 8.4. For the area scanned using background frequencies without resonance peaks (65 kHz and 135 kHz), the corresponding signal levels of the amplitude and phase channels are much weaker than those observed at peak resonances. At higher frequencies, the resonance peaks are narrower, thus the reproducibility of tuning in the resonance motion is less precise. A small change in the forward or reverse position of the resonance peak can change the tip-sample contact situation to a repulsive or attractive regime within a narrowly defined range of frequencies.[230]

Imaging with FM-AFM is highly frequency dependent, a slight change in the selection of the resonance peak has been demonstrated to greatly influence the contrast of phase and amplitude images.[230, 327, 328] The effect of making small changes in the peak position near the resonance frequency was investigated for the IMM experiment presented in Figure 8.6. Three closely spaced frequencies were selected at locations before the resonance frequency at 85 kHz

(Figure 8.6A), at the resonance frequency of 94 kHz (Figure 8.6B) and post-resonance at 103 kHz (Figure 8.6C). A side-by-side comparison is displayed in Figure 8.6D, by changing the selected frequencies during data capture of a single frame. The contrast in amplitude images is shown to depend on the intensity of chosen drive frequencies. The image acquired for the on-resonance frequency exhibited a stronger amplitude signal of 2.1 V in Figure 8.6B, whereas the smaller intensity peaks at 85 and 103 kHz resulted in weaker amplitude responses of 1.1 V and 1.2 V, respectively for Figures 8.6A and 8.6C. This effect is reproduced in the frequency sweep experiment of Figure 8.6D. A reversal in the contrast of the amplitude and phase channels is detected when the driving frequency is precisely on resonance compared to near resonance peaks. When the driving frequency is off-resonance, the magnitude of the response and contrast differences are diminished. A spectral profile of the selected resonance peaks are displayed in Figure 8.6E. When the tip makes contact with the surface, the tallest resonance peak is relatively broader and shifted left as compared to the profile when the tip was disengaged (Figure 8.6E).

When choosing to drive the tip at different positions near the resonance peak, the tip-sample contact situation changes to either a repulsive or attractive regime for tip-surface interactions, which produces corresponding changes in the contrast for amplitude and phase images.[230] Using well-defined test structures provides a way to assess and select the optimal resonance for FM-AFM. For example, in Figure 8.6, the silane nanostructures should be softer than the silicon substrate, which would produce a corresponding bright contrast for the rings. This is clearly observed for both the phase and amplitude channels with the images acquired precisely on-resonance in Figure 8.6B. At non-resonance frequencies or nearby resonances, the contrast for OTS rings is reversed, due to the interplay of attractive and repulsive interactions of the tip and surface.
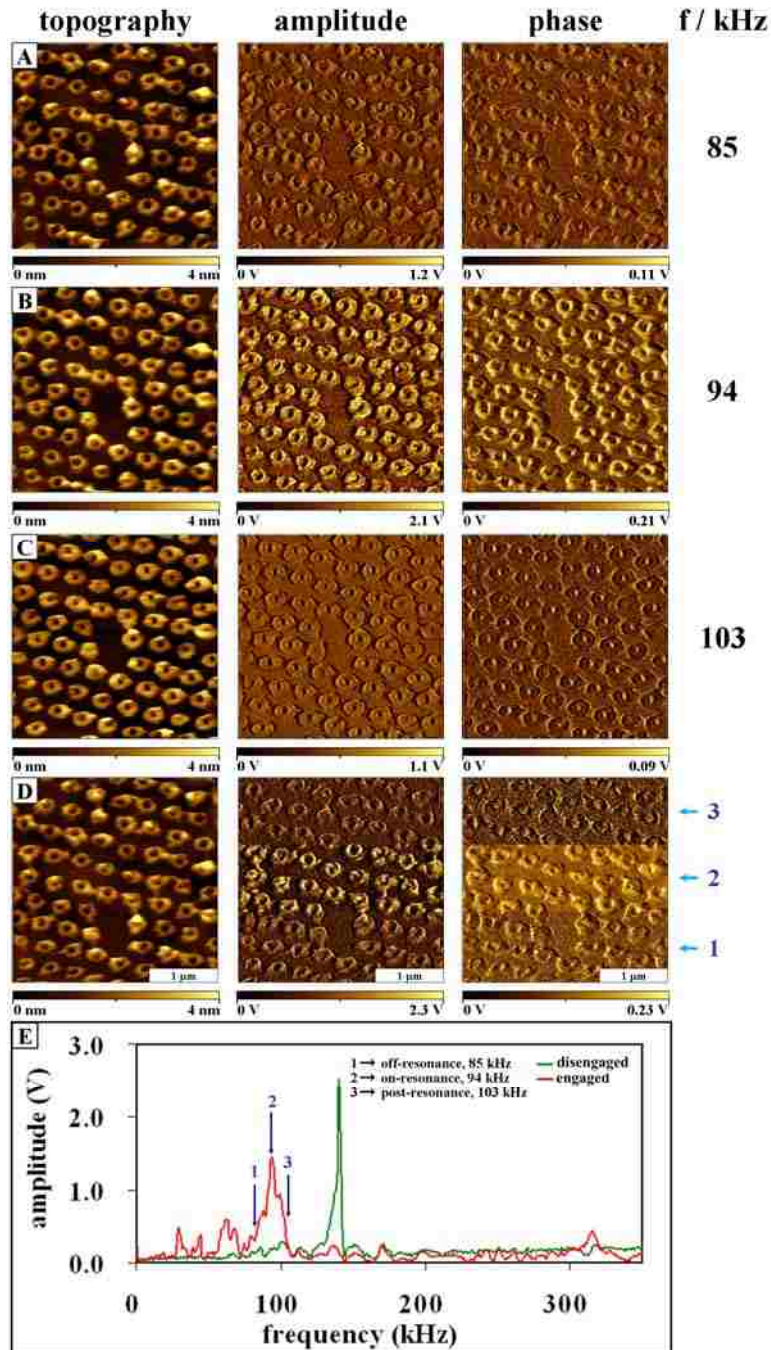
Figure 8.6 Frequency-dependent changes for amplitude and phase images at peak positions at or near resonance: (A) pre-resonance, 85 kHz, (B) on-resonance, 94 kHz, and (C) post-resonance, 103 kHz. (D) Successive changes captured within a single frame for the three frequencies. (E) Comparison of frequency spectra when the tip is engaged or disengaged from the surface.

Phase and amplitude images can be used to sensitively map differences in the elastic response of nanopatterned samples, however the selection of optimal parameters such as the

119

driving frequency and modulation amplitude remain a complicated issue. Indirect modulation is well-suited for characterizations with soft cantilevers (0.1 - 0.2 N m^{-1}) at low forces (<1 nN), to provide non-destructive imaging conditions. The instrument configuration for IMM provides a means to clarify whether the peak resonances originate from motion of the vibrating tip holder or from vibrations originating at the tip-sample contact. Choices for imaging modes, spring constants of the cantilevers, imaging media as well as the nature of the sample surface will influence the experimental decisions for selecting the most suitable driving frequency and amplitudes for dynamic SFM.

8.4 Conclusions

An IMM instrument configuration was successfully demonstrated for FM-AFM under ambient conditions, based on indirect modulation of a non-magnetic tip. The instrument set-up employs a soft, cantilever which does not respond directly to an externally applied magnetic field; instead the tip motion is driven indirectly by the vibration of the sample holder assembly in response to the flux of an externally applied AC electromagnetic field. Using IMM, frequency-dependent changes for the contrast of phase and amplitude images were demonstrated for nanopatterned test platforms of organosilane rings for driving frequencies up to 350 kHz. For phase images, a small change in the peak position (forward or reverse) of the selected resonance peak can invert the image contrast expected for phase and amplitude images. When the selected driving frequency is precisely on resonance, the amplitude and phase images correlate well with predicted differences in softness for designed test structures of organosilanes. Future investigations will evaluate the capabilities of IMM for imaging in liquid media, as well for a broader range of driving frequencies and amplitudes.

CHAPTER 9. CONCLUSIONS AND FUTURE PROSPECTS

New methods for nanofabrication based on particle lithography were developed and applied to generate nanostructures on surfaces. Monodisperse spheres self-assemble on flat surfaces into periodic structures with designed dimensions and interparticle spacing, which can then be used as structural templates or masks to guide the deposition of nanomaterials. Geometry, dimension and size of nanostructures are tunable by changing the size of particles. Particle lithography provides the advantages of high throughput, and reproducibility. Well-defined surfaces with desired functionalities and geometries can be fabricated using particle lithography and successive chemical reactions. The position and spatial distribution of nanomaterials can be regulated at the nanoscale with mesoparticle masks/templates prepared by particle lithography. The spatial selectivity provided by particle lithography will be used for further chemical reactions to adsorb different materials such as proteins, metals and nanoparticles. Well-defined nanostructures will provide precise reproducible dimensions for investigations of surface properties and furnish test platforms that are suitable for successive characterizations with SPM to obtain insight into size-dependent properties. The results presented in this dissertation demonstrate the combination of nanofabrication and AFM to investigate structure/property relationships and measure size-dependent nanoscale properties. Particle lithography possesses the capability of designing well-defined surfaces with exquisitely uniform nanostructures and tailorable surface chemistry. Designed nanostructures with desirable functionalities facilitate development and evaluation for new AFM imaging modes. Magnetic sample modulation enables to identify the location of iron oxide nanostructures. The elastic compliance of organosilane nanopatterns can be investigated using indirect magnetic modulation.

9.1 Arrays of Protein Nanopatterns Produced Using Particle Lithography

Particle lithography was applied for high-throughput patterning to generate millions of protein nanostructures on surfaces. The model proteins bovine serum albumin and staphylococcal protein A were patterned on the surface of mica indicating the generality and reproducibility of the particle lithography.[31, 32] Conventional bench chemistry steps of mixing, centrifuging, drying and rinsing facilitate particle lithography to provide exquisite control for the surface coverage and periodicity of protein nanopatterns. The periodicity and diameter of the protein nanostructures are tunable by selecting the sizes of spheres. The morphologies of nanopatterns can be precisely regulated with the protein-to-particle ratios, providing exquisite uniformity of the array elements. Particle lithography with a low ratio of proteins to mesospheres produced ring-shaped patterns with a single layer of proteins. At higher protein-to-particle ratio, a monolayer of proteins with uncovered pore structures was produced. Particle lithography is a highly reproducible and robust method for patterning proteins, and serves as an excellent starting point for continuing to develop more complex bioassays. Arrays of protein nanostructures can enhance binding efficacy to target molecules and improve sensitivity of detection for further advancing biosensor technology.

9.2 Particle Lithography Combined with Vapor Deposition of Organosilanes

Method of particle lithography combined with vapor deposition was developed to pattern organosilanes on various surfaces such as, mica, silicon and gold.[36, 37] For organosilanes to bind to substrates, nanoscopic amounts of water are needed to initiate surface hydrolysis. Latex masks used for particle lithography enable to control and direct the placement of nanoscopic residues of water for hydrosilation. Drying intervals determine the nanoscopic amounts of water present on surfaces. Differences in nanopattern morphologies of organosilanes depend on various drying

conditions. For latex masks that have been dried briefly, water is distributed homogeneously throughout areas of the surface to enable molecular self-assembly of a silane thin film covering interstitial areas between mesoparticles, resulting in the formation of pore-shaped morphology. When colloidal masks are dried under ambient conditions for longer intervals, tiny residues of water persist to form a circular meniscus in areas surrounding the base of latex spheres. As silane vapors are introduced, molecules bind to any areas of the surface with a circular meniscus between latex spheres. The circular shapes of the nanostructures correspond to the areas with water residues near the base of the latex mesoparticles.

9.3 Metal Nanostructures Fabricated by Selective Deposition on Nanopatterned Surfaces

Surfaces with well-defined nanopatterns provide a platform for further successive steps of chemical reactions. Nanopatterned surfaces with different functionalized organosilanes can provide exquisite surface selectivity to precisely define areas for the deposition of metals. Arrays of iron oxide nanostructures were fabricated using electroless deposition onto nanopatterned surfaces produced with particle lithography and organosilanes.[39] The head groups of organosilanes enable exquisite selectivity for deposition of iron oxide. The geometry of nanopattern provides spatial confinement to localize iron oxide on the surfaces. Arrays of iron oxide nanostructures conform precisely to the selected areas of patterned organosilanes with reproducible and near-perfect nanoscale geometries. The periodicity of the iron oxide nanostructures is determined by the diameter of mesospheres used for particle lithography. Metal contacts formed on organosilane nanopatterns produced by particle lithography combined with vapor deposition may be suitable for SPM investigations of molecular conductance and nanomagnetism, towards development of nanoscale electrical heterojunctions and molecular electronics.

9.4 Detection of Magnetic Response Using Magnetic Sample Modulation AFM

New imaging strategies using atomic force microscopy were developed for mapping magnetic domains and elastic compliance at size regimes at nanoscale. Arrays of nanostructures possess tailorable size and spacing, which can be used as test platforms for new AFM imaging modes. A different AFM imaging strategy is applied for magnetic sample modulation, which requires nonmagnetic tips to detect the vibration of magnetic nanomaterials.[40] When an electromagnetic field is applied to arrays of iron oxide nanostructures, only iron oxide can be driven to vibrate, providing selective contrast for areas that are in motion. The AFM tip serves as a force and motion sensor for mapping the vibrational response of iron oxide nanostructures. Changes in the phase and amplitude images with and without an applied magnetic field are used to recognize iron oxide domains. The information acquired from MSM images includes the distribution of individual magnetic domains as well as spectra of the characteristic resonance frequencies of the vibrating nanomaterials. Analysis of the amplitude response of the AFM probe demonstrates that the magnitude of the vibration increases linearly with increasing size for iron oxide nanostructures. Future work for MSM will evaluate the size-dependent effects, studied in a range from superparamagnetism to regular bulk ferromagnetism.

9.5 Characterization of Elastic Compliance Using Indirect Magnetic Modulation

An AFM imaging mode based on the instrument configuration of indirect magnetic modulation was successfully demonstrated to investigate elastic response of organosilane nanostructures.[45] The instrument set-up employs a soft, non-magnetic cantilever which does not respond directly to an externally applied magnetic field. In IMM, a tip is driven to vibrate by the motion of a tip holder assembly which contains ferromagnetic materials. The entire tip assembly is induced to vibrate with the flux of an external ac electromagnetic field, supplied by a wire coil

solenoid placed underneath the sample plate. With the use of IMM, dynamic parameters of the driving frequencies and amplitude of the tip motion can be optimized to sensitively map the elastic response of samples. Frequency-dependent changes for the contrast of phase and amplitude images were relative to the driving resonance frequencies selected for nanopatterned test platforms of organosilane. A small change in the peak position of the selected resonance peak can invert the image contrast expected for phase and amplitude images. When the selected driving frequency is precisely on resonance, the amplitude and phase images correlate well with predicted differences in softness for designed test structures of organosilanes.

9.6 Future Prospectus

The results presented in this dissertation are foundation for further development of particle lithography to design well-defined surfaces with uniform nanostructures and tailorable surface chemistry. Engineered surfaces with well-defined functionalities produced using particle lithography with organosilanes can provide exquisite surface selectivity to precisely confine the adsorption of various nanomaterials. An example is presented in Figure 9.1 for selective adsorption of monolayer-protected clusters (MPCs) onto the nanopatterned surfaces with an organosilane. The steps include fabrication of organosilane nanopatterns on silicon substrates using vapor deposition through mesoparticles masks and deposition of silanol-terminated MPCs (Figure 9.1A). The methyl-terminated films of OTS provide a highly effective resist to prevent binding at boundary areas surrounding the circular areas of Si(111). Due to the strong affinity between silanol and silicon, the MPCs can adsorb selectively and uniformly at the regions surrounded with OTS, as demonstrated in the AFM images of Figures 9.1B and 9.1C. Within the $1 \times 1 \ \mu m^2$ area of Figure 9.1D, nine clusters of MPCs are apparent the 3-D zoom-in view.
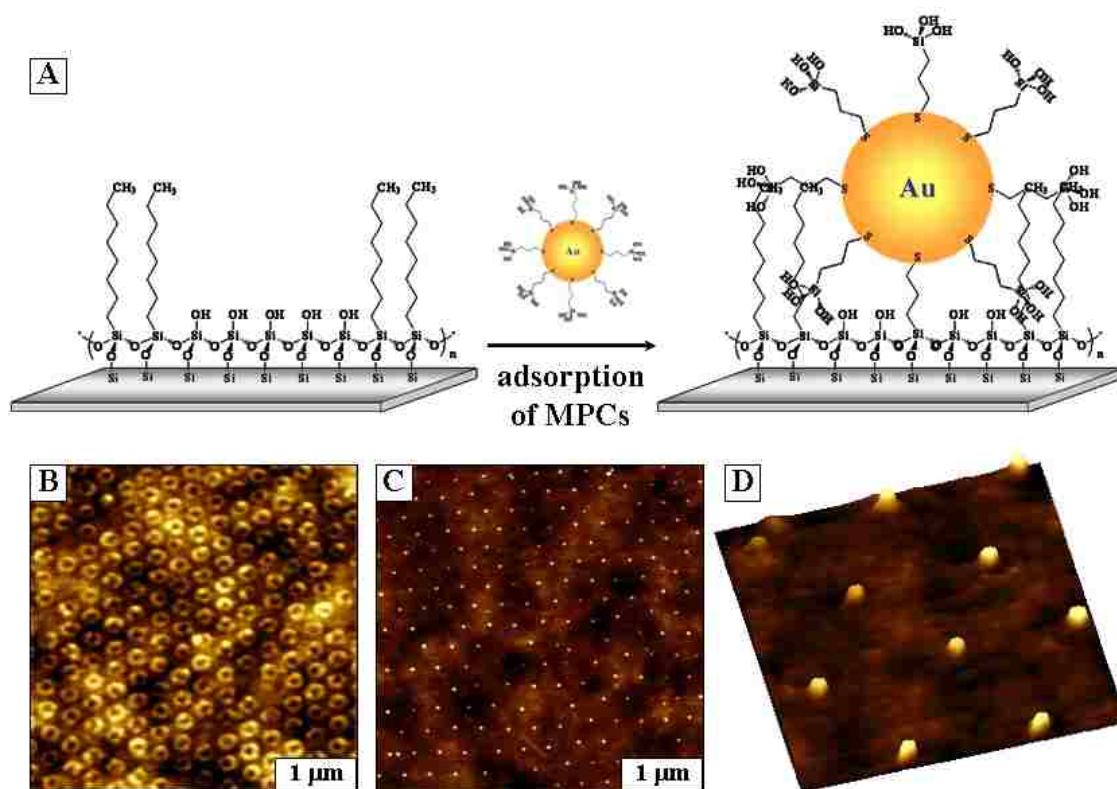
Figure 9.1 Selective adsorption of MPCs onto nanopatterns of organosilanes. (A) Fabrication procedure; (B) topography (4×4 μm^2) of OTS nanostructures fabricated using particle lithography with 300 nm latex particles; (C) topography (4×4 μm^2) of MPCs arrays produced using selective adsorption; (D) 3-D zoom-in view of MPCs arrays.

Instead of selective deposition of nanomaterials onto well-defined surface, the arrangement of nanomaterials can be directly guided with structural templates of monodisperse mesoparticles to generate 2D arrays of nanopatterns. The representative example in Figure 9.2 presents an approach of two-particle lithography to produce arrays of patterns of cobalt nanoparticles. For two-particle lithography, the silica mesoparticles serve as a solid structural template during conditions of ambient drying. As the liquid dries, cobalt nanoparticles assemble surrounding the base of silica spheres (Figure 9.2A). The resulting patterns of cobalt nanoparticle aggregates exhibit ring-shaped morphology that conforms to the shape of structural templates. The geometry and arrangement of the rings are viewed with AFM and SEM images in Figure

9.2B and 9.2C. The geometries of cobalt nanopatterns are highly symmetric and uniform. Two-particle lithography provides a viable approach for generating arrays of patterns of nanoparticles using simple steps of bench chemistry (e.g. centrifugation, drying, evaporation, rinsing).
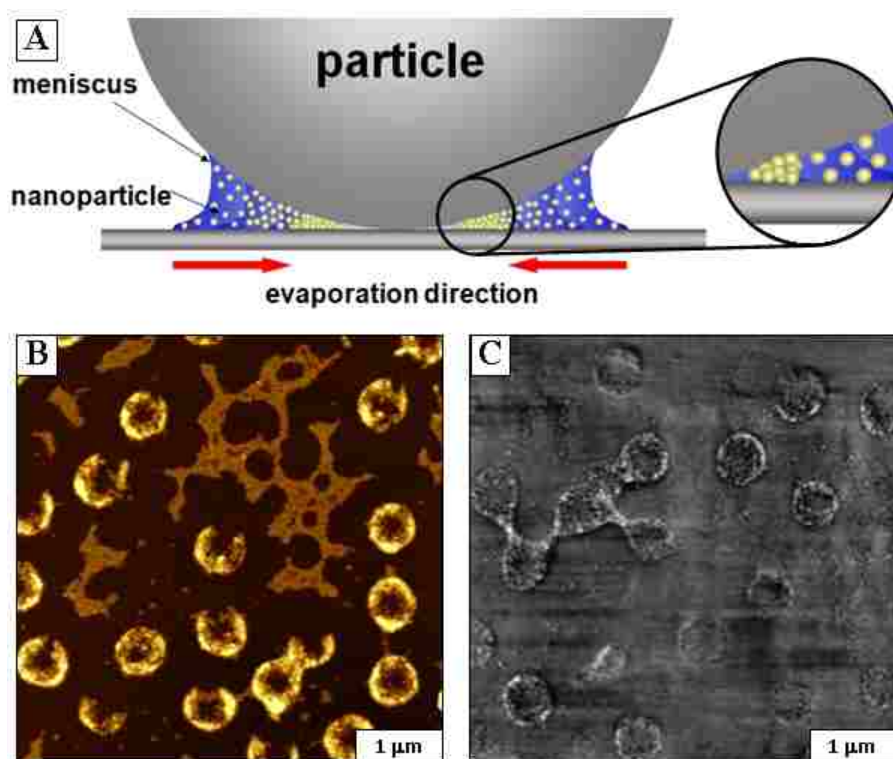
Figure 9.2 Ring-shaped structures of cobalt nanoparticles produce using structural templates of 500 nm silica particles. (A) overview for two-particle lithography; (B) contact mode AFM topography (5×5 μm^2); (C) SEM image (5×5 μm^2).

The emergence of nanoscience and nanotechnology depends on the ability to organize materials at the nanoscale so as to create designed functional assemblies that can display desirable properties with reproducibility. Nanomaterials exhibit quantized electrical and optical properties that can be advantageously exploited in the design of future nanodevices. Control of the relative position and orientation of the nanomaterials on the surfaces enables the development of well-defined molecular architectures. Research efforts have been invested in advancing nanofabrication capabilities which enable site-selective deposition of nanomaterials

onto designed surfaces. Patterned surfaces with controllable chemical functionality can be used to integrate various molecules into miniaturized devices with organized arrangements which will lead to develop molecular electronics and biological sensing systems. Ongoing research will focus on patterning nanomaterials to be test platforms for SPM investigation of size-dependent properties.

REFERENCES

1. Barth, J. V.; Costantini, G.; Kern, K., Engineering atomic and molecular nanostructures at surfaces. *Nature* **2005,** 437, (7059), 671-679.

2. Rosi, N. L.; Mirkin, C. A., Nanostructures in biodiagnostics. *Chemical Reviews* **2005,** 105, (4), 1547-1562.

3. Woodson, M.; Liu, J., Functional nanostructures from surface chemistry patterning. *Physical Chemistry Chemical Physics* **2007,** 9, (2), 207-225.

4. Gimzewski, J. K.; Joachim, C., Nanoscale science of single molecules using local probes. *Science* **1999,** 283, (5408), 1683-1688.

5. Link, S.; El-Sayed, M. A., Spectral properties and relaxation dynamics of surface plasmon electronic oscillations in gold and silver nanodots and nanorods. *Journal of Physical Chemistry B* **1999,** 103, (40), 8410-8426.

6. Cui, Y.; Wei, Q. Q.; Park, H. K.; Lieber, C. M., Nanowire nanosensors for highly sensitive and selective detection of biological and chemical species. *Science* **2001,** 293, (5533), 1289-1292.

7. Theobald, J. A.; Oxtoby, N. S.; Phillips, M. A.; Champness, N. R.; Beton, P. H., Controlling molecular deposition and layer structure with supramolecular surface assemblies. *Nature* **2003,** 424, (6952), 1029-1031.

8. Alivisatos, A. P., Semiconductor clusters, nanocrystals, and quantum dots. *Science* **1996,** 271, (5251), 933-937.

9. Cui, Y.; Lieber, C. M., Functional nanoscale electronic devices assembled using silicon nanowire building blocks. *Science* **2001,** 291, (5505), 851-853.

10. Lu, A. H.; Salabas, E. L.; Schuth, F., Magnetic nanoparticles: Synthesis, protection, functionalization, and application. *Angewandte Chemie-International Edition* **2007,** 46, (8), 1222-1244.

11. Radmacher, M.; Tillmann, R. W.; Fritz, M.; Gaub, H. E., From molecules to cells - Imaging soft samples with the atomic force microscope. *Science* **1992,** 257, (5078), 1900-1905.

12. Hansma, P. K.; Elings, V. B.; Marti, O.; Bracker, C. E., Scanning tunneling microscopy and atomic force microscopy - Application to biology and technology. *Science* **1988,** 242, (4876), 209-216.

13. Frisbie, C. D.; Rozsnyai, L. F.; Noy, A.; Wrighton, M. S.; Lieber, C. M., Functional-group imaging by chemical force microscopy. *Science* **1994,** 265, (5181), 2071-2074.

14. Kelley, T. W.; Granstrom, E. L.; Frisbie, C. D., Conducting probe atomic force microscopy: A characterization tool for molecular electronics. *Advanced Materials* **1999,** 11, (3), 261-264.

15. Dulcey, C. S.; Georger, J. H.; Krauthamer, V.; Stenger, D. A.; Fare, T. L.; Calvert, J. M., Deep UV photochemistry of chemisorbed monolayers - Patterned coplanar molecular assemblies. *Science* **1991,** 252, (5005), 551-554.

16. Xia, Y. N.; Mrksich, M.; Kim, E.; Whitesides, G. M., Microcontact printing of octadecylsiloxane on the surface of silicon dioxide and Its application in microfabrication. *Journal of the American Chemical Society* **1995,** 117, (37), 9576-9577.

17. Ivanisevic, A.; Mirkin, C. A., "Dip-Pen" nanolithography on semiconductor surfaces. *Journal of the American Chemical Society* **2001,** 123, (32), 7887-7889.

18. Wadu-Mesthrige, K.; Xu, S.; Amro, N. A.; Liu, G. Y., Fabrication and imaging of nanometer-sized protein patterns. *Langmuir* **1999,** 15, (25), 8580-8583.
19. Lee, K. B.; Park, S. J.; Mirkin, C. A.; Smith, J. C.; Mrksich, M., Protein nanoarrays generated by dip-pen nanolithography. *Science* **2002,** 295, (5560), 1702-1705.

20. Hoeppener, S.; Maoz, R.; Sagiv, J., Constructive microlithography: Electrochemical printing of monolayer template patterns extends constructive nanolithography to the micrometer-millimeter dimension range. *Nano Letters* **2003,** 3, (6), 761-767.

21. Gu, J. H.; Yam, C. M.; Li, S.; Cai, C. Z., Nanometric protein arrays on protein-resistant monolayers on silicon surfaces. *Journal of the American Chemical Society* **2004,** 126, (26), 8098-8099.
22. Haynes, C. L.; Van Duyne, R. P., Nanosphere lithography: A versatile nanofabrication tool for studies of size-dependent nanoparticle optics. *Journal of Physical Chemistry B* **2001,** 105, (24), 5599-5611.

23. Xia, Y. N.; Gates, B.; Yin, Y. D.; Lu, Y., Monodispersed colloidal spheres: Old materials with new applications. *Advanced Materials* **2000,** 12, (10), 693-713.

24. Jiang, P.; Bertone, J. F.; Colvin, V. L., A lost-wax approach to monodisperse colloids and their crystals. *Science* **2001,** 291, (5503), 453-457.

25. Kuo, C. W.; Shiu, J. Y.; Chen, P. L.; Somorjai, G. A., Fabrication of size-tunable large-area periodic silicon nanopillar arrays with sub-10-nm resolution. *Journal of Physical Chemistry B* **2003,** 107, (37), 9950-9953.

26. Meng, Q. B.; Fu, C. H.; Einaga, Y.; Gu, Z. Z.; Fujishima, A.; Sato, O., Assembly of highly ordered three-dimensional porous structure with nanocrystalline TiO2 semiconductors. *Chemistry of Materials* **2002,** 14, (1), 83-88.

27.   Jiang, P.; Hwang, K. S.; Mittleman, D. M.; Bertone, J. F.; Colvin, V. L., Template-directed preparation of macroporous polymers with oriented and crystalline arrays of voids. *Journal of the American Chemical Society* **1999,** 121, (50), 11630-11637.

28.   Geissler, M.; McLellan, J. M.; Chen, J. Y.; Xia, Y. N., Side-by-side patterning of multiple alkanethiolate monolayers on gold by edge-spreading lithography. *Angewandte Chemie-International Edition* **2005,** 44, (23), 3596-3600.

29.   Cai, Y. G.; Ocko, B. M., Large-scale fabrication of protein nanoarrays based on nanosphere lithography. *Langmuir* **2005,** 21, (20), 9274-9279.

30.   Garno, J. C.; Amro, N. A.; Wadu-Mesthrige, K.; Liu, G. Y., Production of periodic arrays of protein nanostructures using particle lithography. *Langmuir* **2002,** 18, (21), 8186-8192.

31.   Li, J. R.; Henry, G. C.; Garno, J. C., Fabrication of nanopatterned films of bovine serum albumin and staphylococcal protein A using latex particle lithography. *Analyst* **2006,** 131, (2), 244-250.

32.   Ngunjiri, J. N.; Daniels, S. L.; Li, J. R.; Serem, W. K.; Garno, J. C., Controlling the surface coverage and arrangement of proteins using particle lithography. *Nanomedicine* **2008,** 3, (4), 529-541.

33.   Sagiv, J., Organized monolayers by adsorption .1. Formation and structure of oleophobic mixed monolayers on solid-surfaces. *Journal of the American Chemical Society* **1980,** 102, (1), 92-98.

34.   Ulman, A., Formation and structure of self-assembled monolayers. *Chemical Reviews* **1996,** 96, (4), 1533-1554.

35.   Onclin, S.; Ravoo, B. J.; Reinhoudt, D. N., Engineering silicon oxide surfaces using self-assembled monolayers. *Angewandte Chemie-International Edition* **2005,** 44, (39), 6282-6304.

36.   Li, J. R.; Garno, J. C., Elucidating the role of surface hydrolysis in preparing organosilane nanostructures via particle lithography. *Nano Letters* **2008,** 8, (7), 1916-1922.

37.   Li, J. R.; Garno, J. C., Nanostructures of Octadecyltrisiloxane Self-Assembled Monolayers Produced on Au(111) Using Particle Lithography. *ACS Applied Materials & Interfaces* **2009,** in press.

38.   Li, J. R.; Lusker, L. K.; Yu, J. J.; Garno, J. C., Engineering the spatial selectivity of surfaces at the nanoscale by patterning organosilane self-assembled monolayers via particle lithography. *ACS Nano* **2009,** in submission.

39.   Li, J.-R.; Garno, J. C., Electroless deposition of metals on nanopatterns of organosilane SAMs. *ECS Transactions* **2008,** 13, 121-128.

40.   Li, J. R.; Lewandowski, B. R.; Xu, S.; Garno, J. C., Characteristics and Recognition of Magnetic Response of Iron Oxide-Capped Organosilane Nanostructures Investigated Using Magnetic Sample Modulation. *Analytical Chemistry* **2009,** accepted.

41.   Rossi, R. C.; Tan, M. X.; Lewis, N. S., Size-dependent electrical behavior of spatially inhomogeneous barrier height regions on silicon. *Applied Physics Letters* **2000,** 77, (17), 2698-2700.

42.   Roduner, E., Size matters: why nanomaterials are different. *Chemical Society Reviews* **2006,** 35, (7), 583-592.

43.   Maoz, R.; Frydman, E.; Cohen, S. R.; Sagiv, J., Constructive nanolithography: Site-defined silver self-assembly on nanoelectrochemically patterned monolayer templates. *Advanced Materials* **2000,** 12, (6), 424-429.

44.   Martin, C. R., Nanomaterials - A membrane-based synthetic approach. *Science* **1994,** 266, (5193), 1961-1966.

45.   Li, J. R.; Garno, J. C., Indirect Modulation of Nonmagnetic Probes for Force Modulation Atomic Force Microscopy. *Analytical Chemistry* **2009,** 81, (4), 1699-1706.

46.   Jarai-Szabo, F.; Astilean, S.; Neda, Z., Understanding self-assembled nanosphere patterns. *Chemical Physics Letters* **2005,** 408, (4-6), 241-246.

47.   Rabani, E.; Reichman, D. R.; Geissler, P. L.; Brus, L. E., Drying-mediated self-assembly of nanoparticles. *Nature* **2003,** 426, (6964), 271-274.

48.   Tessier, P.; Velev, O. D.; Kalambur, A. T.; Lenhoff, A. M.; Rabolt, J. F.; Kaler, E. W., Structured metallic films for optical and spectroscopic applications via colloidal crystal templating. *Advanced Materials* **2001,** 13, (6), 396-400.

49.   Chen, Z.; Zhan, P.; Wang, Z. L.; Zhang, J. H.; Zhang, W. Y.; Ming, N. B.; Chan, C. T.; Sheng, P., Two- and three-dimensional ordered structures of hollow silver spheres prepared by colloidal crystal templating. *Advanced Materials* **2004,** 16, (5), 417-422.

50.   Haynes, C. L.; Van Duyne, R. P., Dichroic optical properties of extended nanostructures fabricated using angle-resolved nanosphere lithography. *Nano Letters* **2003,** 3, (7), 939-943.

51.   Frey, W.; Woods, C. K.; Chilkoti, A., Ultraflat nanosphere lithography: A new method to fabricate flat nanostructures. *Advanced Materials* **2000,** 12, (20), 1515-1519.

52.   Sun, F. Q.; Cai, W. P.; Li, Y.; Cao, B. Q.; Lu, F.; Duan, G. T.; Zhang, L. D., Morphology control and transferability of ordered through-pore arrays based on electrodeposition and colloidal monolayers. *Advanced Materials* **2004,** 16, (13), 1116-1121.

53.   Abdelsalam, M. E.; Bartlett, P. N.; Baumberg, J. J.; Coyle, S., Preparation of arrays of isolated spherical cavities by self-assembly of polystyrene spheres on self-assembled pre-patterned macroporous films. *Advanced Materials* **2004,** 16, (1), 90-93.

54.   Winzer, M.; Kleiber, M.; Dix, N.; Wiesendanger, R., Fabrication of nano-dot- and nano-ring-arrays by nanosphere lithography. *Applied Physics a-Materials Science & Processing* **1996,** 63, (6), 617-619.

55.   Gustavsson, M.; Fredriksson, H.; Kasemo, B.; Jusys, Z.; Kaiser, J.; Jun, C.; Behm, R. J., Nanostructured platinum-on-carbon model electrocatalysts prepared by colloidal lithography. *Journal of Electroanalytical Chemistry* **2004,** 568, (1-2), 371-377.

56.   Chen, X.; Chen, Z. M.; Fu, N.; Lu, G.; Yang, B., Versatile nanopatterned surfaces generated via three-dimensional colloidal crystals. *Advanced Materials* **2003,** 15, (17), 1413-1417.

57.   Wang, Y.; Han, S. B.; Briseno, A. L.; Sanedrin, R. J. G.; Zhou, F. M., A modified nanosphere lithography for the fabrication of aminosilane/polystyrene nanoring arrays and the subsequent attachment of gold or DNA-capped gold nanoparticles. *Journal of Materials Chemistry* **2004,** 14, (24), 3488-3494.

58.   Briseno, A. L.; Han, S. B.; Rauda, I. E.; Zhou, F. M.; Toh, C. S.; Nemanick, E. J.; Lewis, N. S., Electrochemical polymerization of aniline monomers infiltrated into well-ordered truncated eggshell structures of polyelectrolyte multilayers. *Langmuir* **2004,** 20, (1), 219-226.

59.   Yan, F.; Goedel, W. A., The preparation of mesoscopic rings in colloidal crystal templates. *Angewandte Chemie-International Edition* **2005,** 44, (14), 2084-2088.

60.   Gates, B.; Yin, Y. D.; Xia, Y. N., Fabrication and characterization of porous membranes with highly ordered three-dimensional periodic structures. *Chemistry of Materials* **1999,** 11, (10), 2827-2836.

61.   Velev, O. D.; Jede, T. A.; Lobo, R. F.; Lenhoff, A. M., Microstructured porous silica obtained via colloidal crystal templates. *Chemistry of Materials* **1998,** 10, (11), 3597-3602.

62.   Xu, D. W.; Graugnard, E.; King, J. S.; Zhong, L. W.; Summers, C. J., Large-scale fabrication of ordered nanobowl arrays. *Nano Letters* **2004,** 4, (11), 2223-2226.

63.   Holland, B. T.; Blanford, C. F.; Do, T.; Stein, A., Synthesis of highly ordered, three-dimensional, macroporous structures of amorphous or crystalline inorganic oxides, phosphates, and hybrid composites. *Chemistry of Materials* **1999,** 11, (3), 795-805.

64. Valsesia, A.; Colpo, P.; Silvan, M. M.; Meziani, T.; Ceccone, G.; Rossi, F., Fabrication of nanostructured polymeric surfaces for biosensing devices. *Nano Letters* **2004,** 4, (6), 1047-1050.

65. Kawaguchi, H., Functional polymer microspheres. *Progress in Polymer Science* **2000,** 25, (8), 1171-1210.

66. Wang, D. Y.; Salgueirino-Maceira, V.; Liz-Marzan, L. W.; Caruso, F., Gold-silica inverse opals by colloidal crystal templating. *Advanced Materials* **2002,** 14, (12), 908-912.

67. Subramania, G.; Constant, K.; Biswas, R.; Sigalas, M. M.; Ho, K. M., Inverse face-centered cubic thin film photonic crystals. *Advanced Materials* **2001,** 13, (6), 443-446.

68. Wang, D. Y.; Rogach, A. L.; Caruso, F., Composite photonic crystals from semiconductor nanocrystal/polyelectrolyte-coated colloidal spheres. *Chemistry of Materials* **2003,** 15, (14), 2724-2729.

69. Norris, D. J.; Arlinghaus, E. G.; Meng, L. L.; Heiny, R.; Scriven, L. E., Opaline photonic crystals: How does self-assembly work? *Advanced Materials* **2004,** 16, (16), 1393-1399.

70. Jiang, P., Surface-templated nanostructured films with two-dimensional ordered arrays of voids. *Angewandte Chemie-International Edition* **2004,** 43, (42), 5625-5628.

71. Denis, F. A.; Hanarp, P.; Sutherland, D. S.; Dufrene, Y. F., Nanoscale chemical patterns fabricated by using colloidal lithography and self-assembled monolayers. *Langmuir* **2004,** 20, (21), 9335-9339.

72. Michel, R.; Reviakine, I.; Sutherland, D.; Fokas, C.; Csucs, G.; Danuser, G.; Spencer, N. D.; Textor, M., A novel approach to produce biologically relevant chemical patterns at the nanometer scale: Selective molecular assembly patterning combined with colloidal lithography. *Langmuir* **2002,** 18, (22), 8580-8586.

73. Bergveld, P., The future of biosensors. *Sensors and Actuators a-Physical* **1996,** 56, (1-2), 65-73.

74. Kunz, R. E., Miniature integrated optical modules for chemical and biochemical sensing. *Sensors and Actuators B-Chemical* **1997,** 38, (1-3), 13-28.

75. Templin, M. F.; Stoll, D.; Schwenk, J. M.; Potz, O.; Kramer, S.; Joos, T. O., Protein microarrays: Promising tools for proteomic research. *Proteomics* **2003,** 3, (11), 2155-2166.

76. Walt, D. R., Miniature analytical methods for medical diagnostics. *Science* **2005,** 308, (5719), 217-219.

77. Blawas, A. S.; Reichert, W. M., Protein patterning. *Biomaterials* **1998,** 19, (7-9), 595-609.

78.   Scouten, W. H.; Luong, J. H. T.; Brown, R. S., Enzyme or protein immobilization techniques for applications in biosensor design. *Trends in Biotechnology* **1995,** 13, (5), 178-185.

79.   Zhang, S. G.; Yan, L.; Altman, M.; Lassle, M.; Nugent, H.; Frankel, F.; Lauffenburger, D. A.; Whitesides, G. M.; Rich, A., Biological surface engineering: a simple system for cell pattern formation. *Biomaterials* **1999,** 20, (13), 1213-1220.

80.   Schweitzer, B.; Kingsmore, S. F., Measuring proteins on microarrays. *Current Opinion in Biotechnology* **2002,** 13, (1), 14-19.

81.   Templin, M. F.; Stoll, D.; Schrenk, M.; Traub, P. C.; Vohringer, C. F.; Joos, T. O., Protein microarray technology. *Trends in Biotechnology* **2002,** 20, (4), 160-166.

82.   Wilson, D. S.; Nock, S., Functional protein microarrays. *Current Opinion in Chemical Biology* **2002,** 6, (1), 81-85.

83.   Eggers, M.; Hogan, M.; Reich, R. K.; Lamture, J.; Ehrlich, D.; Hollis, M.; Kosicki, B.; Powdrill, T.; Beattie, K.; Smith, S.; Varma, R.; Gangadharan, R.; Mallik, A.; Burke, B.; Wallace, D., A microchip for quantitative detection of molecules utilizing luminescent and radioisotope reporter groups. *Biotechniques* **1994,** 17, (3), 516-525.

84.   Lee, K. B.; Kim, E. Y.; Mirkin, C. A.; Wolinsky, S. M., The use of nanoarrays for highly sensitive and selective detection of human immunodeficiency virus type 1 in plasma. *Nano Letters* **2004,** 4, (10), 1869-1872.

85.   Marquette, C. A.; Degiuli, A.; Imbert-Laurenceau, E.; Mallet, F.; Chaix, C.; Mandrand, B.; Blum, L. J., Latex bead immobilisation in PDMS matrix for the detection of p53 gene point mutation and anti-HIV-1 capsid protein antibodies. *Analytical and Bioanalytical Chemistry* **2005,** 381, (5), 1019-1024.

86.   Wang, D. Y.; Mohwald, H., Template-directed colloidal self-assembly - the route to 'top-down' nanochemical engineering. *Journal of Materials Chemistry* **2004,** 14, (4), 459-468.

87.   Geissler, M.; Xia, Y. N., Patterning: Principles and some new developments. *Advanced Materials* **2004,** 16, (15), 1249-1269.

88.   Hulteen, J. C.; Van Duyne, R. P., Nanosphere lithography - a materials general fabrication process for periodic particle array surfaces. *Journal of Vacuum Science & Technology a-Vacuum Surfaces and Films* **1995,** 13, (3), 1553-1558.

89.   Rosenoer, V. M.; Oratz, M.; Rothschilde, M. A., Albumin structure and function. *Pergamon Press, New York* **1977**.

90.   Chen, Y. Y.; Ford, W. T.; Materer, N. F.; Teeters, D., Conversion of colloidal crystals to polymer nets: Turning latex particles inside out. *Chemistry of Materials* **2001,** 13, (8), 2697-2704.

91.   Kim, A. J.; Manoharan, V. N.; Crocker, J. C., Swelling-based method for preparing stable, functionalized polymer colloids. *Journal of the American Chemical Society* **2005,** 127, (6), 1592-1593.

92.   Moks, T.; Abrahmsen, L.; Nilsson, B.; Hellman, U.; Sjoquist, J.; Uhlen, M., Staphylococcal protein-A consists of 5 IgG-binding domains. *European Journal of Biochemistry* **1986,** 156, (3), 637-643.

93.   Ren, X. Z.; Kobatake, E.; Aizawa, M., A new type of reusable piezoimmunosensor fabricated by a recombinant IgG-binding protein. *Analyst* **2000,** 125, (4), 669-671.

94.   Bjork, I.; Peters, B.-A.; Sjoquist, J., Some physicochemical properties of protein A from staphylococcus aureus. *European Journal of Biochemistry* **1972,** 29, (3), 579-584.

95.   Medintz, I. L.; Uyeda, H. T.; Goldman, E. R.; Mattoussi, H., Quantum dot bioconjugates for imaging, labelling and sensing. *Nature Materials* **2005,** 4, (6), 435-446.

96.   Hyun, J.; Ahn, S. J.; Lee, W. K.; Chilkoti, A.; Zauscher, S., Molecular recognition-mediated fabrication of protein nanostructures by dip-pen lithography. *Nano Letters* **2002,** 2, (11), 1203-1207.

97.   Reed, M. A.; Zhou, C.; Muller, C. J.; Burgin, T. P.; Tour, J. M., Conductance of a molecular junction. *Science* **1997,** 278, (5336), 252-254.

98.   Joachim, C.; Gimzewski, J. K.; Aviram, A., Electronics using hybrid-molecular and mono-molecular devices. *Nature* **2000,** 408, (6812), 541-548.

99.   Carroll, R. L.; Gorman, C. B., The genesis of molecular electronics. *Angewandte Chemie-International Edition* **2002,** 41, (23), 4379-4400.

100.   Nitzan, A.; Ratner, M. A., Electron transport in molecular wire junctions. *Science* **2003,** 300, (5624), 1384-1389.

101.   Schreiber, F., Structure and growth of self-assembling monolayers. *Progress in Surface Science* **2000,** 65, (5-8), 151-256.

102.   Nuzzo, R. G.; Allara, D. L., Adsorption of bifunctional organic disulfides on gold surfaces. *Journal of the American Chemical Society* **1983,** 105, (13), 4481-4483.

103.   Love, J. C.; Estroff, L. A.; Kriebel, J. K.; Nuzzo, R. G.; Whitesides, G. M., Self-assembled monolayers of thiolates on metals as a form of nanotechnology. *Chemical Reviews* **2005,** 105, (4), 1103-1169.

104.   Wen, K.; Maoz, R.; Cohen, H.; Sagiv, J.; Gibaud, A.; Desert, A.; Ocko, B. M., Postassembly chemical modification of a highly ordered organosilane multilayer: New

insights into the structure, bonding, and dynamics of self-assembling silane monolayers. *Acs Nano* **2008,** 2, (3), 579-599.

105.   Kessel, C. R.; Granick, S., Formation and characterization of a highly ordered and well-anchored alkylsilane monolayer on mica by self-assembly. *Langmuir* **1991,** 7, (3), 532-538.

106.   Schwartz, D. K.; Steinberg, S.; Israelachvili, J.; Zasadzinski, J. A. N., Growth of a self-assembled monolayer by fractal aggregation. *Physical Review Letters* **1992,** 69, (23), 3354-3357.

107.   Wasserman, S. R.; Tao, Y. T.; Whitesides, G. M., Structure and reactivity of alkylsiloxane monolayers formed by reaction of alkyltrichlorosilanes on silicon substrates. *Langmuir* **1989,** 5, (4), 1074-1087.

108.   Maoz, R.; Sagiv, J., Penetration-controlled reactions in organized monolayer assemblies .1. Aqueous permanganate interaction with monolayer and multilayer films of long-chain surfactants. *Langmuir* **1987,** 3, (6), 1034-1044.

109.   Rozlosnik, N.; Gerstenberg, M. C.; Larsen, N. B., Effect of solvents and concentration on the formation of a self-assembled monolayer of octadecylsiloxane on silicon (001). *Langmuir* **2003,** 19, (4), 1182-1188.

110.   Pallandre, A.; Glinel, K.; Jonas, A. M.; Nysten, B., Binary nanopatterned surfaces prepared from silane monolayers. *Nano Letters* **2004,** 4, (2), 365-371.

111.   Hoffmann, P. W.; Stelzle, M.; Rabolt, J. F., Vapor phase self-assembly of fluorinated monolayers on silicon and germanium oxide. *Langmuir* **1997,** 13, (7), 1877-1880.

112.   Fadeev, A. Y.; McCarthy, T. J., Self-assembly is not the only reaction possible between alkyltrichlorosilanes and surfaces: Monomolecular and oligomeric covalently attached layers of dichloro- and trichloroalkylsilanes on silicon. *Langmuir* **2000,** 16, (18), 7268-7274.

113.   Vallant, T.; Brunner, H.; Mayer, U.; Hoffmann, H.; Leitner, T.; Resch, R.; Friedbacher, G., Formation of self-assembled octadecylsiloxane monolayers on mica and silicon surfaces studied by atomic force microscopy and infrared spectroscopy. *Journal of Physical Chemistry B* **1998,** 102, (37), 7190-7197.

114.   Jeon, N. L.; Finnie, K.; Branshaw, K.; Nuzzo, R. G., Structure and stability of patterned self-assembled films of octadecyltrichlorosilane formed by contact printing. *Langmuir* **1997,** 13, (13), 3382-3391.

115.   Allara, D. L.; Parikh, A. N.; Rondelez, F., Evidence for a unique chain organization in long-chain silane monolayers deposited on 2 widely different solid substrates. *Langmuir* **1995,** 11, (7), 2357-2360.

116. Parikh, A. N.; Allara, D. L.; Azouz, I. B.; Rondelez, F., An intrinsic relationship between molecular-structure in self-assembled N-alkylsiloxane monolayers and deposition temperature. *Journal of Physical Chemistry* **1994,** 98, (31), 7577-7590.

117. Richter, A. G.; Durbin, M. K.; Yu, C. J.; Dutta, L., In situ time-resolved X-ray reflectivity study of self-assembly from solution. *Langmuir* **1998,** 14, (21), 5980-5983.

118. Kojio, K.; Takahara, A.; Omote, K.; Kajiyama, T., Molecular aggregation state of n-octadecyltrichlorosilane monolayers prepared by the Langmuir and chemisorption methods. *Langmuir* **2000,** 16, (8), 3932-3936.

119. Hoffmann, H.; Mayer, U.; Krischanitz, A., Structure of alkylsiloxane monolayers on silicon surfaces investigated by external reflection infrared-spectroscopy. *Langmuir* **1995,** 11, (4), 1304-1312.

120. Fragneto, G.; Lu, J. R.; McDermott, D. C.; Thomas, R. K.; Rennie, A. R.; Gallagher, P. D.; Satija, S. K., Structure of monolayers of tetraethylene glycol monododecyl ether adsorbed on self-assembled monolayers on silicon: A neutron reflectivity study. *Langmuir* **1996,** 12, (2), 477-486.

121. Tripp, C. P.; Hair, M. L., An infrared study of the reaction of octadecyltrichlorosilane with silica. *Langmuir* **1992,** 8, (4), 1120-1126.

122. Carson, G. A.; Granick, S., Self-assembly of octadecyltrichlorosilane monolayers on mica. *Journal of Materials Research* **1990,** 5, (8), 1745-1751.

123. Krasnoslobodtsev, A. V.; Smirnov, S. N., Effect of water on silanization of silica by trimethoxysilanes. *Langmuir* **2002,** 18, (8), 3181-3184.

124. Angst, D. L.; Simmons, G. W., Moisture Absorption characteristics of organosiloxane self-assembled monolayers. *Langmuir* **1991,** 7, (10), 2236-2242.

125. Le Grange, J. D.; Markham, J. L.; Kurkjian, C. R., Effects of surface hydration on the deposition of silane monolayers on silica. *Langmuir* **1993,** 9, (7), 1749-1753.

126. Brandow, S. L.; Chen, M. S.; Aggarwal, R.; Dulcey, C. S.; Calvert, J. M.; Dressick, W. J., Fabrication of patterned amine reactivity templates using 4-chloromethylphenylsiloxane self-assembled monolayer films. *Langmuir* **1999,** 15, (16), 5429-5432.

127. Lercel, M. J.; Redinbo, G. F.; Pardo, F. D.; Rooks, M.; Tiberio, R. C.; Simpson, P.; Craighead, H. G.; Sheen, C. W.; Parikh, A. N.; Allara, D. L., Electron-beam lithography with monolayers of alkylthiols and alkylsiloxanes. *Journal of Vacuum Science & Technology B* **1994,** 12, (6), 3663-3667.

128. Lercel, M. J.; Craighead, H. G.; Parikh, A. N.; Seshadri, K.; Allara, D. L., Sub-10 nm lithography with self-assembled monolayers. *Applied Physics Letters* **1996,** 68, (11), 1504-1506.

129. Wang, D. W.; Thomas, S. G.; Wang, K. L.; Xia, Y. N.; Whitesides, G. M., Nanometer scale patterning and pattern transfer on amorphous Si, crystalline Si, and SiO2 surfaces using self-assembled monolayers. *Applied Physics Letters* **1997,** 70, (12), 1593-1595.

130. Jung, H.; Kulkarni, R.; Collier, C. P., Dip-pen nanolithography of reactive alkoxysilanes on glass. *Journal of the American Chemical Society* **2003,** 125, (40), 12096-12097.

131. Jourdan, J. S.; Cruchon-Dupeyrat, S. J.; Huan, Y.; Kuo, P. K.; Liu, G. Y., Imaging nanoscopic elasticity of thin film materials by atomic force microscopy: Effects of force modulation frequency and amplitude. *Langmuir* **1999,** 15, (19), 6495-6504.

132. Headrick, J. E.; Armstrong, M.; Cratty, J.; Hammond, S.; Sheriff, B. A.; Berrie, C. L., Nanoscale patterning of alkyl monolayers on silicon using the atomic force microscope. *Langmuir* **2005,** 21, (9), 4117-4122.

133. Maoz, R.; Frydman, E.; Cohen, S. R.; Sagiv, J., "Constructive nanolithography": Inert monolayers as patternable templates for in-situ nanofabrication of metal-semiconductor-organic surface structures - A generic approach. *Advanced Materials* **2000,** 12, (10), 725-731.

134. Marquez, M.; Patel, K.; Carswell, A. D. W.; Schmidtke, D. W.; Grady, B. P., Synthesis of nanometer-scale polymeric structures on surfaces from template assisted admicellar polymerization: A comparative study with protein adsorption. *Langmuir* **2006,** 22, (19), 8010-8016.

135. McLellan, J. M.; Geissler, M.; Xia, Y. N., Edge spreading lithography and its application to the fabrication of mesoscopic gold and silver rings. *Journal of the American Chemical Society* **2004,** 126, (35), 10830-10831.

136. Bae, C.; Shin, H. J.; Moon, J.; Sung, M. M., Contact area lithography (CAL): A new approach to direct formation of nanometric chemical patterns. *Chemistry of Materials* **2006,** 18, (5), 1085-1088.

137. Denkov, N. D.; Velev, O. D.; Kralchevsky, P. A.; Ivanov, I. B.; Yoshimura, H.; Nagayama, K., Mechanism of formation of 2-dimensional crystals from latex-particles on substrates. *Langmuir* **1992,** 8, (12), 3183-3190.

138. Klapetek, P. N., D.; Czech Metrology Institute: Czech Republic, 2007, http://gwyddion.net/.

139. Xiao, X. D.; Liu, G. Y.; Charych, D. H.; Salmeron, M., Preparation, structure, and mechanical stability of alkylsilane monolayers on mica. *Langmuir* **1995,** 11, (5), 1600-1604.

140. Kingshott, P.; Griesser, H. J., Surfaces that resist bioadhesion. *Current Opinion in Solid State & Materials Science* **1999,** 4, (4), 403-412.

141. Herrwerth, S.; Eck, W.; Reinhardt, S.; Grunze, M., Factors that determine the protein resistance of oligoether self-assembled monolayers - Internal hydrophilicity, terminal hydrophilicity, and lateral packing density. *Journal of the American Chemical Society* **2003,** 125, (31), 9359-9366.

142. Choi, I.; Kang, S. K.; Lee, J.; Kim, Y.; Yi, J., In situ observation of biomolecules patterned on a PEG-modified Si surface by scanning probe lithography. *Biomaterials* **2006,** 27, (26), 4655-4660.

143. Prevo, B. G.; Velev, O. D., Controlled, rapid deposition of structured coatings from micro- and nanoparticle suspensions. *Langmuir* **2004,** 20, (6), 2099-2107.

144. Marquez, M.; Grady, B. P., The use of surface tension to predict the formation of 2D arrays of latex spheres formed via the Langmuir-Blodgett-like technique. *Langmuir* **2004,** 20, (25), 10998-11004.

145. Thames, S. F.; Panjnani, K. G., Organosilane polymer chemistry: A review. *Journal of Inorganic and Organometallic Polymers* **1996,** 6, (2), 59-94.

146. Grabar, K. C.; Allison, K. J.; Baker, B. E.; Bright, R. M.; Brown, K. R.; Freeman, R. G.; Fox, A. P.; Keating, C. D.; Musick, M. D.; Natan, M. J., Two-dimensional arrays of colloidal gold particles: A flexible approach to macroscopic metal surfaces. *Langmuir* **1996,** 12, (10), 2353-2361.

147. Chrisey, L. A.; Lee, G. U.; Oferrall, C. E., Covalent attachment of synthetic DNA to self-assembled monolayer films. *Nucleic Acids Research* **1996,** 24, (15), 3031-3039.

148. Mooney, J. F.; Hunt, A. J.; McIntosh, J. R.; Liberko, C. A.; Walba, D. M.; Rogers, C. T., Patterning of functional antibodies and other proteins by photolithography of silane monolayers. *Proceedings of the National Academy of Sciences of the United States of America* **1996,** 93, (22), 12287-12291.

149. Gao, Y. F.; Koumoto, K., Bioinspired ceramic thin film processing: Present status and future perspectives. *Crystal Growth & Design* **2005,** 5, (5), 1983-2017.

150. Balachander, N.; Sukenik, C. N., Monolayer transformation by nucleophilic-substitution - Applications to the creation of new monolayer assemblies. *Langmuir* **1990,** 6, (11), 1621-1627.

151. Maoz, R.; Cohen, S. R.; Sagiv, J., Nanoelectrochemical patterning of monolayer surfaces: Toward spatially defined self-assembly of nanostructures. *Advanced Materials* **1999,** 11, (1), 55-61.

152. Killampalli, A. S.; Ma, P. F.; Engstrom, J. R., The reaction of tetrakis(dimethylamido)titanium with self-assembled alkyltrichlorosilane monolayers possessing -OH, -NH2, and -CH3 terminal groups. *Journal of the American Chemical Society* **2005,** 127, (17), 6300-6310.

153. Britt, D. W.; Hlady, V., An AFM study of the effects of silanization temperature, hydration, and annealing on the nucleation and aggregation of condensed OTS domains on mica. *Journal of Colloid and Interface Science* **1996,** 178, (2), 775-784.

154. Wu, K.; Bailey, T. C.; Willson, C. G.; Ekerdt, J. G., Surface hydration and its effect on fluorinated SAM formation on SiO2 surfaces. *Langmuir* **2005,** 21, (25), 11795-11801.

155. Finklea, H. O.; Robinson, L. R.; Blackburn, A.; Richter, B.; Allara, D.; Bright, T., Formation of an organized monolayer by solution adsorption of octadecyltrichlorosilane on gold - Electrochemical properties and structural characterization. *Langmuir* **1986,** 2, (2), 239-244.

156. Sabatani, E.; Rubinstein, I.; Maoz, R.; Sagiv, J., Organized self-assembling monolayers on electrodes .1. Octadecyl derivatives on gold. *Journal of Electroanalytical Chemistry* **1987,** 219, (1-2), 365-371.

157. Vallant, T.; Brunner, H.; Kattner, J.; Mayer, U.; Hoffmann, H.; Leitner, T.; Friedbacher, G.; Schugerl, G.; Svagera, R.; Ebel, M., Monolayer-controlled deposition of silicon oxide films on gold, silicon, and mica substrates by room-temperature adsorption and oxidation of alkylsiloxane monolayers. *Journal of Physical Chemistry B* **2000,** 104, (22), 5309-5317.

158. Sabatani, E.; Rubinstein, I., Organized self-assembling monolayers on electrodes .2. Monolayer-based ultramicroelectrodes for the study of very rapid electrode-kinetics. *Journal of Physical Chemistry* **1987,** 91, (27), 6663-6669.

159. Kurth, D. G.; Bein, T., Thin-films of (3-aminopropyl)triethoxysilane on aluminum-oxide and gold substrates. *Langmuir* **1995,** 11, (8), 3061-3067.

160. Katsonis, N.; Marchenko, A.; Taillemite, S.; Fichou, D.; Chouraqui, G.; Aubert, C.; Malacria, M., A molecular approach to self-assembly of trimethylsilylacetylene derivatives on gold. *Chemistry-a European Journal* **2003,** 9, (11), 2574-2581.

161. Owens, T. M.; Nicholson, K. T.; Holl, M. M. B.; Suzer, S., Formation of alkylsilane-based monolayers on gold. *Journal of the American Chemical Society* **2002,** 124, (24), 6800-6801.

162. Owens, T. M.; Suzer, S.; Holl, M. M. B., Variable energy X-ray photoemission studies of alkylsilane based monolayers on gold. *Journal of Physical Chemistry B* **2003,** 107, (14), 3177-3182.

163. Owens, T. M.; Ludwig, B. J.; Schneider, K. S.; Fosnacht, D. R.; Orr, B. G.; Holl, M. M. B., Oxidation of alkylsilane-based monolayers on gold. *Langmuir* **2004,** 20, (22), 9636-9645.

164. White, M. L., Wetting of gold surfaces by water. *Journal of Physical Chemistry* **1964,** 68, (10), 3083-3085.

165. Bewig, K. W.; Zisman, W. A., Wetting of gold and platinum by water. *Journal of Physical Chemistry* **1965,** 69, (12), 4238-4242.

166. Erb, R. A., Wettability of gold. *Journal of Physical Chemistry* **1968,** 72, (7), 2412-2417.

167. Gardner, J. R.; Woods, R., Hydrophilic nature of gold and platinum. *Journal of Electroanalytical Chemistry* **1977,** 81, (2), 285-290.

168. Smith, T., The hydrophilic nature of a clean gold surface. *Journal of Colloid and Interface Science* **1980,** 75, (1), 51-55.

169. Zettlemoyer, A. C., Hydrophobic surfaces. *Journal of Colloid and Interface Science* **1968,** 28, (3-4), 343-369.

170. White, M. L.; Drobek, J., Effect of residual abrasives on wettability of polished gold surfaces. *Journal of Physical Chemistry* **1966,** 70, (11), 3432-3436.

171. Erb, R. A., Wettability of metals under continuous condensing conditions. *Journal of Physical Chemistry* **1965,** 69, (4), 1306-1309.

172. Rubinstein, I.; Steinberg, S.; Tor, Y.; Shanzer, A.; Sagiv, J., Ionic recognition and selective response in self-assembling monolayer membranes on electrodes. *Nature* **1988,** 332, (6163), 426-429.

173. Evans, S. D.; Sharma, R.; Ulman, A., Contact-angle stability - Reorganization of monolayer surfaces. *Langmuir* **1991,** 7, (1), 156-161.

174. Sondag-Huethorst, J. A. M.; Fokkink, L. G. J., Potential-dependent wetting of octadecanethiol-modified polycrystalline gold electrodes. *Langmuir* **1992,** 8, (10), 2560-2566.

175. King, D. E., Oxidation of gold by ultraviolet-light and ozone at 25-degrees-C. *Journal of Vacuum Science & Technology A-Vacuum Surfaces and Films* **1995,** 13, (3), 1247-1253.

176. Yang, S. M.; Jang, S. G.; Choi, D. G.; Kim, S.; Yu, H. K., Nanomachining by colloidal lithography. *Small* **2006,** 2, (4), 458-475.

177. Jiang, P.; McFarland, M. J., Large-scale fabrication of wafer-size colloidal crystals, macroporous polymers and nanocomposites by spin-coating. *Journal of the American Chemical Society* **2004,** 126, (42), 13778-13786.

178. Aswal, D. K.; Lenfant, S.; Guerin, D.; Yakhmi, J. V.; Vuillaume, D., A tunnel current in self-assembled monolayers of 3-mercaptopropyltrimethoxysilane. *Small* **2005,** 1, (7), 725-729.

179. Aswal, D. K.; Lenfant, S.; Guerin, D.; Yakhmi, J. V.; Vuillaume, D., Self assembled monolayers on silicon for molecular electronics. *Analytica Chimica Acta* **2006,** 568, (1-2), 84-108.

180. Chauhan, A. K.; Aswal, D. K.; Koiry, S. P.; Gupta, S. K.; Yakhmi, J. V.; Surgers, C.; Guerin, D.; Lenfant, S.; Vuillaume, D., Self-assembly of the 3-aminopropyltrimethoxysilane multilayers on Si and hysteretic current-voltage characteristics. *Applied Physics A-Materials Science & Processing* **2008,** 90, (3), 581-589.

181. Fontaine, P.; Goguenheim, D.; Deresmes, D.; Vuillaume, D.; Garet, M.; Rondelez, F., Octadecyltrichlorosilane monolayers as ultrathin gate insulating films in metal-insulator-semiconductor devices. *Applied Physics Letters* **1993,** 62, (18), 2256-2258.

182. Vuillaume, D.; Boulas, C.; Collet, J.; Davidovits, J. V.; Rondelez, F., Organic insulating films of nanometer thicknesses. *Applied Physics Letters* **1996,** 69, (11), 1646-1648.

183. Pireaux, J. J.; Liehr, M.; Thiry, P. A.; Delrue, J. P.; Caudano, R., Electron spectroscopic characterization of oxygen-adsorption on gold surfaces .2. Production of gold oxide in oxygen Dc reactive sputtering. *Surface Science* **1984,** 141, (1), 221-232.

184. Ron, H.; Rubinstein, I., Alkanethiol monolayers on preoxidized gold - Encapsulation of gold oxide under an organic monolayer. *Langmuir* **1994,** 10, (12), 4566-4573.

185. Neto, J. M. M.; Cardoso, A. L. H.; Testa, A. P.; Galembeck, F., Heterogeneity in polymer latices - Detection by zonal centrifugation. *Langmuir* **1994,** 10, (7), 2095-2099.

186. Tan, S. S.; Sherman, R. L.; Qin, D. Q.; Ford, W. T., Surface heterogeneity of polystyrene latex particles determined by dynamic force microscopy. *Langmuir* **2005,** 21, (1), 43-49.

187. Chan, W. C. W.; Nie, S. M., Quantum dot bioconjugates for ultrasensitive nonisotopic detection. *Science* **1998,** 281, (5385), 2016-2018.

188. Wong, S. S.; Joselevich, E.; Woolley, A. T.; Cheung, C. L.; Lieber, C. M., Covalently functionalized nanotubes as nanometre-sized probes in chemistry and biology. *Nature* **1998,** 394, (6688), 52-55.

189. Shi, H. Q.; Tsai, W. B.; Garrison, M. D.; Ferrari, S.; Ratner, B. D., Template-imprinted nanostructured surfaces for protein recognition. *Nature* **1999,** 398, (6728), 593-597.

190. Ahmed, H., Single electron electronics: Challenge for nanofabrication. *Journal of Vacuum Science & Technology B* **1997,** 15, (6), 2101-2108.

191. Mallory; O., G.; Hajdu, J. B., Electroless plating: Fundamentals and applications. *American Electroplaters and Surface Finishers Society, Orlando, FL* **1990**.

192. Dressick, W. J.; Dulcey, C. S.; Georger, J. H.; Calabrese, G. S.; Calvert, J. M., Covalent binding of Pd catalysts to ligating self-assembled monolayer films for selective electroless metal-deposition. *Journal of the Electrochemical Society* **1994,** 141, (1), 210-220.

193. Hidber, P. C.; Helbig, W.; Kim, E.; Whitesides, G. M., Microcontact printing of palladium colloids: Micron-scale patterning by electroless deposition of copper. *Langmuir* **1996,** 12, (5), 1375-1380.

194. Dubin, V. M.; ShachamDiamand, Y.; Zhao, B.; Vasudev, P. K.; Ting, C. H., Selective and blanket electroless copper deposition for ultralarge scale integration. *Journal of the Electrochemical Society* **1997,** 144, (3), 898-908.

195. Hilmi, A.; Luong, J. H. T., Electrochemical detectors prepared by electroless deposition for microfabricated electrophoresis chips. *Analytical Chemistry* **2000,** 72, (19), 4677-4682.

196. Kobayashi, Y.; Salgueirino-Maceira, V.; Liz-Marzan, L. M., Deposition of sliver nanoparticles on silica spheres by pretreatment steps in electroless plating. *Chemistry of Materials* **2001,** 13, (5), 1630-1633.

197. Saito, N.; Haneda, H.; Sekiguchi, T.; Ohashi, N.; Sakaguchi, I.; Koumoto, K., Low-temperature fabrication of light-emitting zinc oxide micropatterns using self-assembled monolayers. *Advanced Materials* **2002,** 14, (6), 418-421.

198. Zhang, X. Y.; Whitney, A. V.; Zhao, J.; Hicks, E. M.; Van Duyne, R. P., Advances in contemporary nanosphere lithographic techniques. *Journal of Nanoscience and Nanotechnology* **2006,** 6, (7), 1920-1934.

199. Li, Y.; Cai, W.; Duan, G., Ordered micro/nanostructured arrays based on the monolayer colloidal crystals. *Chemistry of Materials* **2008,** 20, (3), 615-624.

200. Jiang, P.; Cizeron, J.; Bertone, J. F.; Colvin, V. L., Preparation of macroporous metal films from colloidal crystals. *Journal of the American Chemical Society* **1999,** 121, (34), 7957-7958.

201. Wang, D. Y.; Caruso, F., Fabrication of polyaniline inverse opals via templating ordered colloidal assemblies. *Advanced Materials* **2001,** 13, (5), 350-353.

202.	Werdinius, C.; Osterlund, L.; Kasemo, B., Nanofabrication of planar model catalysts by colloidal lithography: Pt/ceria and Pt/alumina. *Langmuir* **2003,** 19, (2), 458-468.

203.	Xia, Y. N.; Whitesides, G. M., Soft lithography. *Annual Review of Materials Science* **1998,** 28, 153-184.

204.	Himpsel, F. J.; Ortega, J. E.; Mankey, G. J.; Willis, R. F., Magnetic nanostructures. *Advances in Physics* **1998,** 47, (4), 511-597.

205.	Chou, S. Y., Patterned magnetic nanostructures and quantized magnetic disks. *Proceedings of the IEEE* **1997,** 85, (4), 652-671.

206.	Tiwari, S.; Rana, F.; Hanafi, H.; Hartstein, A.; Crabbe, E. F.; Chan, K., A silicon nanocrystals based memory. *Applied Physics Letters* **1996,** 68, (10), 1377-1379.

207.	Duan, X. F.; Huang, Y.; Cui, Y.; Wang, J. F.; Lieber, C. M., Indium phosphide nanowires as building blocks for nanoscale electronic and optoelectronic devices. *Nature* **2001,** 409, (6816), 66-69.

208.	Wang, X. D.; Summers, C. J.; Wang, Z. L., Large-scale hexagonal-patterned growth of aligned ZnO nanorods for nano-optoelectronics and nanosensor arrays. *Nano Letters* **2004,** 4, (3), 423-426.

209.	Shipway, A. N.; Katz, E.; Willner, I., Nanoparticle arrays on surfaces for electronic, optical, and sensor applications. *Chemphyschem* **2000,** 1, (1), 18-52.

210.	Lin, Y. H.; Lu, F.; Tu, Y.; Ren, Z. F., Glucose biosensors based on carbon nanotube nanoelectrode ensembles. *Nano Letters* **2004,** 4, (2), 191-195.

211.	Kong, J.; Franklin, N. R.; Zhou, C. W.; Chapline, M. G.; Peng, S.; Cho, K. J.; Dai, H. J., Nanotube molecular wires as chemical sensors. *Science* **2000,** 287, (5453), 622-625.

212.	Zhou, C.; Deshpande, M. R.; Reed, M. A.; Jones, L.; Tour, J. M., Nanoscale metal self-assembled monolayer metal heterostructures. *Applied Physics Letters* **1997,** 71, (5), 611-613.

213.	Wolkow, R. A., Controlled molecular adsorption on silicon: Laying a foundation for molecular devices. *Annual Review of Physical Chemistry* **1999,** 50, 413-441.

214.	Hrapovic, S.; Liu, Y. L.; Male, K. B.; Luong, J. H. T., Electrochemical biosensing platforms using platinum nanoparticles and carbon nanotubes. *Analytical Chemistry* **2004,** 76, (4), 1083-1088.

215.	Lewandowski, B. R.; Kelley, A. T.; Singleton, R.; Li, J.-R.; Lowry, M.; Warner, I. M.; Garno, J. C., Nanostructures of Cysteine-Coated CdS Nanoparticles Produced with "Two-Particle" Lithography. *Journal of Physical Chemistry C* **2009,** 113, (15), 5933–5940.

216.	Chen, J. X.; Liao, W. S.; Chen, X.; Yang, T. L.; Wark, S. E.; Son, D. H.; Batteas, J. D.; Cremer, P. S., Evaporation-Induced Assembly of Quantum Dots into Nanorings. *ACS Nano* **2009,** 3, (1), 173-180.

217.	Brzoska, J. B.; Benazouz, I.; Rondelez, F., Silanization of Solid Substrates - a Step toward Reproducibility. *Langmuir* **1994,** 10, (11), 4367-4373.

218.	Hozumi, A.; Ushiyama, K.; Sugimura, H.; Takai, O., Fluoroalkylsilane monolayers formed by chemical vapor surface modification on hydroxylated oxide surfaces. *Langmuir* **1999,** 15, (22), 7600-7604.

219.	Grabar, K. C.; Freeman, R. G.; Hommer, M. B.; Natan, M. J., Preparation and Characterization of Au Colloid Monolayers. *Analytical Chemistry* **1995,** 67, (4), 735-743.

220.	Grabar, K. C.; Brown, K. R.; Keating, C. D.; Stranick, S. J.; Tang, S. L.; Natan, M. J., Nanoscale characterization of gold colloid monolayers: A comparison of four techniques. *Analytical Chemistry* **1997,** 69, (3), 471-477.

221.	Bierbaum, K.; Grunze, M.; Baski, A. A.; Chi, L. F.; Schrepp, W.; Fuchs, H., Growth of Self-Assembled N-Alkyltrichlorosilane Films on Si(100) Investigated by Atomic-Force Microscopy. *Langmuir* **1995,** 11, (6), 2143-2150.

222.	Banga, R.; Yarwood, J.; Morgan, A. M.; Evans, B.; Kells, J., FTIR and AFM Studies of the Kinetics and Self-Assembly of Alkyltrichlorosilanes and (Perfluoroalkyl)Trichlorosilanes onto Glass and Silicon. *Langmuir* **1995,** 11, (11), 4393-4399.

223.	Vandenberg, E. T.; Bertilsson, L.; Liedberg, B.; Uvdal, K.; Erlandsson, R.; Elwing, H.; Lundstrom, I., Structure of 3-Aminopropyl Triethoxy Silane on Silicon-Oxide. *Journal of Colloid and Interface Science* **1991,** 147, (1), 103-118.

224.	Horr, T. J.; Arora, P. S., Determination of the acid-base properties for 3-amino, 3-chloro and 3-mercaptopropyltrimethoxysilane coatings on silica surfaces by XPS. *Colloids and Surfaces a-Physicochemical and Engineering Aspects* **1997,** 126, (2-3), 113-121.

225.	Kristensen, E. M. E.; Nederberg, F.; Rensmo, H.; Bowden, T.; Hilborn, J.; Siegbahn, H., Photoelectron spectroscopy studies of the functionalization of a silicon surface with a phosphorylcholine-terminated polymer grafted onto (3-aminopropyl)trimethoxysilane. *Langmuir* **2006,** 22, (23), 9651-9657.

226.	Howarter, J. A.; Youngblood, J. P., Optimization of silica silanization by 3-aminopropyltriethoxysilane. *Langmuir* **2006,** 22, (26), 11142-11147.

227.	Radmacher, M.; Tilmann, R. W.; Gaub, H. E., Imaging viscoelasticity by force modulation with the atomic force microscope. *Biophysical Journal* **1993,** 64, (3), 735-742.

228. Magonov, S. N.; Reneker, D. H., Characterization of polymer surfaces with atomic force microscopy. *Annual Review of Materials Science* **1997,** 27, 175-222.

229. Finot, M. O.; McDermott, M. T., High-resolution chemical mapping of surface bound functional groups with tapping-mode scanning force microscopy. *Journal of the American Chemical Society* **1997,** 119, (36), 8564-8565.

230. Garcia, R.; Perez, R., Dynamic atomic force microscopy methods. *Surface Science Reports* **2002,** 47, (6-8), 197-301.

231. Freeman, R. G.; Grabar, K. C.; Allison, K. J.; Bright, R. M.; Davis, J. A.; Guthrie, A. P.; Hommer, M. B.; Jackson, M. A.; Smith, P. C.; Walter, D. G.; Natan, M. J., Self-Assembled Metal Colloid Monolayers - An Approach to SERS Substrates. *Science* **1995,** 267, (5204), 1629-1632.

232. Westcott, S. L.; Oldenburg, S. J.; Lee, T. R.; Halas, N. J., Formation and adsorption of clusters of gold nanoparticles onto functionalized silica nanoparticle surfaces. *Langmuir* **1998,** 14, (19), 5396-5401.

233. He, H. X.; Zhang, H.; Li, Q. G.; Zhu, T.; Li, S. F. Y.; Liu, Z. F., Fabrication of designed architectures of Au nanoparticles on solid substrate with printed self-assembled monolayers as templates. *Langmuir* **2000,** 16, (8), 3846-3851.

234. Rechberger, W.; Hohenau, A.; Leitner, A.; Krenn, J. R.; Lamprecht, B.; Aussenegg, F. R., Optical properties of two interacting gold nanoparticles. *Optics Communications* **2003,** 220, (1-3), 137-141.

235. Daniel, M. C.; Astruc, D., Gold nanoparticles: Assembly, supramolecular chemistry, quantum-size-related properties, and applications toward biology, catalysis, and nanotechnology. *Chemical Reviews* **2004,** 104, (1), 293-346.

236. Murphy, C. J.; San, T. K.; Gole, A. M.; Orendorff, C. J.; Gao, J. X.; Gou, L.; Hunyadi, S. E.; Li, T., Anisotropic metal nanoparticles: Synthesis, assembly, and optical applications. *Journal of Physical Chemistry B* **2005,** 109, (29), 13857-13870.

237. Lin, S.; Li, M.; Dujardin, E.; Girard, C.; Mann, S., One-dimensional plasmon coupling by facile self-assembly of gold nanoparticles into branched chain networks. *Advanced Materials* **2005,** 17, (21), 2553-2559.

238. Berkowitz, A. E.; Lahut, J. A.; Vanburen, C. E., Properties of magnetic fluid particles. *IEEE Transactions on Magnetics* **1980,** 16, (2), 184-190.

239. Chikazumi, S.; Taketomi, S.; Ukita, M.; Mizukami, M.; Miyajima, H.; Setogawa, M.; Kurihara, Y., Physics of magnetic fluids. *Journal of Magnetism and Magnetic Materials* **1987,** 65, (2-3), 245-251.

240. Taketomi, S.; Ukita, M.; Mizukami, M.; Miyajima, H.; Chikazumi, S., Magnetooptical effects of magnetic fluid. *Journal of the Physical Society of Japan* **1987,** 56, (9), 3362-3374.

241. Guillou, N.; Gao, Q.; Forster, P. M.; Chang, J. S.; Nogues, M.; Park, S. E.; Ferey, G.; Cheetham, A. K., Nickel(II) phosphate VSB-5: A magnetic nanoporous hydrogenation catalyst with 24-ring tunnels. *Angewandte Chemie-International Edition* **2001,** 40, (15), 2831-2834.

242. Yoon, T. J.; Lee, W.; Oh, Y. S.; Lee, J. K., Magnetic nanoparticles as a catalyst vehicle for simple and easy recycling. *New Journal of Chemistry* **2003,** 27, (2), 227-229.

243. Lu, A. H.; Schmidt, W.; Matoussevitch, N.; Bonnemann, H.; Spliethoff, B.; Tesche, B.; Bill, E.; Kiefer, W.; Schuth, F., Nanoengineering of a magnetically separable hydrogenation catalyst. *Angewandte Chemie-International Edition* **2004,** 43, (33), 4303-4306.

244. Olsvik, O.; Popovic, T.; Skjerve, E.; Cudjoe, K. S.; Hornes, E.; Ugelstad, J.; Uhlen, M., Magnetic separation techniques in diagnostic microbiology. *Clinical Microbiology Reviews* **1994,** 7, (1), 43-54.

245. Uehara, M.; Mori, S.; Chen, C. H.; Cheong, S. W., Percolative phase separation underlies colossal magnetoresistance in mixed-valent manganites. *Nature* **1999,** 399, (6736), 560-563.

246. Dagotto, E.; Hotta, T.; Moreo, A., Colossal magnetoresistant materials: The key role of phase separation. *Physics Reports-Review Section of Physics Letters* **2001,** 344, (1-3), 1-153.

247. Weissleder, R.; Elizondo, G.; Wittenberg, J.; Rabito, C. A.; Bengele, H. H.; Josephson, L., Ultrasmall superparamagnetic iron-oxide - Characterization of a new class of contrast agents for MR Imaging. *Radiology* **1990,** 175, (2), 489-493.

248. Wang, Y. X. J.; Hussain, S. M.; Krestin, G. P., Superparamagnetic iron oxide contrast agents: physicochemical characteristics and applications in MR imaging. *European Radiology* **2001,** 11, (11), 2319-2331.

249. Mornet, S.; Vasseur, S.; Grasset, F.; Duguet, E., Magnetic nanoparticle design for medical diagnosis and therapy. *Journal of Materials Chemistry* **2004,** 14, (14), 2161-2175.

250. Ross, C., Patterned magnetic recording media. *Annual Review of Materials Research* **2001,** 31, 203-235.

251. Moser, A.; Takano, K.; Margulies, D. T.; Albrecht, M.; Sonobe, Y.; Ikeda, Y.; Sun, S. H.; Fullerton, E. E., Magnetic recording: advancing into the future. *Journal of Physics D-Applied Physics* **2002,** 35, (19), R157-R167.

252. Terris, B. D.; Thomson, T., Nanofabricated and self-assembled magnetic structures as data storage media. *Journal of Physics D-Applied Physics* **2005,** 38, (12), R199-R222.

253. Tartaj, P.; Morales, M. D.; Veintemillas-Verdaguer, S.; Gonzalez-Carreno, T.; Serna, C. J., The preparation of magnetic nanoparticles for applications in biomedicine. *Journal of Physics D-Applied Physics* **2003,** 36, (13), R182-R197.

254. Pankhurst, Q. A.; Connolly, J.; Jones, S. K.; Dobson, J., Applications of magnetic nanoparticles in biomedicine. *Journal of Physics D-Applied Physics* **2003,** 36, (13), R167-R181.

255. Gupta, A. K.; Gupta, M., Synthesis and surface engineering of iron oxide nanoparticles for biomedical applications. *Biomaterials* **2005,** 26, (18), 3995-4021.

256. Jun, Y. W.; Seo, J. W.; Cheon, A., Nanoscaling laws of magnetic nanoparticles and their applicabilities in biomedical sciences. *Accounts of Chemical Research* **2008,** 41, (2), 179-189.

257. Iglesias, O.; Batlle, X.; Labarta, A., Particle size and cooling field dependence of exchange bias in core/shell magnetic nanoparticles. *Journal of Physics D-Applied Physics* **2008,** 41, (13), 134010.

258. Gibbs, M. R. J., Nanomagnetism - nascent or fully formed? *Current Opinion in Solid State & Materials Science* **2003,** 7, (2), 83-86.

259. Kodama, R. H., Magnetic nanoparticles. *Journal of Magnetism and Magnetic Materials* **1999,** 200, (1-3), 359-372.

260. Respaud, M.; Broto, J. M.; Rakoto, H.; Fert, A. R.; Thomas, L.; Barbara, B.; Verelst, M.; Snoeck, E.; Lecante, P.; Mosset, A.; Osuna, J.; Ely, T. O.; Amiens, C.; Chaudret, B., Surface effects on the magnetic properties of ultrafine cobalt particles. *Physical Review B* **1998,** 57, (5), 2925-2935.

261. Bodker, F.; Morup, S.; Linderoth, S., Surface effects in metallic iron nanoparticles. *Physical Review Letters* **1994,** 72, (2), 282-285.

262. Rugar, D.; Yannoni, C. S.; Sidles, J. A., Mechanical detection of magnetic-resonance. *Nature* **1992,** 360, (6404), 563-566.

263. Sidles, J. A.; Garbini, J. L.; Bruland, K. J.; Rugar, D.; Zuger, O.; Hoen, S.; Yannoni, C. S., Magnetic-resonance force microscopy. *Reviews of Modern Physics* **1995,** 67, (1), 249-265.

264. Zhang, Z.; Hammel, P. C.; Wigen, P. E., Observation of ferromagnetic resonance in a microscopic sample using magnetic resonance force microscopy. *Applied Physics Letters* **1996,** 68, (14), 2005-2007.

265. Rugar, D.; Budakian, R.; Mamin, H. J.; Chui, B. W., Single spin detection by magnetic resonance force microscopy. *Nature* **2004,** 430, (6997), 329-332.

266. Han, W. H.; Lindsay, S. M.; Jing, T. W., A magnetically driven oscillating probe microscope for operation in liquids. *Applied Physics Letters* **1996,** 69, (26), 4111-4113.

267. Leuba, S. H.; Lindsay, S. M., Magnetically driven oscillating probe ("MAC mode") scanning force microscopy (SFM) of chromatin fibers in aqueous buffer. *Biophysical Journal* **1998,** 74, (2), A71-A71.

268. Kienberger, F.; Stroh, C.; Kada, G.; Moser, R.; Baumgartner, W.; Pastushenko, V.; Rankl, C.; Schmidt, U.; Muller, H.; Orlova, E.; LeGrimellec, C.; Drenckhahn, D.; Blaas, D.; Hinterdorfer, P., Dynamic force microscopy imaging of native membranes. *Ultramicroscopy* **2003,** 97, (1-4), 229-237.

269. Ge, G. L.; Han, D.; Lin, D. Y.; Chu, W. G.; Sun, Y. X.; Jiang, L.; Ma, W. Y.; Wang, C., MAC mode atomic force microscopy studies of living samples, ranging from cells to fresh tissue. *Ultramicroscopy* **2007,** 107, (4-5), 299-307.

270. Florin, E. L.; Radmacher, M.; Fleck, B.; Gaub, H. E., Atomic-force microscope with magnetic force modulation. *Review of Scientific Instruments* **1994,** 65, (3), 639-643.

271. Yamamoto, S.; Yamada, H., Interpretation of direct and indirect force modulation methods using polymer films. *Langmuir* **1997,** 13, (18), 4861-4864.

272. Schemmel, A.; Gaub, H. E., Single molecule force spectrometer with magnetic force control and inductive detection. *Review of Scientific Instruments* **1999,** 70, (2), 1313-1317.

273. Scherer, M. P.; Gummer, A. W., Impedance analysis of the organ of corti with magnetically actuated probes. *Biophysical Journal* **2004,** 87, (2), 1378-1391.

274. Martin, Y.; Wickramasinghe, H. K., Magnetic imaging by force microscopy with 1000-a resolution. *Applied Physics Letters* **1987,** 50, (20), 1455-1457.

275. Hehn, M.; Padovani, S.; Ounadjela, K.; Bucher, J. P., Nanoscale magnetic domain structures in epitaxial cobalt films. *Physical Review B* **1996,** 54, (5), 3428-3433.

276. Porthun, S.; Abelmann, L.; Lodder, C., Magnetic force microscopy of thin film media for high density magnetic recording. *Journal of Magnetism and Magnetic Materials* **1998,** 182, (1-2), 238-273.

277. Belliard, L.; Miltat, J.; Thiaville, A.; Dubois, S.; Duvail, J. L.; Piraux, L., Observing magnetic nanowires by means of magnetic force microscopy. *Journal of Magnetism and Magnetic Materials* **1998,** 190, (1-2), 1-16.

278. Qin, D. H.; Lu, M.; Li, H. L., Magnetic force microscopy of magnetic domain structure in highly ordered Co nanowire arrays. *Chemical Physics Letters* **2001,** 350, (1-2), 51-56.

279. Puntes, V. F.; Gorostiza, P.; Aruguete, D. M.; Bastus, N. G.; Alivisatos, A. P., Collective behaviour in two-dimensional cobalt nanoparticle assemblies observed by magnetic force microscopy. *Nature Materials* **2004,** 3, (4), 263-268.

280. Hartmann, U., Magnetic force microscopy. *Annual Review of Materials Science* **1999,** 29, 53-87.

281. Freeman, M. R.; Choi, B. C., Advances in magnetic microscopy. *Science* **2001,** 294, (5546), 1484-1488.

282. Abe, M.; Tamaura, Y.; Goto, Y.; Kitamura, N.; Gomi, M., High-speed deposition of high-quality ferrite films from aqueous-solution at low-temperatures (less-than-or-equal-to-90-degrees-C). *Journal of Applied Physics* **1987,** 61, (8), 3211-3213.

283. Palacin, S.; Hidber, P. C.; Bourgoin, J. P.; Miramond, C.; Fermon, C.; Whitesides, G. M., Patterning with magnetic materials at the micron scale. *Chemistry of Materials* **1996,** 8, (6), 1316-1325.

284. Binnig, G.; Quate, C. F.; Gerber, C., Atomic force microscope. *Physical Review Letters* **1986,** 56, (9), 930-933.

285. Binnig, G.; Smith, D. P. E., Single-tube 3-dimensional scanner for scanning tunneling microscopy. *Review of Scientific Instruments* **1986,** 57, (8), 1688-1689.

286. Schitter, G.; Menold, P.; Knapp, H. F.; Allgower, F.; Stemmer, A., High performance feedback for fast scanning atomic force microscopes. *Review of Scientific Instruments* **2001,** 72, (8), 3320-3327.

287. Ando, T.; Kodera, N.; Takai, E.; Maruyama, D.; Saito, K.; Toda, A., A high-speed atomic force microscope for studying biological macromolecules. *Proceedings of the National Academy of Sciences of the United States of America* **2001,** 98, (22), 12468-12472.

288. Schitter, G.; Allgower, F.; Stemmer, A., A new control strategy for high-speed atomic force miciroscopy. *Nanotechnology* **2004,** 15, (1), 108-114.

289. Schitter, G.; Stark, R. W.; Stemmer, A., Fast contact-mode atomic force microscopy on biological specimen by model-based control. *Ultramicroscopy* **2004,** 100, (3-4), 253-257.

290. Lindsay, S. M.; Lyubchenko, Y. L.; Tao, N. J.; Li, Y. Q.; Oden, P. I.; Derose, J. A.; Pan, J., Scanning-tunneling-microscopy and atomic-force microscopy studies of biomaterials at a liquid-solid interface. *Journal of Vacuum Science & Technology a-Vacuum Surfaces and Films* **1993,** 11, (4), 808-815.

291. DeVecchio, D.; Bhushan, B., Localized surface elasticity measurements using an atomic force microscope. *Review of Scientific Instruments* **1997,** 68, (12), 4498-4505.

292. Price, W. J.; Kuo, P. K.; Lee, T. R.; Colorado, R.; Ying, Z. C.; Liu, G. Y., Probing the local structure and mechanical response of nanostructures using force modulation and nanofabrication. *Langmuir* **2005,** 21, (18), 8422-8428.

293. Price, W. J.; Leigh, S. A.; Hsu, S. M.; Patten, T. E.; Liu, G. Y., Measuring the size dependence of Young's modulus using force modulation atomic force microscopy. *Journal of Physical Chemistry A* **2006,** 110, (4), 1382-1388.

294. Jun, Y. W.; Huh, Y. M.; Choi, J. S.; Lee, J. H.; Song, H. T.; Kim, S.; Yoon, S.; Kim, K. S.; Shin, J. S.; Suh, J. S.; Cheon, J., Nanoscale size effect of magnetic nanocrystals and their utilization for cancer diagnosis via magnetic resonance imaging. *Journal of the American Chemical Society* **2005,** 127, (16), 5732-5733.

295. Lu, Y.; Yin, Y. D.; Mayers, B. T.; Xia, Y. N., Modifying the surface properties of superparamagnetic iron oxide nanoparticles through a sol-gel approach. *Nano Letters* **2002,** 2, (3), 183-186.

296. Sun, S. H.; Zeng, H.; Robinson, D. B.; Raoux, S.; Rice, P. M.; Wang, S. X.; Li, G. X., Monodisperse MFe2O4 (M = Fe, Co, Mn) nanoparticles. *Journal of the American Chemical Society* **2004,** 126, (1), 273-279.

297. Jeong, U.; Teng, X. W.; Wang, Y.; Yang, H.; Xia, Y. N., Superparamagnetic colloids: Controlled synthesis and niche applications. *Advanced Materials* **2007,** 19, (1), 33-60.

298. Hu, J.; Xiao, X. D.; Salmeron, M., Scanning polarization force microscopy - a technique for imaging liquids and weakly adsorbed layers. *Applied Physics Letters* **1995,** 67, (4), 476-478.

299. Luna, M.; Rieutord, F.; Melman, N. A.; Dai, Q.; Salmeron, M., Adsorption of water on alkali halide surfaces studied by scanning polarization force microscopy. *Journal of Physical Chemistry A* **1998,** 102, (34), 6793-6800.

300. Hu, J.; Carpick, R. W.; Salmeron, M.; Xiao, X. D., Imaging and manipulation of nanometer-size liquid droplets by scanning polarization force microscopy. *Journal of Vacuum Science & Technology B* **1996,** 14, (2), 1341-1343.

301. Chou, S. Y.; Krauss, P. R.; Kong, L. S., Nanolithographically defined magnetic structures and quantum magnetic disk. *Journal of Applied Physics* **1996,** 79, (8), 6101-6106.

302. Rugar, D.; Mamin, H. J.; Guethner, P.; Lambert, S. E.; Stern, J. E.; McFadyen, I.; Yogi, T., Magnetic force microscopy - General-principles and application to longitudinal recording media. *Journal of Applied Physics* **1990,** 68, (3), 1169-1183.

303. Hehn, M.; Ounadjela, K.; Bucher, J. P.; Rousseaux, F.; Decanini, D.; Bartenlian, B.; Chappert, C., Nanoscale magnetic domains in mesoscopic magnets. *Science* **1996,** 272, (5269), 1782-1785.

304. Noy, A.; Frisbie, C. D.; Rozsnyai, L. F.; Wrighton, M. S.; Lieber, C. M., Chemical force microscopy - Exploiting chemically-modified tips to quantify adhesion, friction, and functional-group distributions in molecular assemblies. *Journal of the American Chemical Society* **1995,** 117, (30), 7943-7951.

305. Wold, D. J.; Frisbie, C. D., Fabrication and characterization of metal-molecule-metal junctions by conducting probe atomic force microscopy. *Journal of the American Chemical Society* **2001,** 123, (23), 5549-5556.

306. Wold, D. J.; Haag, R.; Rampi, M. A.; Frisbie, C. D., Distance dependence of electron tunneling through self-assembled monolayers measured by conducting probe atomic force microscopy: Unsaturated versus saturated molecular junctions. *Journal of Physical Chemistry B* **2002,** 106, (11), 2813-2816.

307. Rawlett, A. M.; Hopson, T. J.; Nagahara, L. A.; Tsui, R. K.; Ramachandran, G. K.; Lindsay, S. M., Electrical measurements of a dithiolated electronic molecule via conducting atomic force microscopy. *Applied Physics Letters* **2002,** 81, (16), 3043-3045.

308. McLean, R. S.; Sauer, B. B., Tapping-mode AFM studies using phase detection for resolution of nanophases in segmented polyurethanes and other block copolymers. *Macromolecules* **1997,** 30, (26), 8314-8317.

309. Putman, C. A. J.; Vanderwerf, K. O.; Degrooth, B. G.; Vanhulst, N. F.; Greve, J., Viscoelasticity of living cells allows high-resolution imaging by tapping mode atomic-force microscopy. *Biophysical Journal* **1994,** 67, (4), 1749-1753.

310. Winkler, R. G.; Spatz, J. P.; Sheiko, S.; Moller, M.; Reineker, P.; Marti, O., Imaging material properties by resonant tapping-force microscopy: A model investigation. *Physical Review B* **1996,** 54, (12), 8908-8912.

311. Maivald, P.; Butt, H. J.; Gould, S. A. C.; Prater, C. B.; Drake, B.; Gurley, J. A.; Elings, V. B.; Hansma, P. K., Using force modulation to image surface elasticities with the atomic force microscope. *Nanotechnology* **1991,** 2, 103-106.

312. Greene, M. E.; Kinser, C. R.; Kramer, D. E.; Pingree, L. S. C.; Hersam, M. C., Application of scanning probe microscopy to the characterization and fabrication of hybrid nanomaterials. *Microscopy Research and Technique* **2004,** 64, (5-6), 415-434.

313. Magonov, S. N.; Elings, V.; Whangbo, M. H., Phase imaging and stiffness in tapping-mode atomic force microscopy. *Surface Science* **1997,** 375, (2-3), L385-L391.

314. Overney, R. M.; Meyer, E.; Frommer, J.; Guntherodt, H. J.; Fujihira, M.; Takano, H.; Gotoh, Y., Force microscopy study of friction and elastic compliance of phase-separated organic thin-films. *Langmuir* **1994,** 10, (4), 1281-1286.

315. Yamanaka, K.; Ogiso, H.; Kolosov, O., Ultrasonic force microscopy for nanometer resolution subsurface imaging. *Applied Physics Letters* **1994,** 64, (2), 178-180.

316. Nie, H. Y.; Motomatsu, M.; Mizutani, W.; Tokumoto, H., Local modification of elastic properties of polystyrene-polyethyleneoxide blend surfaces. *Journal of Vacuum Science & Technology B* **1995,** 13, (3), 1163-1166.

317. Nysten, B.; Legras, R.; Costa, J. L., Atomic-force microscopy imaging of viscoelastic properties in toughened polypropylene resins. *Journal of Applied Physics* **1995,** 78, (10), 5953-5958.

318. Snitka, V.; Ulcinas, A.; Mizariene, V., Characterization of materials' nanomechanical properties by force modulation and phase imaging atomic force microscopy with soft cantilevers. *Materials Characterization* **2002,** 48, (2-3), 147-152.

319. Haga, H.; Sasaki, S.; Morimoto, M.; Kawabata, K.; Ito, E.; Abe, K.; Sambongi, T., Imaging elastic properties of soft materials immersed in water using force modulation mode in atomic force microscopy. *Japanese Journal of Applied Physics Part 1-Regular Papers Short Notes & Review Papers* **1998,** 37, (6B), 3860-3863.

320. Crittenden, S.; Raman, A.; Reifenberger, R., Probing attractive forces at the nanoscale using higher-harmonic dynamic force microscopy. *Physical Review B* **2005,** 72, (23), 235422.

321. Xu, X.; Raman, A., Comparative dynamics of magnetically, acoustically, and Brownian motion driven microcantilevers in liquids. *Journal of Applied Physics* **2007,** 102, (3), 034303.

322. Kiridena, W.; Jain, V.; Kuo, P. K.; Liu, G. Y., Nanometer-scale elasticity measurements on organic monolayers using scanning force microscopy. *Surface and Interface Analysis* **1997,** 25, (6), 383-389.

323. Zhong, Q.; Inniss, D.; Kjoller, K.; Elings, V. B., Fractured polymer silica fiber surface studied by tapping mode atomic-force microscopy. *Surface Science* **1993,** 290, (1-2), L688-L692.

324. Pietrement, O.; Troyon, M., Quantitative elastic modulus measurement by magnetic force modulation microscopy. *Tribology Letters* **2000,** 9, (1-2), 77-87.

325. Kawakami, M.; Byrne, K.; Khatri, B. S.; McLeish, T. C. B.; Radford, S. E.; Smith, D. A., Viscoelastic measurements of single molecules on a millisecond time scale by

magnetically driven oscillation of an atomic force microscope cantilever. *Langmuir* **2005,** 21, (10), 4765-4772.

326. Asif, S. A. S.; Wahl, K. J.; Colton, R. J.; Warren, O. L., Quantitative imaging of nanoscale mechanical properties using hybrid nanoindentation and force modulation. *Journal of Applied Physics* **2001,** 90, (3), 1192-1200.

327. Tamayo, J.; Garcia, R., Deformation, contact time, and phase contrast in tapping mode scanning force microscopy. *Langmuir* **1996,** 12, (18), 4430-4435.

328. Tamayo, J.; Garcia, R., Effects of elastic and inelastic interactions on phase contrast images in tapping-mode scanning force microscopy. *Applied Physics Letters* **1997,** 71, (16), 2394-2396.

329. Bar, G.; Brandsch, R.; Whangbo, M. H., Description of the frequency dependence of the amplitude and phase angle of a silicon cantilever tapping on a silicon substrate by the harmonic approximation. *Surface Science* **1998,** 411, (1-2), L802-L809.

330. Whangbo, M. H.; Bar, G.; Brandsch, R., Description of phase imaging in tapping mode atomic force microscopy by harmonic approximation. *Surface Science* **1998,** 411, (1-2), L794-L801.

331. Putman, C. A. J.; Vanderwerf, K. O.; Degrooth, B. G.; Vanhulst, N. F.; Greve, J., Tapping mode atomic-force microscopy in liquid. *Applied Physics Letters* **1994,** 64, (18), 2454-2456.

332. Noy, A.; Sanders, C. H.; Vezenov, D. V.; Wong, S. S.; Lieber, C. M., Chemically-sensitive imaging in tapping mode by chemical force microscopy: Relationship between phase lag and adhesion. *Langmuir* **1998,** 14, (7), 1508-1511.

333. Czajkowsky, D. M.; Allen, M. J.; Elings, V.; Shao, Z. F., Direct visualization of surface charge in aqueous solution. *Ultramicroscopy* **1998,** 74, (1-2), 1-5.

334. Wadu-Mesthrige, K.; Amro, N. A.; Garno, J. C.; Cruchon-Dupeyrat, S.; Liu, G. Y., Contact resonance imaging - a simple approach to improve the resolution of AFM for biological and polymeric materials. *Applied Surface Science* **2001,** 175, 391-398.

APPENDIX A: LABORATORY PROCEDURE FOR PARTICLE LITHOGRAPHY COMBINED WITH VAPOR DEPOSITION OF ORGANOSILANES

1. Use ruby muscovite mica(0001) or double-sided polished silicon(111) wafers as substrates used for particle lithography with organosilanes. Cut pieces of mica needs to 1×1 cm^2) and immediately cleave the mica to produce clean, atomically flat surfaces before used. Cut the silicon wafers into 1×1 cm^2 pieces. Immerse the pieces in piranha solution for 1 h, for cleaning. Piranha solution is a mixture of sulfuric acid (96%) and hydrogen peroxide (30%,) at 3:1 ratio (v/v). After piranha cleaning, rinse the silicon substrates with deionized water.

2. Wash the monodisperse polystyrene latex solutions with deionized water using centrifugation twice to remove contaminants such as charge stabilizers or surfactants. After centrifuging latex solutions for 10 min at 14000 rpm, a pellet is formed at the bottom of the microcentrifuge tube. The pellets can then be resuspended in desired volume of deionized water by vortex mixing.

3. Deposit 20 μL of an aqueous solution containing washed monodisperse latex onto the substrate. Dry the samples in ambient conditions (25 °C, relative humidity ~60%), for at least 2 h to produce for ring-shaped nanopatterns. For pore-shaped morphologies, dry the samples need for 25 min.

4. Place the samples with dried latex films into a plastic vessel containing 300 μL of neat organosilanes. To generate a vapor, seal the reaction vessel with parafilm and place in an oven at 70 C for 8 h.

5. When using mica(0001) as the substrate, the mask of latex particles can be removed by rinsing with deionized water and ethanol. Sonication will damage the samples. If the substrate is Si(111), the mask of latex particles can be removed by sonication in ethanol for 15 min followed by further rinsing with ethanol and deionized water.

APPENDIX B: PROCEDURE FOR MAGNETIC SAMPLE MODULATION

The instrument set-up for MSM is a hybrid of contact mode AFM combined with selective actuation of magnetic samples. For MSM operation, connect cables as shown in Figure B.1. A cable connects the **AUX** of head electronic box to the **PHASE input** of MAC/AC controller. Connect a second cable from **AMPLITUDE output** of MAC/AC controller to the **AUX IN** of the PicoSPM II controller. The magnetic AC (MAC) sample plate is used to drive the oscillation magnetic materials. Use the plain nosecone with the Agilent 5500 AFM multipurpose scanner with a scanning area of 11 x 11 μm^2 for MSM imaging.
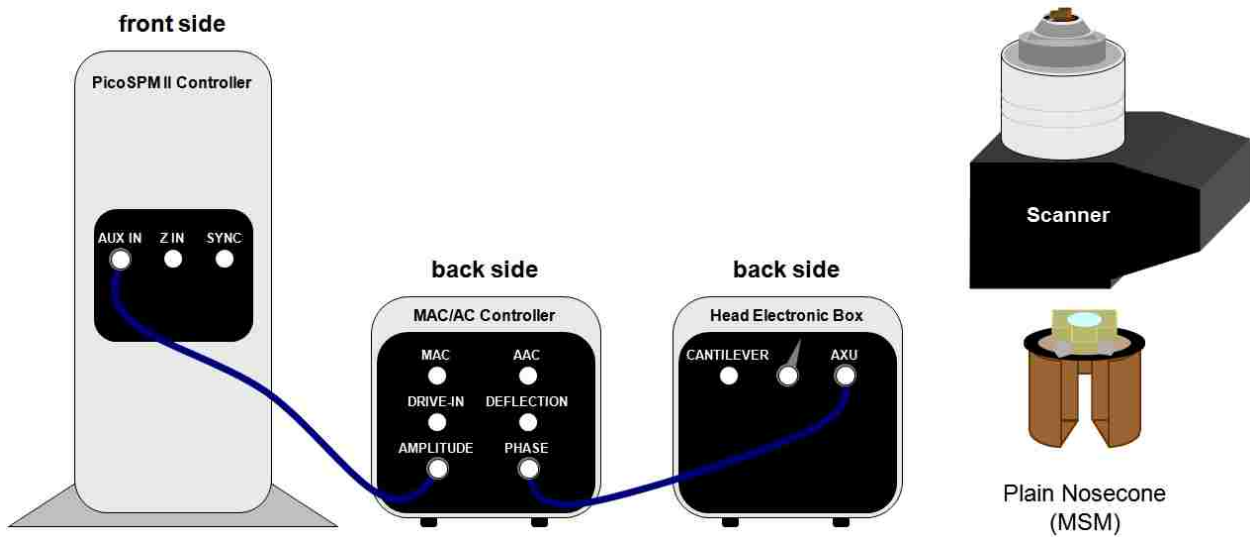

Figure B.1 Cable configuration for magnetic sample modulation AFM.

1. Connect two cables between PicoSPM II controller, MAC/AC controller and head electronic box as shown in Figure B.1.

2. Install the plain nosecone into the Agilent 5500 AFM multipurpose scanner. Use the MAC mode sample plate for mounting the sample.

3. Use silicon nitride cantilevers (MSCT-AUHW, Veeco Probes) with force constants of 0.1 N m^{-1} and resonance frequency of 26 kHz for contact mode and MSM imaging.

4. Install the MAC mode sample stage and the scanner for contact mode operation. Adjust the position of laser and photodiode signal.

5. Launch the PicoScan v5.3.3 software. Under **main menu**, select contact mode parameters for the Agilent 5500 AFM multipurpose scanner.

6. Use the **Layout Editor** to create eight channels including include topography, defection, Axu IN and Axu IN 5 on the top/bottom row. Choose channels on the top row to represent raw data and those on the bottom row to display processed data.

7. Open the AFM AC Mode Frequency Plot window and set up the frequency range.

8. Run a frequency sweep without MSM while the tip is disengaged to confirm that there is no magnetic response by silicon nitride probe or nosecone. Also, get information of background level.

9. Select MAC/Top MAC option in AC Mode controls window. Disable the **Drive On**.

10. Enter 0 for the **Force Setpoint** and then start to approach.

11. After the tip engages the surface, click on the **Sweep** button to acquire a frequency spectrum without the AC electromagnetic field.

12. Select the **Drive On** and enter 5 for the **Drive On %** and 1X for **Gain**. Click on the **Sweep** button to acquire a frequency spectrum with the AC electromagnetic field.

13. Adjust the **Drive On %** and **frequency range** until significant, detectable peaks are observed for the frequency sweep.

14. Choose the resonance frequency for the magnetic driving signal by left clicking the resonance peak maximum.

15. Check the **Active check box** in the AFM AC Mode Frequency Plot window.

16. Start to acquire MSM images and adjust the **Integral (I) Gain**, the **Proportional (P) Gain** and the **Force Setpoint** like regular contact mode AFM.

17. During experiments, compare images and spectra with and without the field activated. Turn the field on and off by clicking the **Drive On**.

18. To acquire MSM spectra, the AFM tip must be place in direct contact with a vibrating nanoparticle or nanostructure. Use contact mode images with successive, small zoom-in views to ensure that the tip is placed on a magnetic area.

19. The spectra acquired with MSM will change according to the site of the magnetic domain. During MSM experiments, evaluate spectra and measurements within 10-20 kHz of the primary resonance frequency to optimize parameters.

20. Evaluate MSM parameters of **Drive On %** to determine the change in sample response with field strength.

APPENDIX C: PROCEDURE FOR INDIRECT MAGNETIC MODULATION

The instrument configuration for AFM imaging using IMM is displayed in Figure C.1. Before IMM operation, connect cables for the PicoSPM II controller, MAC/AC controller and head electronic box as shown in the cable diagram. A cable connects **AUX** of head electronic box to the **PHAS**E input of MAC/AC Controller. Another cable connects the **AMPLITUDE** of MAC/AC controller to the **AUX IN** of PicoSPM II controller. The magnetic AC (MAC) sample plate is used to drive the oscillation of nosecone for IMM imaging. An Agilent 5500 AFM multipurpose scanner with a scan area of 11 x 11 μm^2 is used for contact mode AFM imaging with an AAC nosecone.
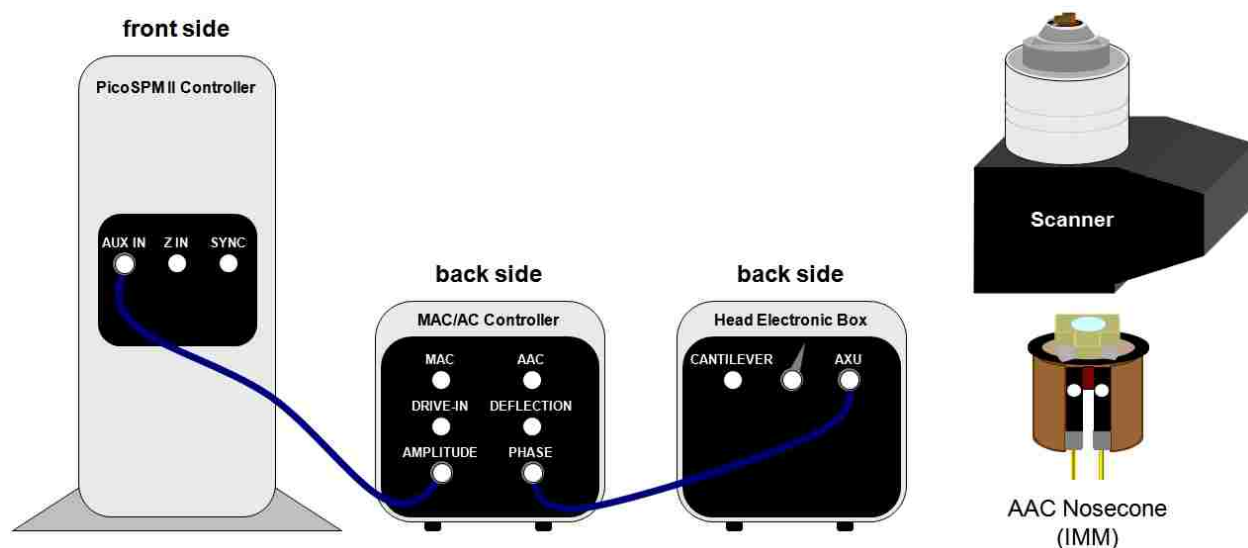

Figure C.1 Cable configuration for indirect magnetic modulation.

1. Connect the cables between PicoSPM II controller, MAC/AC controller and head electronic box as shown in Figure C.1.

2. Install the AAC or Top-MAC nosecone into the Agilent 5500 AFM multipurpose scanner.

3. Place a sample onto MAC mode sample plate.

4. Silicon nitride cantilevers (MSCT-AUHW, Veeco Probes) with force constants of 0.1 N m^{-1} and resonance frequency of 26 kHz should be for contact mode imaging using IMM. Silicon cantilevers (SICON, NanoScience Instruments) with force constants of 0.2 N m^{-1} and a resonance frequency of 12 kHz can also be used for IMM imaging.

5. Install the MAC mode sample stage and the scanner. Adjust the laser position to optimize the photodiode signal.

6. Launch PicoScan v5.3.3 software. From the **main menu**, select contact mode and parameters for the Agilent 5500 AFM multipurpose scanner.

7. Use the **Layout Editor** to create eight channels including include topography, defection, Axu IN and Axu IN 5 on the top and bottom row. Use the channels on the top row to represent raw data and those on the bottom row for processed data.

8. Open the AFM AC Mode Frequency Plot window and set up the frequency range.

9. Select MAC/Top MAC option in AC Mode controls window. Disable the **Drive On**.

10. Enter 0 for the **Force Setpoint** and then start to approach.

11. After the tip engages the surface, click on the **Sweep** button to acquire a frequency spectrum without activating the AC electromagnetic field.

12. Select the **Drive On** and enter 5 for the **Drive On %** and 1X for **Gain**. Reduce the **Force Setpoint** to the minimum to lift up the tip.

13. Click on the **Sweep** button to acquire a resonance spectrum with the AC electromagnetic field when the tip is disengaged with the surface.

14. Adjust the **Drive On %** and **frequency range** (0-600 kHz) until significant frequencies are observed.

15. Increase the **Force Setpoint** to bring the tip in contact with the surface. Click on the **Sweep** button to acquire a resonance spectrum with the AC electromagnetic field when the tip is engaged with the surface.

16. Adjust the **Drive On %** and **frequency range** until significant frequencies are observed.

17. Compare resonance frequency spectra acquired with or without the tip in contact with surfaces. When the tip engages the surface, the natural resonance frequency slightly shifts.

18. Select the resonance frequency for IMM by left clicking the resonance peak maximum.

19. Check the **Active check box** in the AFM AC Mode Frequency Plot window.

20. Start to acquire IMM images and adjust the **Integral (I) Gain**, the **Proportional (P) Gain** and the **Force Setpoint** like regular contact mode AFM.

21. To optimize the driving frequency for IMM imaging, scanning pre-resonance, on-resonance and post-resonance should be a protocol for every experiment.

APPENDIX D: LETTERS OF PERMISSION

Jie-Ren Li <jli11@tigers.lsu.edu>

RE: Permission Request Form: Jie-Ren Li

1 message

CONTRACTS-COPYRIGHT (shared) <Contracts-Copyright@rsc.org>   Tue, Mar 24, 2009 at 3:13 AM
To: "jli11@lsu.edu" <jli11@lsu.edu>

Dear Dr Li

The Royal Society of Chemistry (RSC) hereby grants permission for the use of your paper(s) specified below in the printed and microfilm version of your thesis. You may also make available the PDF version of your paper(s) that the RSC sent to the corresponding author(s) of your paper(s) upon publication of the paper(s) in the following ways: in your thesis via any website that your university may have for the deposition of theses, via your university's Intranet or via your own personal website. We are however unable to grant you permission to include the PDF version of the paper(s) on its own in your institutional repository. The Royal Society of Chemistry is a signatory to the STM Guidelines on Permissions (available on request).

Please note that if the material specified below or any part of it appears with credit or acknowledgement to a third party then you must also secure permission from that third party before reproducing that material.

Please ensure that the thesis states the following:

Reproduced by permission of The Royal Society of Chemistry

and include a link to the article on the Royal Society of Chemistry's website.

Please ensure that your co-authors are aware that you are including the paper in your thesis.

Regards

Gill Cockhead

Contracts & Copyright Executive

Gill Cockhead (Mrs), Contracts & Copyright Executive
Royal Society of Chemistry, Thomas Graham House
Science Park, Milton Road, Cambridge CB4 0WF, UK
Tel +44 (0) 1223 432134, Fax +44 (0) 1223 423623
http://www.rsc.org

Any Additional Comments:

I am requesting permission to include this article in my dissertation.

DISCLAIMER:

This communication (including any attachments) is intended for the use of the addressee only and may contain confidential, privileged or copyright material. It may not be relied upon or disclosed to any other person without the consent of the RSC. If you have received it in error, please contact us immediately. Any advice given by the RSC has been carefully formulated but is necessarily based on the information available, and the RSC cannot be held responsible for accuracy or completeness. In this respect, the RSC owes no duty of care and shall not be liable for any resulting damage or loss. The RSC acknowledges that a disclaimer cannot restrict liability at law for personal injury or death arising through a finding of negligence. The RSC does not warrant that its emails or attachments are Virus-free: Please rely on your own screening.

American Chemical Society's Policy on Theses and Dissertations

If your university requires a signed copy of this letter see contact information below.

Thank you for your request for permission to include **your** paper(s) or portions of text from **your** paper(s) in your thesis. Permission is now automatically granted; please pay special attention to the implications paragraph below. The Copyright Subcommittee of the Joint Board/Council Committees on Publications approved the following:

Copyright permission for published and submitted material from theses and dissertations
ACS extends blanket permission to students to include in their theses and dissertations their own articles, or portions thereof, that have been published in ACS journals or submitted to ACS journals for publication, provided that the ACS copyright credit line is noted on the appropriate page(s).

Publishing implications of electronic publication of theses and dissertation material
Students and their mentors should be aware that posting of theses and dissertation material on the Web prior to submission of material from that thesis or dissertation to an ACS journal may affect publication in that journal. Whether Web posting is considered prior publication may be evaluated on a case-by-case basis by the journal's editor. If an ACS journal editor considers Web posting to be "prior publication", the paper will not be accepted for publication in that journal. If you intend to submit your unpublished paper to ACS for publication, check with the appropriate editor prior to posting your manuscript electronically.

If your paper has **not** yet been published by ACS, we have no objection to your including the text or portions of the text in your thesis/dissertation in **print and microfilm formats**; please note, however, that electronic distribution or Web posting of the unpublished paper as part of your thesis in electronic formats might jeopardize publication of your paper by ACS. Please print the following credit line on the first page of your article: "Reproduced (or 'Reproduced in part') with permission from [JOURNAL NAME], in press (or 'submitted for publication'). Unpublished work copyright [CURRENT YEAR] American Chemical Society." Include appropriate information.

If your paper has already been published by ACS and you want to include the text or portions of the text in your thesis/dissertation in **print or microfilm formats**, please print the ACS copyright credit line on the first page of your article: "Reproduced (or 'Reproduced in part') with permission from [FULL REFERENCE CITATION.] Copyright [YEAR] American Chemical Society." Include appropriate information.

Submission to a Dissertation Distributor: If you plan to submit your thesis to UMI or to another dissertation distributor, you should not include the unpublished ACS paper in your thesis if the thesis will be disseminated electronically, until ACS has published your paper. After publication of the paper by ACS, you may release the entire thesis (**not the individual ACS article by itself**) for electronic dissemination through the distributor; ACS's copyright credit line should be printed on the first page of the ACS paper.

Use on an Intranet: The inclusion of your ACS unpublished or published manuscript is permitted in your thesis in print and microfilm formats. If ACS has published your paper you may include the manuscript in your thesis on an intranet that is not publicly available. Your ACS article cannot be posted electronically on a publicly available medium (i.e. one that is not password protected), such as but not limited to, electronic archives, Internet, library server, etc. The only material from your paper that can be posted on a public electronic medium is the article abstract, figures, and tables, and you may link to the article's DOI or post the article's author-directed URL link provided by ACS. This paragraph does not pertain to the dissertation distributor paragraph above.

Questions? Call +1 202/872-4368/4367. Send e-mail to copyright@acs.org or fax to +1 202-776-8112.   10/10/03, 01/15/04, 06/07/06

VITA

Jie-Ren Li was born and grew up in Taipei, Taiwan. He earned his Bachelor of Science degree in Chemistry from National Chung Cheng University 1998. Upon graduation, he went on to pursue master's degree at National Chiao Tung University in 2000. He started his academic journey in the United States in Fall 2004. He enrolled at Louisiana State University, where he pursued a doctoral degree in the field of analytical chemistry under the supervision of Dr. Jayne C. Garno. His research interests included applications of scanning probe microscopy for surface characterization and lithography, fabrication of functional nanostructures with particle lithography, and synthesis of nanoparticles.

During studies at LSU, he submitted eight first author journal articles. A collaborative manuscript for *Langmuir* resulted from research with Dr. Evgueni E. Nesterov of the LSU Chemistry Department. Another collaborative manuscript with Agilent Technologies was submitted to *Analytical Chemistry*. He participated in regional, national and international conferences, where he presented his research results. Jie-Ren also received several awards, including LSU Graduate School Supplement Award, Graduate Student Travel Award, Charles E. Coates Travel Award, Best Student Poster Award of ACS National Meeting and Pfizer Graduate Research Fellowship in Analytical Chemistry Award.